Measurement of Multijet Events at low x_{Bj} and low Q^2 with the ZEUS Detector at HERA

Dissertation
zur Erlangung des Doktorgrades
des Departments Physik
der Universität Hamburg

vorgelegt von
Tim Gosau
aus Hamburg

Hamburg
Juli 2007

Gutachter der Dissertation: Prof. Dr. R. Klanner
Prof. Dr. E. Elsen

Gutachter der Disputation: Prof. Dr. K. Wick
Prof. Dr. P. Schleper

Datum der Disputation: 02.08.2007

Vorsitzender des Prüfungsausschusses: Prof. Dr. E. Heumann

Vorsitzender des Promotionsausschusses: Prof. Dr. G. Huber

Dekan der MIN-Fakultät: Prof. Dr. A. Frühwald

Abstract

In this thesis, cross sections of inclusive and differential di- and trijet production in deep inelastic electron-proton scattering at low Bjorken-x have been determined and compared to perturbative QCD calculations at next-to-leading order. The data were taken during the years $1998 - 2000$ with the ZEUS detector at the HERA collider and had an integrated luminosity of $82\,\mathrm{pb}^{-1}$. The center-of-mass energy was $\sqrt{s} = 318\,\mathrm{GeV}$. The phase space was defined by $10^{-4} < x_{\mathrm{Bj}} < 10^{-2}$, $10\ \mathrm{GeV}^2 < Q^2 < 100\ \mathrm{GeV}^2$, and $0.1 < y < 0.6$. The jets were identified in the hadronic center-of-mass frame using the inclusive k_T-clustering algorithm. The cross sections were measured differentially in virtuality, Q^2, inelasticity of the photon, y, Bjorken-x, x_{Bj}, transverse energy of the jets in the hadronic center-of-mass frame, $E^{\mathrm{jet}}_{T,\mathrm{HCM}}$, and the pseudorapidity of the jets in the laboratory frame, $\eta^{\mathrm{jet}}_{\mathrm{LAB}}$. Multi-differential cross sections were measured as functions of x_{Bj} and correlations of the jet momenta in the transverse plane.

The 6m Tagger, which was reinstalled in 2003, was calibrated using the measurement of the photon energies by the Spectrometer. First measurements of the acceptance of the luminosity photon detectors where carried out.

Zusammenfassung

In dieser Arbeit wurden die Wirkungsquerschnitte der inklusiven Zwei- und Dreijet-Produktion in Tief-Inelastischer-Streuung (DIS) bei kleinem Bjorken-x gemessen und mit störungstheoretischen QCD-Rechnungen nächstführender Ordnung (NLO pQCD) verglichen. Die verwendeten Daten stammen aus den Jahren 1998 bis 2000 und wurden mit dem ZEUS Detektor am HERA Speicherring genommen. Die integrierte Luminosität für diesen Zeitraum war $82\,\mathrm{pb}^{-1}$. Die Schwerpunktsenergie betrug $\sqrt{s} = 318\,\mathrm{GeV}$. Der betrachtete Phasenraum war $10^{-4} < x_{\mathrm{Bj}} < 10^{-2}$, $10\ \mathrm{GeV}^2 < Q^2 < 100\ \mathrm{GeV}^2$, und $0.1 < y < 0.6$. Die Jets wurden im hadronischen Schwerpunktssystem (HCM) unter Verwendung des inklusiven k_T-Clustering Algorithmus rekonstruiert. Die Wirkungsquerschnitte wurden differentiell in Virtualität, Q^2, Inelastizität des Photons, y, Bjorken-x, x_{Bj}, Transversalenergie der Jets im HCM-System, $E^{\mathrm{jet}}_{T,\mathrm{HCM}}$ und der Pseudorapidität der Jets im Laborsystem, $\eta^{\mathrm{jet}}_{\mathrm{LAB}}$, gemessen. Die zweifach differentiellen Wirkungsquerschnitte wurden als Funktionen von x_{Bj} und Korrelationen der Jetimpulse in der Transversalebene gemessen.

Der 6m Tagger, der im Jahr 2003 erneut eingebaut wurde, wurde unter der Verwendung der vom Spectrometer gemessen Photonenenergien kalibriert und erste Messungen der Akzeptanz der Photondetektoren des Luminositätsmesssystems wurden durchgeführt.

Contents

List of Figures

Chapter 1

Introduction and Physics Motivation

In previous studies, multijet production in deep inelastic scattering (DIS) at HERA [2, 3] has been used to test the predictions of perturbative QCD (pQCD) over a large range of four-momentum transfer squared, Q^2, and to determine the strong coupling constant α_s [4, 5, 6, 7, 8, 9, 10, 11, 12]. At lowest-order QCD, $\mathcal{O}(\alpha_s)$, dijet production in neutral current DIS proceeds via the boson-gluon-fusion (BGF, $V^*g \rightarrow q\bar{q}$ with $V = \gamma,\ Z^0$) and QCD-Compton (QCDC, $V^*q \rightarrow qg$) processes. Events with three jets can be seen as dijet processes with an additional gluon radiation or splitting of a gluon into a quark-antiquark pair and are directly sensitive to $\mathcal{O}(\alpha_s^2)$ QCD effects. The higher sensitivity to α_s and the large number of degrees of freedom of the trijet final state make further tests of the QCD predictions possible.

In this analysis, the multi-differential cross sections and angular jet correlations for dijet and trijet production in the hadronic center-of-mass (HCM) frame are measured with high statistical precision in the kinematic region defined by $10\,\mathrm{GeV}^2 < Q^2 < 100\,\mathrm{GeV}^2$, $10^{-4} < x_{\mathrm{Bj}} < 10^{-2}$ and $0.1 < y < 0.6$. The results are compared with perturbative QCD (pQCD) calculations at next-to-leading order (NLO). Multijet production at low Bjorken-x, x_{Bj} [13], is a particular interesting region to study parton dynamics.

In the usual QCD factorization approach, the cross sections are obtained as the convolution of perturbative matrix elements and parton densities evolved according to the DGLAP evolution equations [14, 15]. These equations resum to all orders the terms proportional to $\alpha_s \log Q^2$ and the double logarithms $\log Q^2 \log 1/x$, where x is the fraction of the proton momentum carried by a parton, which is equal to x_{Bj} in the quark-parton model. In the DGLAP approach, the parton participating in the hard scattering is the result of a partonic cascade ordered in transverse momentum, p_T. The partonic cascade starts from a low-p_T and high-x parton from the incoming proton and ends up, after consecutive branching, in the high-p_T and low-x parton entering in the hard scattering. This approximation has been tested extensively at HERA and was found to describe well the inclusive cross sections [10, 16] and jet production [2, 17, 18, 7, 19, 3, 9]. At low x_{Bj}, where the phase space for parton emissions increases, large terms proportional to $\alpha_s \log 1/x$ may spoil the accuracy of the DGLAP approach. In this region the transverse momenta and angular correlations between partons produced in the hard scatter may be sensitive to effects beyond DGLAP dynamics. The information about cross sections, transverse energy, E_T, and angular correlations between the two leading jets in multijet production therefore provides an important testing ground for studying the parton dynamics in the region of small x_{Bj}.

Recent studies [20] by the H1 collaboration compared multi-differential cross sections with NLO QCD DGLAP-based predictions in the low-Q^2 and low-x_{Bj} region. Reasonable agreement between data and the theoretical calculations was found, except for the azimuthal correlation between jets, where the NLO QCD predictions failed to describe the data.

In this analysis, correlations for both azimuthal and polar angles, and correlations in jet transverse energy and momenta for dijet and trijet production in the hadronic ($\gamma^* p$) center-of-mass (HCM) frame are measured with high statistical precision in the kinematic region of $10\,\mathrm{GeV}^2 < Q^2 < 100\,\mathrm{GeV}^2$ and restricted to $10^{-4} < x_{\mathrm{Bj}} < 10^{-2}$. The results are compared with pQCD calculations at NLO.

Chapter 2

Theory

2.1 Introduction

The experimental results of particle physics are described by a theory called Standard Model (SM). In the SM matter is built of three families of elementary fermions. Each family consists of a charged and a neutral lepton and two quarks with charges $-1/3$ and $+2/3$. These are electron (e^-), electron neutrino (ν_e), down-quark (d) and up-quark (u) for the first family. The second family are muon (μ^-), muon neutrino (ν_μ), strange-quark (s) and charm-quark (c). Finally the third family consists of the tau lepton (τ^-, also tauon), tau-neutrino (ν_τ), bottom-quark (b, often called beauty-quark) and top-quark (t, sometimes called truth). From family to family the particles get more massive. The fundamental forces are the electromagnetic, weak and strong interactions, which are modeled by quantum field theories. QED (quantum electrodynamics) and QCD (quantum chromodynamics) describe the electromagnetic and strong interactions, respectively. The electroweak model unifies the description of the weak interaction with QED. The forces are mediated by bosons. The photon mediates the electromagnetic force, Z- and $W^\pm$-bosons the electroweak force and the 8 gluons the strong interaction. The masses of the fundamental particles are generated by the so-called Higgs-mechanism. The Higgs particle is the only particle of the SM that has not been experimentally discovered yet. The only known force that is not included in the Standard Model is gravity.

In this chapter the basics of QCD will be described. It is not the aim to lay out the complete theory, but to present the main points in the calculation of the cross sections that are compared to the experimental measurements that were carried out for this thesis.

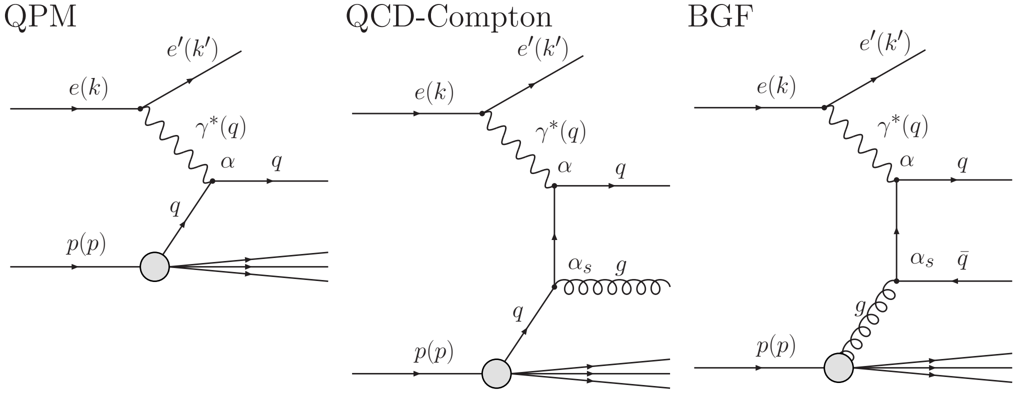

Figure 2.1: Feynman diagrams of the Quark Parton Model, QCD-Compton and Boson Gluon Fusion processes in NC DIS.

2.2 Deep Inelastic Scattering

In deep inelastic scattering (DIS) a virtual boson probes the inside of the proton. In case of neutral current (NC) DIS this boson is either a photon or a Z. In charged current (CC) DIS a $W^{\pm}$-boson is exchanged. In this analysis only NC DIS was considered, and the analyzed low-Q^2 range makes the Z-contribution negligible[1], so that only the case of the virtual photon exchange is important here.

The NC DIS process in electron(positron)[2]-proton scattering can be expressed as:

$$e^{\pm}(k) + P(p) \rightarrow e^{\pm}(k') + X$$

Where p is the four-momentum of the incoming proton and k and k' are the four-momenta of the incoming and scattered electron, respectively. X is the hadronic final state. The electron exchanges a photon of four-momentum $q = k' - k$ with the proton.

2.2.1 Kinematic Variables

The kinematics of deep inelastic scattering can be described by three variables [13]:

$$Q^2 = -q^2 = -(k' - k)^2$$

$$x_{\mathrm{Bj}} = \frac{Q^2}{2p \cdot q}$$

---

[1] $10\,\mathrm{GeV}^2 < Q^2 < 100\,\mathrm{GeV}^2$ compared to $m_Z^2 = 8315\,\mathrm{GeV}^2$

[2] In the following, the term “electron” denotes both electron and positron.

$$y = \frac{p \cdot q}{p \cdot k}$$

Q^2 is the virtuality of the photon, x_{Bj} is the momentum fraction of the parton in the proton. y is the inelasticity. In the approximation of negligible proton and electron masses, the relationship of these variables to the center of mass energy of the colliding particles is:

$$s = (k + p)^2 = 2E_e E_p = \frac{Q^2}{xy}$$

2.3 Quark Parton Model

The quark parton model (QPM) describes the hard scattering on hadrons in terms of their parton distributions. When, for instance, a virtual photon scatters on a proton, the probability that it hits a certain parton inside the proton is given by the density of that parton in the proton as a function of the kinematic variables. The parton distributions functions (PDFs) are assumed to be universal for all processes. This model was very successful in describing early deep inelastic scattering (DIS) experiments. The quantum numbers and momenta of the partons add up to the quantum numbers of the hadron. QCD is an extension to the simple QPM in that it subjects the parton coming from the hadron to the strong interaction, thus causing gluon radiation and splitting of gluons into quarks, before a parton interacts with the probing particle.

2.4 QCD

Quantum chromodynamics (QCD) is the theory of the strong interaction. The gauge symmetry group of QCD is the SU(3). Gluons mediate the force between colored particles. Analogous to the electromagnetic charge, strongly interacting particles carry "color". The name color was chosen, because it comes in three different varieties. Also, like the three basic colors red, green and blue mix to white, an object that carries equal amounts of the three types of color charge is neutral to the strong interaction. Thus baryons, e.g. the proton, consisting of three quarks of different colors, are colorless. Mesons consist of a quark and an anti-quark, which carry color and anti-color of the same type, and are also colorless. The gluons come in eight different varieties and carry color and anti-color, which do not cancel. So, unlike photons, which are electrically neutral, gluons carry the charge of the force that they mediate and can directly interact with each other via a three-gluon vertex.

One success of QCD is that it explains the property of asymptotic freedom, which is the vanishing of the coupling constant of the strong interaction at very short distances. The coupling of the strong interaction increases at higher distances. When two colored particles are separated, quark-antiquark pairs are created from the energy of the field between them and eventually quarks combine to form colorless baryons and mesons. This mechanism, which makes it impossible to observe colored particles directly, is called confinement, which, however, has not been completely proven within the theory yet. The theory of the strong interaction [21, 22, 23, 24] that was able to describe asymptotic freedom was awarded with the Nobel Prize in 2004 [25]. The phenomena of confinement and asymptotic freedom are reflected in the dependence of the coupling constant of the strong interaction, α_s, on the energy scale of the process. At higher energies, which relate to smaller distances, α_s gets smaller. This is opposite to the behavior of the fine-structure constant, α, in electromagnetic interactions. This can be explained by the different properties of the mediating bosons. Photons are electrically neutral and splits into virtual electron-positron pairs that partially screen the electromagnetic field of a charged particle at larger distances. Gluons, on the other hand, carry color and anti-color that do not cancel. The cloud of virtual gluons between colored particles enhances the effective coupling at larger distances, leading to an "antiscreening" effect.

In perturbative QCD (pQCD [26]) cross sections are calculated up to a certain order of α_s. For these calculations to be reliable, α_s must be small enough so that the omission of higher orders is not so significant. This is the case at larger scales μ, where $\alpha_s(\mu)$ becomes smaller. The order of α_s is related to the number of vertices of the strong interaction in the considered Feynman diagrams. For instance the QCD-Compton and BGF processes, Fig. 2.1, are of first order in α_s. The number of orders is often referred to as leading (LO) or next-to-leading (NLO) order. This notation depends on the final state that is considered. The aforementioned processes are LO for dijet production. The NLO includes Feynman diagrams with an additional parton radiation or an internal gluon line.

When integrating over the phase space, the momenta in the loops have to be integrated to infinity. This would lead to diverging cross sections. These are called ultraviolet (UV) divergencies. To remove these divergencies, the integral is only calculated up to some scale, which is called renormalization scale, μ_r. This scale is not a prediction of the theory, but has to be chosen. When all orders of α_s are taken into account, the resulting cross sections do not depend on μ_r, while in practical calculations that sum up only a few orders, the dependence on the choice of the renormalization scale introduces an uncertainty.

2.4.1 DIS Cross Section

The DIS cross section can be described by this formula:

$$d\sigma = \frac{4\alpha^2}{s}\frac{d^3k'}{2|\vec{k'}|}\frac{1}{(q^2 - M_V^2)^2}L^{\mu\nu}(k,q)W_{\mu\nu}(p,q)$$

$L^{\mu\nu}$ and $W_{\mu\nu}$ are the lepton and hadron tensors. The lepton tensor can be calculated from quantum electrodynamics (QED) and describes the emission of the virtual photon by the electron. The hadron tensor is defined as:

$$W_{\mu\nu} = \frac{1}{4\pi}\int d^4x e^{iqx}\sum_X \langle 0|J_\mu(0)|A(p), X\rangle\langle A(p), X|J_\nu^\dagger(x)|0\rangle$$

In terms of the structure functions, the differential cross section for unpolarized ep scattering $d^2\sigma/dxdQ^2$ can be written as:

$$\frac{d^2\sigma}{dxdQ^2} = \frac{4\pi\alpha^2}{xQ^4}\left[y^2xF_1(x,Q^2) + (1-y)F_2(x,Q^2) \mp y(1-\frac{y}{2})xF_3(x,Q^2)\right]$$

where the F_i are the structure functions. The structure functions can be related to the parton distributions (PDFs). At zeroth order QCD the relationship is described by these simple formulas:

$$F_1(x,Q^2) = \frac{1}{2}\sum_i e_i^2\left[q_i(x,Q^2) + \overline{q}_i(x,Q^2)\right]$$

$$F_2(x,Q^2) = \sum_i e_i^2\left[xq_i(x,Q^2) + x\overline{q}_i(x,Q^2)\right]$$

The structure function F_3 is related to the parity violation and is only relevant at scales where the weak interaction comes into play. For photon exchange F_3 is zero. The $q_i(x,Q^2)$ are the parton distribution functions for parton i in the proton.

2.4.2 Parton Distribution Functions (PDFs)

The PDFs cannot be calculated in perturbative QCD (pQCD) but have to be determined from experiment. The PDFs are supposed to be universal for all processes. The PDFs can be parametrized in different ways. This one is used by the CTEQ project:

$$xf(x,Q_0) = A_0x^{A_1}(1-x)^{A_2}P(x)$$

$$P(x) = (1 + A_3x^{A_4})$$

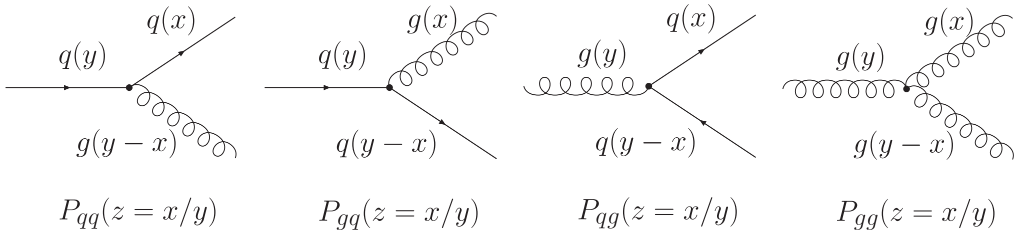

Figure 2.2: Diagrams of the QCD splitting functions

The parameter A_0 gives the normalization, while A_1 and A_2 mainly determine the low- and high-x behavior. The function $P(x)$ is purely phenomenological and chosen to give the best description of the data. There is a set of parameters for every type of parton. With the evolution equations the PDFs can be evolved to different values of Q^2.

2.4.3 DGLAP

The DGLAP (named for Dokshitzer, Gribov, Lipatov, Alterelli, Parisi) equations [14, 15] are one way to evolve the parton distributions:

$$\frac{dq_i(x,Q^2)}{d\log Q^2} = \frac{\alpha_s}{2\pi}\int_x^1 \frac{dy}{y}\left[q_i(y,Q^2)P_{qq}\left(\frac{x}{y}\right) + g(y,Q^2)P_{qg}\left(\frac{x}{y}\right)\right]$$

The $q_i(x,Q^2)$ are the distribution functions of the quark flavors i, $g(x,Q^2)$ is the gluon distribution.

$$\frac{dg(x,Q^2)}{d\log Q^2} = \frac{\alpha_s}{2\pi}\int_x^1 \frac{dy}{y}\left[\sum_i q_i(y,Q^2)P_{gq}\left(\frac{x}{y}\right) + g(y,Q^2)P_{gg}\left(\frac{x}{y}\right)\right]$$

The $P_{kl}(z)$, Fig. 2.2, are the splitting functions for a parton l splitting into a parton k with momentum fraction z. When the parton distributions are evolved according to the DGLAP prescription, the terms with logarithms of Q^2 are kept.

2.4.4 BFKL

While the DGLAP evolution equation sums the terms containing $\log(Q^2)$, it neglects the terms with $\log(1/x)$. At medium to high Q^2 this approach has been quite successful. But at low x, $\log(1/x)$ terms could be important. An alternative to the DGLAP evolution is the BFKL (Balitsky, Fadin, Kuraev, Lipatov) evolution [27], which sums the terms containing $\log(1/x)$:

$$\frac{df(x,k_T^2)}{d\log(1/x)} = \frac{3\alpha_s}{\pi} k_T^2 \int_0^\infty \frac{dk_T'^2}{k_T'^2} \left[\frac{f(x,k_T'^2) - f(x,k_T^2)}{|k_T'^2 - k_T^2|} + \frac{f(x,k_T^2)}{\sqrt{4k_T'^4 + k_T^4}} \right]$$

The BFKL evolution needs the unintegrated gluon distribution $f(x,k_T^2)$, which is related to the gluon distribution $g(x,Q^2)$ by the following equation:

$$xg(x,Q^2) = \int_\mu^{Q^2} \frac{dk_T^2}{k_T^2} f(x,k_T^2)$$

As the BFKL evolution keeps the terms in $\log(1/x)$ it is expected to work better at low-x. Unfortunately there was no program available to calculate cross sections of arbitrary multijet configurations in the BFKL formalism.

2.4.5 Next-to-Leading-Order Calculations

NLO calculations calculate cross sections with one order of α_s more than is required to get the desired final state. For instance, to produce two jets, you need one order of α_s to either radiate a gluon from the initial quark or to split the initial gluon into two partons. The additional order of α_s allows for either another radiated gluon or a virtual loop. So a NLO-calculation of dijet cross sections calculates terms up to the order of two in α_s. For trijets α_s has to be taken into account up to the order of three.

The NLO calculations for comparison with the measurements of this analysis were carried out with NLOJET [28]. It was shown [29, 30] to yield the same results as DISENT [31] for dijets and can additionally calculate trijets at NLO. NLOJET computes the dijet (trijet) cross sections to next-to-leading order, i.e. including all terms up to $\mathcal{O}(\alpha_s^2)$ ($\mathcal{O}(\alpha_s^3)$). In certain regions of the phase space, where the two hardest jets are not balanced in transverse momentum, NLOJET provides calculations for dijet production at $\mathcal{O}(\alpha_s^3)$.

NLOJET implements the $\overline{\text{MS}}$ [32] scheme for five massless quark flavors. The CTEQ6 [33] PDFs were used. The renormalization and factorization scales were both chosen to be $(\bar{E}_T^2 + Q^2)/4$, where $\bar{E}_T$ is the average transverse energy of the two (three) highest E_T jets of the given event for dijets (trijets). This choice was the same as in [2]. The value chosen for the strong coupling constant was $\alpha_s(M_Z) = 0.118$, and evolved according to the two-loop solution of the renormalization group equation.

2.5 Jets in QCD

Because of the color confinement partons cannot be directly observed. After being produced in the hard scattering the partons fragment into colorless hadrons. The exact mechanism of hadronization can only be described phenomenologically. The hadrons that emerge from this process can be detected. To compare the measurement at detector level and predictions at hadron and parton level, jets are reconstructed from the energy depositions in the detector and from the simulated particles. A jet combines a spray of collimated particles into one object. That has to be done in a way that the resulting observables are infrared and collinear safe.

- An observable is infrared safe, if it is insensitive to the additional emission of a low-energy particle. The value of the observable should not change for the transition of a $n-$parton configuration to a $(n+1)$-parton configuration with an additional parton of very low energy.

- An observable is collinear safe, if its value does not change when a pair of collinear particles is replaced with a single particle carrying the momentum sum.

The longitudinally-invariant k_T-clustering algorithm [35, 36], was used in this thesis to reconstruct the jets , see chapter 6.3.1.
NLO calculations depend on the cancellation of diagrams with positive and negative weights. The phase space has to be chosen in a way that the diagrams of one class that are supposed to cancel the contribution from another class of diagrams are not removed. The loop diagrams at NLO partially cancel the LO diagrams. But the diagrams with additional QCD radiation would be suppressed, if the selection favored a symmetry of the transverse energy of the jets, leading to unphysical results of the calculation. In order to avoid this problem, an asymmetric jet energy cut was applied in this analysis. Alternatively one could have chosen to apply a cut on the invariant mass of the jet system. This problem does not appear with trijets, but for better comparability the cuts on the first two jets were kept asymmetric for the trijet sample.

Chapter 3

Monte Carlo Models and Event Simulation

3.1 Introduction

The Monte Carlo method is used to generate events at parton and hadron level and to study the detector response. While perturbative QCD calculations, like in the program NLOJET, calculate cross sections only at the parton level, Monte Carlo generators simulate events at the parton and hadron levels. These hadrons are put through a simulation of the detector. The result of this simulation can be directly compared to the events observed in the detector. The availability of both the hadron level and the detector level of the generated events allows for a correction of the data that was taken with the actual detector. As the Monte Carlo technique is also used for simulating the fragmentation of partons into hadrons (also called hadronization), the comparison of hadron and parton level allows to extract correction factors for the correction of the parton level cross sections from the perturbative QCD calculation. Figure 3.1 illustrates the different levels at which events are analyzed.

Two different Monte Carlo generators, ARIADNE and LEPTO, were used in this analysis. Both use leading-order (LO) matrix elements (ME) for the hard process. That means that, in addition to the quark parton model (QPM) process, the QCD-Compton (QCD-C) and boson gluon fusion (BGF) processes are included. These processes generate one or two hard partons in addition to the proton remnant. To approximate higher orders, which lead to more partons in the partonic final state, LEPTO generates parton showers while ARIADNE employs the Color Dipole Model. With these models soft parton radiations, which cannot be perturbatively calculated, are approximated.

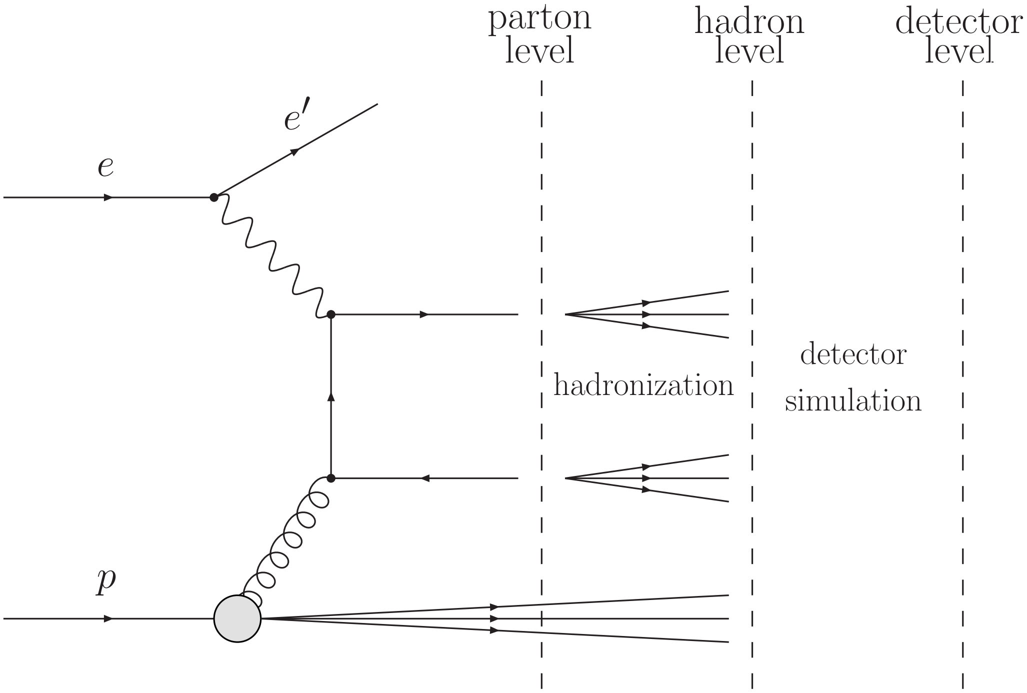

Figure 3.1: Illustration of the different levels at which the MC events are analyzed.

3.2 QED and DJANGO/HERACLES

The interaction between the electron and the parton via exchange of a virtual boson is described by the electroweak theory. The program HERACLES [37] calculates higher order corrections, which include initial and final state radiation and virtual boson loops. For the event samples that were used here, the higher order correction for the weak interaction was switched off. The programs LEPTO and ARIADNE were interfaced with DJANGO [38] to HERACLES. The QED corrections were switched on for the main samples that were used for the detector acceptance corrections. Additional LEPTO samples were generated to study the effect of the QED corrections, see chapter 8.7.

3.3 LEPTO (Parton Showers)

LEPTO [39] uses the leading-log Q^2 parton shower approach. Initial and final state parton emissions, which take place before and after the hard interaction with the boson, are simulated. The initial state parton shower is evolved backward from the parton that interacts with boson in the hard process with decreasing virtualities to the on-shell parton from the incoming proton. In the final state parton shower more partons are produced until the virtualities of the partons are below some cutoff of typically $1\,\mathrm{GeV}^2$.

3.4 ARIADNE (Color Dipole Model)

The ARIADNE program [40] implements the Color Dipole Model (CDM), illustrated in Fig. 3.2. In the Color Dipole Model (CDM) the parton cascade is simulated by the emission of gluons in the color dipole field between the color charges of the partons, analogous to the emission of photons in electromagnetic dipole radiation. The cascade starts with the color dipole between the struck parton and the proton remnant. Between the emitted and the other partons additional dipoles are formed. The gluons can also split into quark-antiquark pairs. Further emissions are generated until some cut-off scale is reached.

3.5 Hadronization Model

Both Monte Carlo Programs use the Lund string model as implemented by JETSET [41] to simulate the fragmentation of the partons into hadrons.

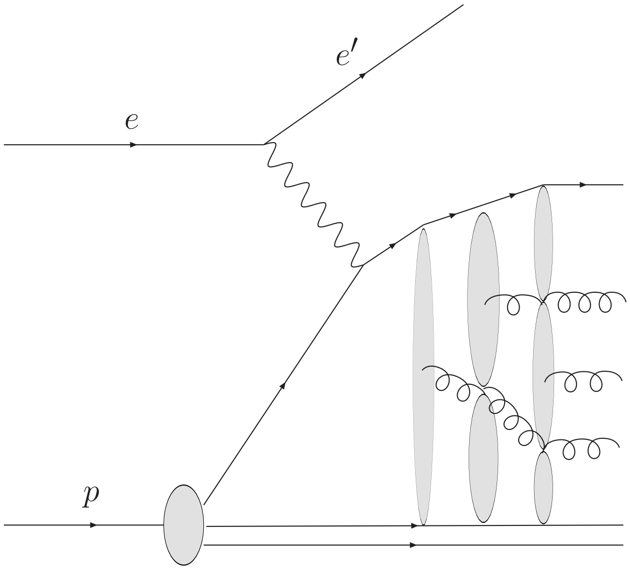

Figure 3.2: Color Dipole Model

When two partons move apart, the energy in the color field between them increases. If the energy gets high enough, the connecting 'string' will break. From the energy of the field quark-antiquark pairs are produced. Each of these partons becomes the end of a smaller substring. Eventually the partons combine and form colorless hadrons.

3.6 Detector Simulation

The output of the Monte Carlo programs is a list of stable particles. These particles are the input for the detector simulation. The detector simulation simulates the interaction of the particles with the detector. The ZEUS detector is simulated by the program MOZART, which is based on GEANT [42]. The trajectories of the particles are traced through the detector. The signals of the detector components are simulated to give responses similar to the ones of the actual detector. Based on the result of the detector simulation the trigger is simulated by the program ZGANA.

Chapter 4

Experiment

4.1 DESY

DESY [43] (Deutsches Elektronen Synchroton, German Electron Synchroton) was founded in Hamburg, Germany, in 1959 as a high energy physics laboratory.

4.2 HERA

The HERA (Hadron-Elektron Ring Anlage) collider at DESY is the first and only lepton-hadron beam collider in the world. It has a circumference of 6.3 km and is located 10 m – 25 m underground. Protons with an energy of 920 GeV[1] are collided with either positrons or electrons of 27.5 GeV. This results in a center of mass energy of 318 GeV. Before HERA the proton structure was tested in fixed target experiments. They had a much smaller center of mass energy, because the center-of-mass system of the interacting particles was strongly boosted into the direction of the accelerated particle. Protons and electrons go through several preaccelator stages until they are injected into HERA and accelerated to their final energies.
The maximum energy of the proton beam is limited by the bending power of the magnetic field that keeps them on their orbit. For this purpose 422 superconducting dipole magnets with 5.1 T are used at HERA. The superconducting magnets have to be cooled down to 4.0 K. The maximum electron energy is limited by the energy loss due to synchroton radiation. The electrons are kept in their orbit with conventional magnets.
As mentioned before, HERA can collide protons with electrons or positrons.

---

[1] Until 1997 the proton energy was 820 GeV.

For the acceleration these are in principle the same, only the polarity of the electromagnetic fields has to be inverted and the orbits in the interaction regions are slightly different, because the two colliding beams have to be brought together and separated. At HERA the beams are each organized into 220 bunches. Of these, up to 210 are filled with particles. The time between the bunches is 96 ns, this corresponds to 28.8 m. The projected luminosity for HERA I was $1.5 \times 10^{31}\,\mathrm{cm}^{-2}\mathrm{s}^{-1}$.

There are four interaction regions at HERA. At the ZEUS and H1 experiments the beams are brought to collision while HERMES and HERA-B[2] are fixed target experiments and use only either the electron beam or the proton beam, respectively.

4.3 ZEUS

ZEUS [44] is a general purpose detector, designed for the measurement of particle collisions at HERA. It is located in the south hall of the HERA ring. Its main components are the Uranium Calorimeter (CAL), which provides an almost complete coverage of the solid angle, and the Central Tracking Detector, CTD.

4.3.1 Central Tracking Detector (CTD)

The main tracking detector of ZEUS is the CTD [45]. The CTD is a 240 cm long cylindrical drift chamber with an active length of 205 cm. It covers the radius from 16.2 cm to 85 cm around the beam pipe. The CTD consists of 72 cylindrical sense wire layers, organized in 9 superlayers covering the polar-angle region of $15^\circ < \theta < 164^\circ$. The wires of the odd-numbered superlayers are parallel to the beam axis. The even-numbered superlayers have small stereo angles of $\pm 5^\circ$ with respect to the beam axis. The gas in the CTD is a mixture of argon, carbon dioxide and ethane.

Charged particles that pass through the CTD ionize the gas. The electrons drift to the sense wires where they are amplified and cause electric signals. Tracks are reconstructed from these hits. A magnetic field of 1.43 T bends the trajectories of the charged particles that pass through. The curvature of the reconstructed tracks gives information about their charge and momentum. The relative transverse-momentum resolution for tracks going through all superlayers is $\sigma(p_T)/p_T = 0.0058 p_T \oplus 0.0065 \oplus 0.0014/p_T$, with p_T in GeV.

The forward (FTD) and rear (RTD) tracking detector extend the tracking into the forward and rear regions. They have not been used in this analysis.

---

[2] The HERA-B experiment ended in 2003.

4.3.2 Calorimeter (CAL)

The calorimeter of the ZEUS detector is a uranium-scintillator-sandwich-calorimeter. It consists of three parts: the forward (FCAL), the barrel (BCAL) and the rear (RCAL) calorimeters. Each part is subdivided transversely into towers and longitudinally into one electromagnetic section (EMC) and either one (in RCAL) or two (in BCAL and FCAL) hadronic sections (HAC). The smallest subdivision of the calorimeter is called a cell. The CAL covers 99.7% of the solid angle around the interaction region. The uranium serves as absorber. The active material is the plastic scintillator SCSN-38. The advantage of using uranium is the equal response of the calorimeter to electromagnetic and hadronic energy depositions. The CAL energy resolutions, as measured under test-beam conditions, are $\sigma(E)/E = 0.18/\sqrt{E}$ for electrons and $\sigma(E)/E = 0.35/\sqrt{E}$ for hadrons, with E in GeV. The scintillator light is read out with wavelength shifters and photomultipliers. The ZEUS calorimeter is deeper in the forward (7.1 interaction lengths, λ_{int}) than in the backward ($4.0\lambda_{int}$) direction to account for the difference of the beam energies. For the initial calibration of the CAL, see [46].

4.3.3 Other Components

SRTD

The Small angle Rear Tracking Detector (SRTD [47]) consists of finely segmented scintillator strips. Its purpose is to improve the resolution of the measurement of the scattered electron at low angles around the beam pipe in the rear direction.

HES

The Hadron Electron Separator was originally designed to be used for a better distinction between hadrons and electrons in the calorimeter. Because of an underestimation of the dead material between interaction point and calorimeter it cannot serve this purpose as planned. But it is used to improve the position reconstruction of the scattered electron.

Presampler

The Presampler [48] consists of scintillator tiles in front of the calorimeter towers. According to the part of the calorimeter it is divided into Forward, Rear (PRES) and Barrel (BPRES) Presampler. The Presampler is calibrated in units of MIPS (minimum ionizing particles). Its measurement indicates

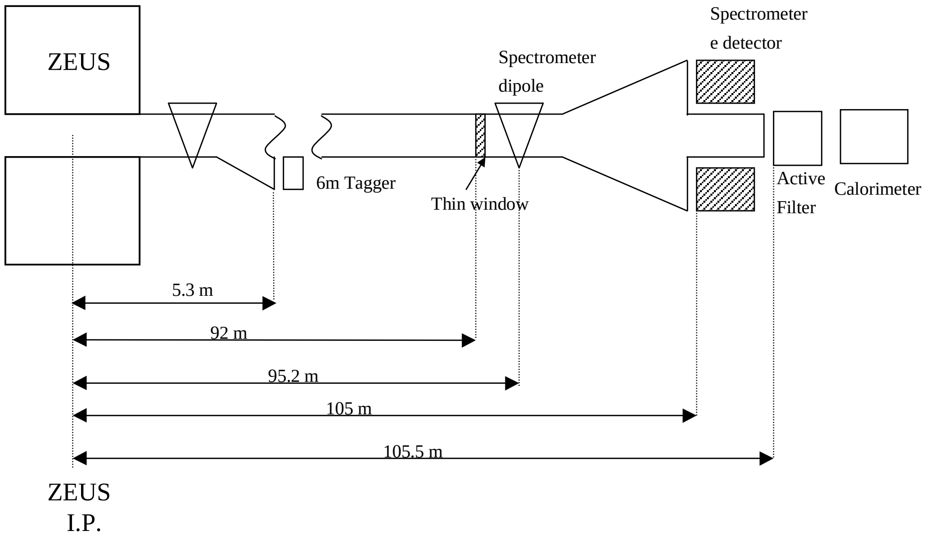

Figure 4.1: Positions of the components of the luminosity measurement system.

the multiplicity of particles. In this analysis the Presampler was only used to correct the electron energy measurement.

4.3.4 Luminosity Measurement

The luminosity is measured with the luminosity monitor, LUMI, via the bremsstrahlung process: $ep \rightarrow e'p\gamma$ The measurement of the luminosity is necessary to determine cross sections from the data. The bremsstrahlung process is well known and has a high cross section, so that it is well suited for the luminosity measurement. The photons as well as the electrons that come out of the bremsstrahlung process can be used to determine the rate. The advantage of detecting the photons is that their trajectories are not bent. After the interaction point (IP) a straight beam pipe branches off in the electron direction. This photon beam pipe leads to the photon detectors of the luminosity monitor about 100 m from the IP. The luminosity measurement system was upgraded for the HERA II running period. The multijet analysis that is described in this work was performed with data from 1998 to 2000 from the end of the HERA I running period. Part of the luminosity monitor upgrade were the Spectrometer and the 6m Tagger, which is described in more detail in chapter 5. Figure 4.1 shows where the components of the new luminosity measurement system are located.

Photon Calorimeter

The Photon Calorimeter is a lead-scintillator calorimeter 107 m from the interaction point. Located in front of it is a carbon filter. The carbon filter absorbs the high flux of low-energetic synchroton radiation photons. During the upgrade to HERA II the depth of the filter was increased to shield the Photon Calorimeter from the more intense synchroton radiation.

Spectrometer

The Spectrometer is part of the luminosity monitor upgrade for HERA II. About 10% of the photons that hit the exit window of the photon beam pipe convert into positron/electron pairs. A magnetic dipole diverts these into the lower and upper parts of the Spectrometer. The Spectrometer consists of two finely segmented tungsten-scintillator calorimeters. The light signal from the scintillating strips is read out with photomultipliers.

6m Tagger

The 6m Tagger is the electron detector of the upgraded luminosity monitor. The 6m Tagger is a sampling calorimeter with tungsten as absorber and scintillating fibers. It is located about 6 m from the interaction point in electron direction. The magnetic field that keeps the electrons of nominal energy in their orbit deflects electrons of a certain energy range into the 6m Tagger. A more detailed description of the 6m Tagger is in chapter 5.

4.3.5 Trigger and Data Acquisition

The bunch crossings take place with intervals of 96 ns. The event size is about 500 kB. The Data Acquisition System (DAQ) is not capable of storing the detector signals for every single bunch crossing and also the front-end electronics cannot be read out that fast. During most bunch crossings nothing of interest happens. The task of the trigger system is to select the interesting events. The trigger [50] of the ZEUS detector has three levels. The First Level Trigger (FLT) works synchronously to the rate of the collisions of about 10 MHz. The detector components send basic information to the Global First Level Trigger (GFLT), which decides if the event should be discarded or if the components should send further information to be processed by the next trigger level. The rate of events is reduced so that the subsequent triggers can work with a lower rate to analyze the events more completely. The Second Level Trigger (SLT) reduces the rate to about 200 Hz. The Third Level Trigger (TLT) uses a farm of computers to analyze the events that have passed through the previous trigger stages. At this level the information from all the components is combined to reconstruct the events. The output rate of the TLT is about 10 Hz. For each trigger level, several so-called trigger “slots” are defined. An event has to fulfill the requirements of at least one trigger slot to reach the next level. The Event Builder (EVB) collects the data from all the components to write the data of the selected events to a mass storage system. During the later analysis of the data, changing trigger configurations have to be taken into account to correctly simulate the efficiency, as described in chapter 7.1.

Chapter 5

6m Tagger

5.1 Introduction

The 6m Tagger [51, 52, 53] is part of the luminosity upgrade. It detects electrons from the Bethe-Heitler process used to measure the luminosity in a certain energy range with an efficiency of nearly 100%. One task of the 6m Tagger is to cross-check the acceptance of the photon detectors. Because of its ability to detect the scattered electrons from *ep* events with very low-Q^2, it can be also used to identify photoproduction events. For the measurement of the longitudinal structure function, F_L, a period of low energy running is planned. Events with high y play an important role for this measurement. The expected background from photoproduction events will be further investigated with the 6m Tagger.

5.2 Hardware and Data Acquisition

The 6m Tagger [51, 52, 53] is a sampling calorimeter, e.g. it consists of a combination of a material that absorbs highly energetic particles and causes them to shower and an active material that gives a measurable response proportional to the absorbed energy. The absorbing material is a tungsten alloy (DENSIMET). There are 85 tungsten plates of dimension $23 \times 100 \times 1\,\mathrm{mm}^3$. The plates have 22 grooves on one side and 23 grooves one the other with a radius of 0.28 mm to accommodate the fibers. The first and last plates have grooves only on one side. An illustration of the geometry of the fibers and the plates is shown in Fig. 5.1. The plates are stacked and held together with thin stainless steel strips. The active component is comprised of 1890 scintillating fibers of the type SCSF-38M. They have a diameter of 0.5 mm and are bundled in 70 channels of 27 fibers each. The front end of the fibers

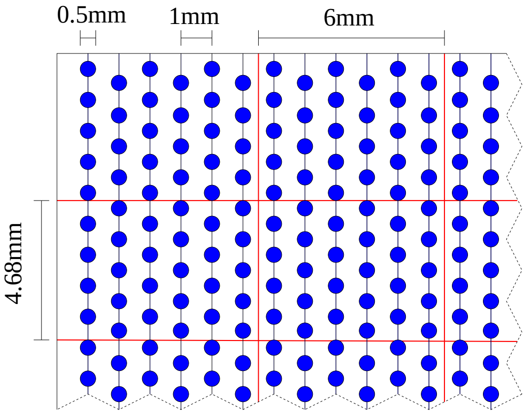

Figure 5.1: Geometry of the fibers and the tungsten plates in the 6m Tagger as seen from the front. Shown is one corner of the 6m Tagger with 2×2 complete cells. Each cell has 27 scintillating fibers, which are located in the grooves between the tungsten plates.

50	51	52	53	54	55	56	57	58	59	5A	5B	5C	5D
40	41	42	43	44	45	46	47	48	49	4A	4B	4C	4D
30	31	32	33	34	35	36	37	38	39	3A	3B	3C	3D
20	21	22	23	24	25	26	27	28	29	2A	2B	2C	2D
10	11	12	13	14	15	16	17	18	19	1A	1B	1C	1D

Figure 5.2: Layout and naming scheme of the 6m Tagger channels when looking at the front face. The fibers are parallel to the beam pipe, which is located to the left of the 6m Tagger.

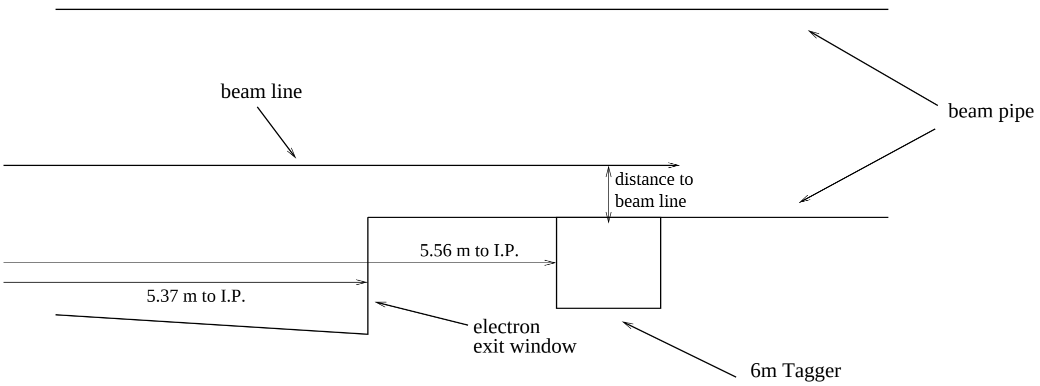

Figure 5.3: View of the 6m Tagger relative to the beam pipe from above. The electrons/positrons that hit the 6m Tagger leave the beam pipe through the exit window. The distance of the 6m Tagger to the beam line is 64.5 mm for electrons and 68.8 mm for positrons.

is polished and painted with reflective paint in order to improve the light yield. Inside the 6m Tagger the fibers are parallel to the beam pipe. The remaining length of the about 1.5 m long fibers serves as light guides to the photomultipliers. The 6m Tagger is located inside the HERA ring radius at a distance of 64.5 mm for electron running and 68.8 mm for positron running. This causes the difference in energy range of the 6m Tagger between electron and positron running. The electrons/positrons that hit the 6m Tagger leave the beam pipe through an exit window 5.37 m from the interaction point. The front face of the 6m Tagger is 5.56 m from the interaction point. The position of the 6m Tagger relative to the beam pipe is illustrated in Fig. 5.3. The vertical position of the 6m Tagger is centered around the beam line, so that it covers y from -12.5 mm to 12.5 mm.

The 70 channels are organized in 5 rows and 14 columns, the layout can be seen in Fig. 5.2. FADCs convert the photomultiplier signals into 12-bit numbers. The 14 channels of every row go to one memory board [54]. The memory boards have separate buffers for locally stored events and events that are sent to the Event Builder (EVB). The memory boards send a sum information to the trigger board, which calculates trigger sums for the GFLT and determines which local events are kept.

The electrons that hit the front face of the 6m Tagger have an incident angle of at least 3°, so that they cannot just travel largely unabsorbed through one single fiber.

on top of 6m Tagger Period	1 Dose [Gy]	2 Dose [Gy]
Dec 4. 2003 – Aug 1. 2004	18.4	4.6
Jan 8. – Feb 5. 2004	0.4	14.7
Feb 5. – Mar 3. 2004	5.2	5.3
Mar 3. – Apr 1. 2004	18.9	66.3
Apr 1. – May 6. 2004	1.0	2.3

between 6m Tagger and PMTs Period	6m Tagger Dose [Gy]	Middle Dose [Gy]	PMT Dose [Gy]
Jan 7. – Apr 5. 2006	411.5	8.9	3.0
Apr 5. – May 3. 2006	53.3	2.0	1.5
May 3. – Sep 6. 2006	91.9	5.5	3.7
Sep 6. – Dec 5. 2006	92.6	7.5	2.3

Table 5.1: Doses at the 6m Tagger measured during certain periods. The doses were measured with TLDs. From the end of 2003 to the middle of 2004 the dosimeters were placed on top of the 6m Tagger. In 2006 the dosimeters were attached to the fibers that guide the light to the photomultipliers. The label indicates the position close to the 6m Tagger, in the middle and at the photomultipliers.

5.3 Evaluation of Radiation Damage

The 6m Tagger is located very close to the beam pipe and it can be hit by scattered synchroton radiation (As it is located inside the radius of the storage ring, it is not hit by direct synchroton radiation.). A 3.3 mm thick lead plate was glued to the front of the 6m Tagger to shield the exposed ends of the fibers against the high rate of low energetic photons. The electrons and positrons of energies between 4 and 9 GeV that hit the 6m Tagger are not stopped by this lead plate. The SCSF-38M fibers used for the 6m Tagger are relatively radiation hard [55, 56, 57, 58], but the high intensity of radiation is still expected to cause a degradation of the fibers. The main effect of radiation damage to the scintillating fibers is the creation of absorption centers that deteriorate the light transmission of the fibers.

Table 5.1 shows the radiation doses at the 6m Tagger measured with thermoluminescence dosimeters (TLDs). From the end of 2003 to the middle of 2004, the dosimeters were placed on top of the 6m Tagger. These measurements show a large variation, probably because the dosimeters were not placed at

the exact same spot. For the middle of 2004 to the end of 2005, no reliable measurements of the doses exist. In 2006, the dosimeters were attached at three different positions to the part of the fibers that runs between the 6m Tagger and the photomultipliers. This measurement shows that the radiation is most intense close to the 6m Tagger, and thus close to the beam pipe, but the fibers are also exposed to a considerable radiation over their whole length. The TLDs that were used give a linear response for doses up to 10 Gy, where the uncertainty is about 5%. For the higher doses the uncertainty is about 20%.
To measure the radiation damage to the 6m Tagger, scans with a cobalt-60 source were carried out, which are presented in the next section.

5.3.1 Cobalt Scans

The system to perform the cobalt scans on the 6m Tagger was similar to the one used on the forward and rear regions of the main calorimeter [59]. To check the response of the scintillating fibers of the 6m Tagger, a cobalt-60 source was moved in guide tubes that were soldered to a frame that is attached to the 6m Tagger. The ten guide tubes are parallel to the fibers. The cobalt source is situated in the tip of a thin tube which is moved through the guide tubes by a stepping motor. So the response of the fibers can be recorded as a function of the longitudinal position of the cobalt source.

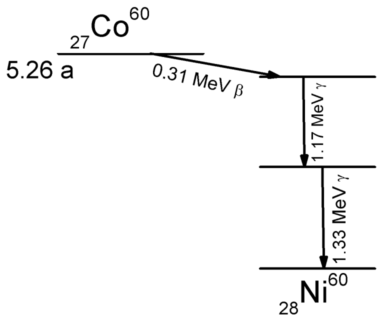

Figure 5.4: Decay of Cobalt-60

Eight of the guide tubes end at the front face of the 6m Tagger, four each underneath and on top of the 6m Tagger. Two more guide tubes are on the side of the 6m Tagger. They extend 14 cm beyond the front of the 6m Tagger and were used [57] for a measurement with the cobalt radiation coming from the front. But after the installation of the lead plate in front of the 6m Tagger the signal from there was too small to be usable, instead only the scan positions beginning at the front of the detector, analogous to the other guide tubes, were used for these tubes. Table 5.2 shows the dates of the cobalt scans and the elapsed time since the first cobalt scan. The same cobalt source was used for all the scans and its decay (half life 5.27 years, decay products shown in Fig. 5.4) was taken into account before comparing the scans from different dates. The activity of the cobalt source at the time of the last cobalt scan in December 2006 was about 30 MBq. For the cobalt scans the output of the photomultipliers was connected to the ADC cards of a portable computer and the high voltage was set to the values of the first cobalt scan. For every scan pedestal values without cobalt irradiation were taken in order to be subtracted from the values measured during the scan.

No. of Scan	Date	Time [d]
1	Dec 4. 2003	0
2	Feb 5. 2004	63
3	May 6. 2004	154
4	Jun 3. 2004	182
5	Aug 16. 2004	256
6	Jan 5. 2005	398
7	Apr 13. 2005	496
8	Dec 7. 2005	734
9	May 2. 2006	880
10	Sep 6. 2006	1007
11	Dec 12. 2006	1098

Table 5.2: Dates of the cobalt scans and elapsed time since the first measurement in days.

5.3.2 Results

Results from the cobalt scans were also presented in [60]. Cobalt scans on the 6m Tagger before 2003 were analyzed in [57]. To determine which guide tube should be used for each channel of the 6m Tagger, the integrated signal over the scan length was determined, Fig. 5.6. In the first cobalt scan, several dead channels were found, Fig. 5.5, which were repaired afterwards. The first cobalt scan was not used further on, instead the second scan was used as a reference for the later scans. During the latest scan (December 2006), the scan could not be carried out with all guide tubes. Channel 44 was broken until scan 3 and the dark current of channel 5B was increasing with time,

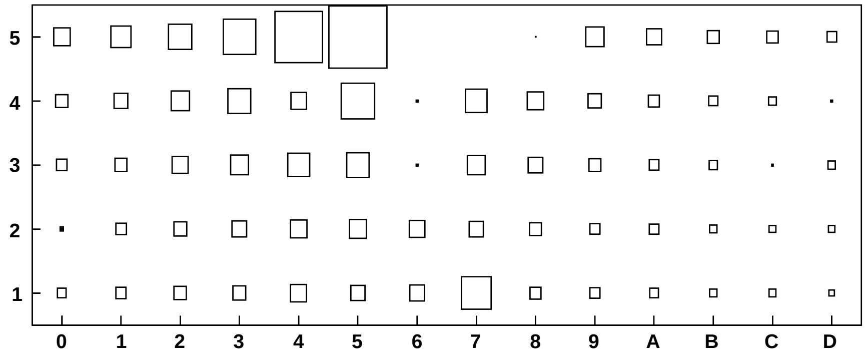

Figure 5.5: The integrated signal of the first cobalt scan with the second guide tube on the top. The sizes of the boxes indicate the relative signal in the channels of the 6m Tagger. Several dead channels can be seen that were repaired afterwards.

which could not be compensated by the pedestal subtraction. Examples of the cobalt scan signals as a function of the source position are shown in Fig. 5.7. Typically the signal is rising steeply from 0 mm to 20 mm, then it is increasing slightly until the slope starts to rise again after 80 mm. At the beginning (position 0 mm), the 6m Tagger is only hit by the radiation from the cobalt source with a quarter of the full solid angle, so it rises to a plateau of about twice that value when it is hit by almost half of the radiation of the cobalt source. Figure 5.8 illustrates this. The behavior at the the last 20 mm is influenced by the irradiation of the part of the fibers that is coming out of the 6m Tagger, where they are not shielded by the tungsten. This leads in most cases to a steeper increase in signal.

In Fig. 5.9 the signal is normalized to the second scan. A stronger reduction of the signal is observed for the channel closest to the beam. For the analysis of the development of the radiation damage versus time, it was chosen to look at the signals at 10 mm and 90 mm from the front. Under the assumption that the primary yield is not affected, the reduction in signal between these points can be attributed to the attenuation of the light due to absorption. For the estimation of the radiation damage to the fibers inside the 6m Tagger, the ratio of these two values is taken. For the damage to the outside part of the fibers, the value from 90 mm is compared. The shown relative signals are defined as

$$\text{relative signal}_{\text{inside}} = (\text{signal}_{\text{10mm}}/\text{signal}_{\text{90mm}})/(\text{signal}_{\text{10mm,2.scan}}/\text{signal}_{\text{90mm,2.scan}})$$

$$\text{relative signal}_{\text{outside}} = \text{signal}_{\text{90mm}}/\text{signal}_{\text{90mm,2.scan}}.$$

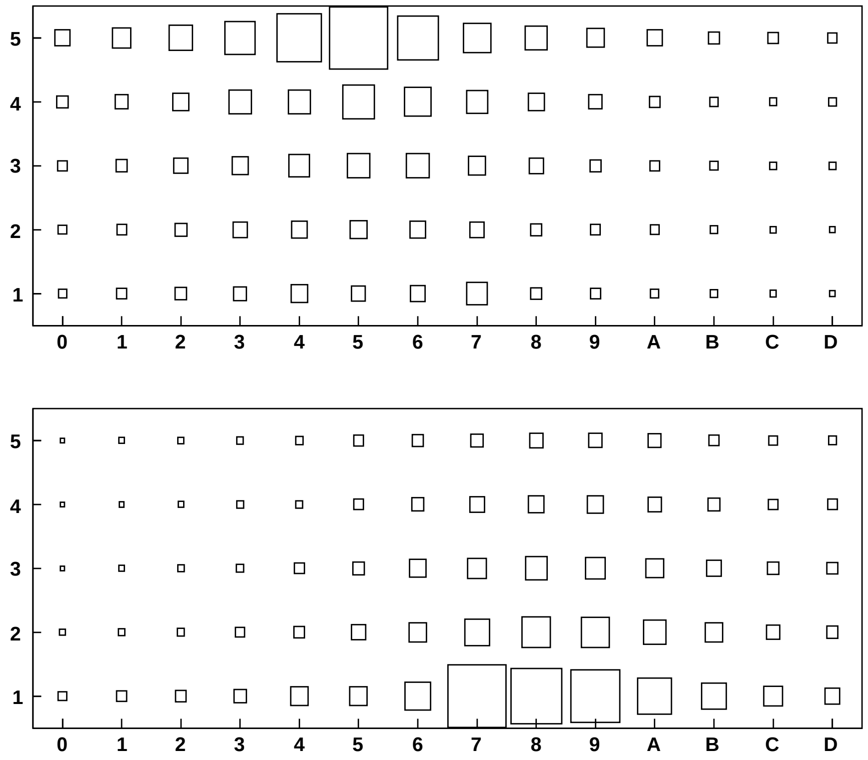

Figure 5.6: The integrated signal of the fourth cobalt scan. The sizes of the boxes indicate the relative signal in the channels of the 6m Tagger. The upper plot shows the signals from the second guide tube on the top of the 6m Tagger, the lower one the signals of the third tube on the bottom.

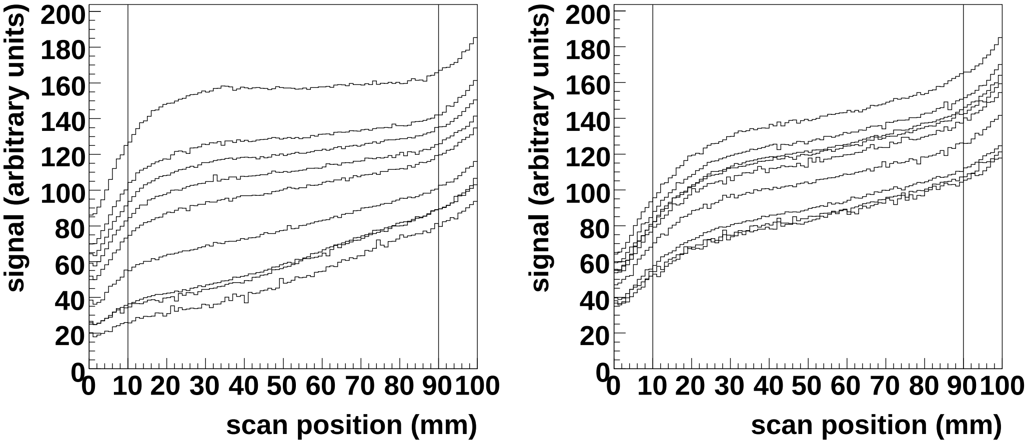

Figure 5.7: 6m Tagger cobalt scan. The signal as a function of the scan position is shown for the scans 2 to 10. The signal decreases from scan 2 to scan 10. On the left is channel 30, on the right channel 3A. Both channels are in the center row. Channel 30 is the channel closest to the beam.

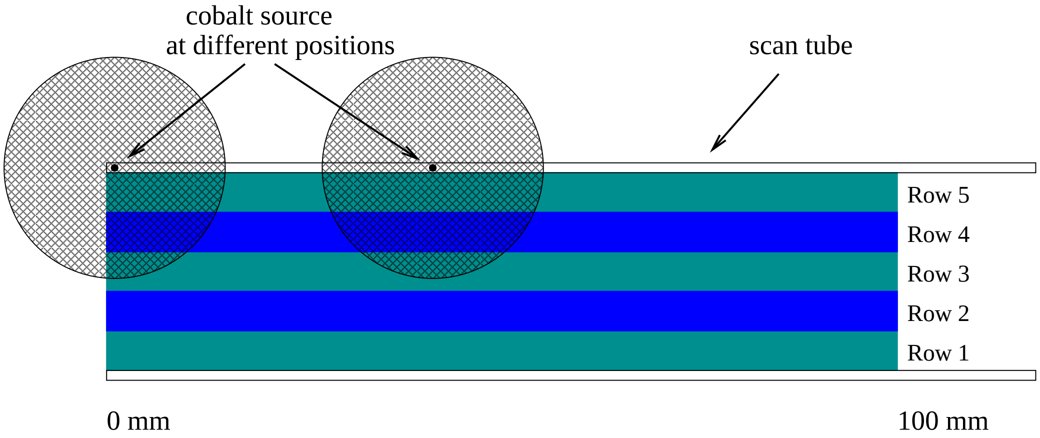

Figure 5.8: Side view of the 6m Tagger during the cobalt scan. This drawing illustrates why the signal at source position 0 mm is about half compared to the signal from the source in the center.

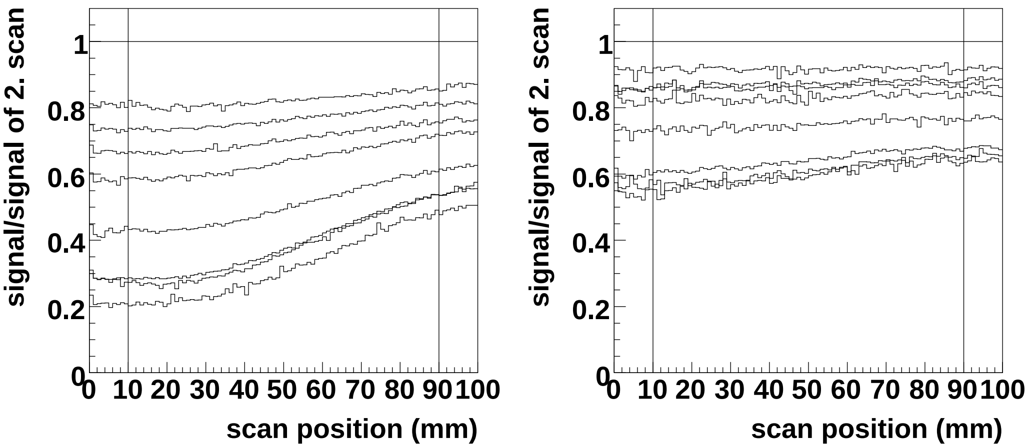

Figure 5.9: 6m Tagger cobalt scan. The relative signal as a function of the scan position is shown for the scans 2 to 10. The scans are normalized to scan 2. The signal decreases from scan 2 to scan 10. On the left is channel 30, on the right channel 3A. Both channels are in the center row. Channel 30 is the channel closest to the beam. A stronger reduction of the signal can be seen for the channel closest to the beam. The vertical lines indicate the reference positions for the evaluation of the development of the signal vs. time.

The relative damage is defined as

$$\text{relative damage}_{\text{inside/outside}} = 1 - \text{relative signal}_{\text{inside/outside}}.$$

The development of the damage outside the 6m Tagger, Figs. 5.11, 5.13 and 5.15, shows a very similar behavior for all the channels. Inside the 6m Tagger, Figs. 5.10, 5.12 and 5.14, the fibers of the channels that are closest to the beam pipe show the largest damage. This is where more and higher energy electrons hit the 6m Tagger. Figures 5.10 and 5.11 show a comparison between two different channels and Figs. 5.12–5.15 give an overview of all the channels in the 6m Tagger. The damage outside seems to come from scattered synchroton radiation or other radiation background, while the fibers inside are screened from background radiation by the tungsten. The damage profile of the fibers that are most affected by the electrons is compatible with the longitudinal shower profile of these electrons [60]. In April 2006, lead shielding was installed between the beam pipe and the 6m Tagger to add protection for the exposed fibers. This measure seems to have prevented some damage to the outside fibers of the 6m Tagger in the last two (May and September 2006) presented scans. Further cobalt scans are planned to

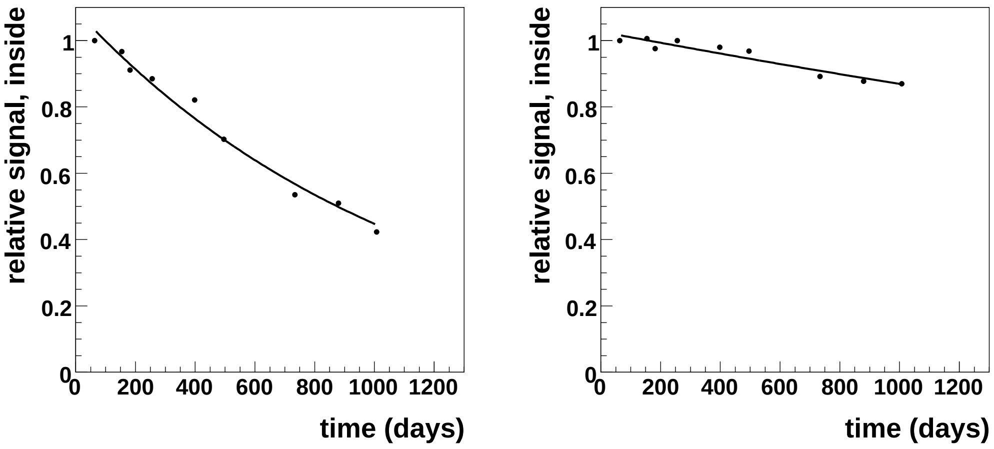

Figure 5.10: Development of the relative signal inside the 6m Tagger vs. time. On the left is channel 30, on the right channel 3A. Both channels are in the center row. Channel 30 is the channel closest to the beam. An exponential function is fitted to the points and shown as a line. The channel closest to the beam shows a significantly stronger reduction in signal inside the 6m Tagger.

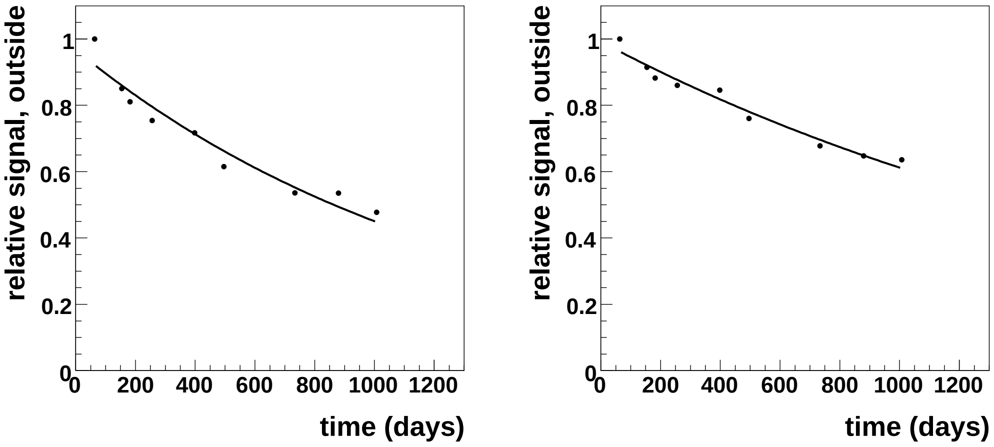

Figure 5.11: Development of the relative signal outside the 6m Tagger vs. time. On the left is channel 30, on the right channel 3A. Both channels are in the center row. Channel 30 is the channel closest to the beam. An exponential function is fitted to the points and shown as a line. Compared to the damage inside the 6m Tagger, Fig. 5.10, both channels show a much more similar behavior.

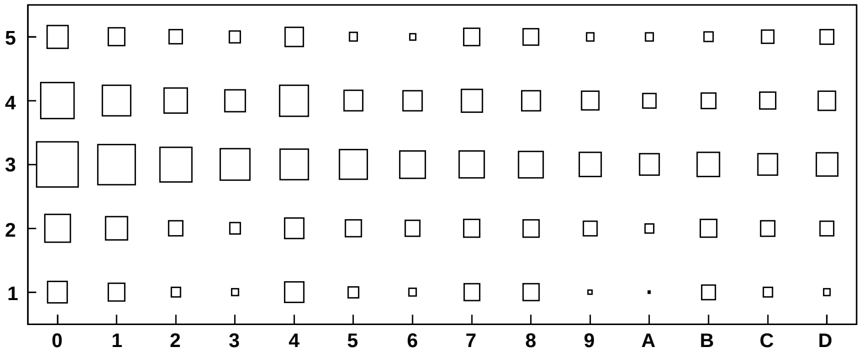

Figure 5.12: Relative damage to the fibers inside the 6m Tagger. The sizes of the boxes indicate the damage (1-relative signal) to the fibers inside the 6m Tagger between the cobalt scans number 2 and 10. The damage is concentrated in the center row and to the side closest to the beam pipe. For a more quantitative overview, see Fig. 5.14.

monitor the development of the radiation damage to the 6m Tagger until the termination of the ZEUS experiment in July 2007.
Although the damage to the fibers of the 6m Tagger is severe, the results of the calibration, as described in Section 5.5, show that the energy resolution deteriorated only slightly.

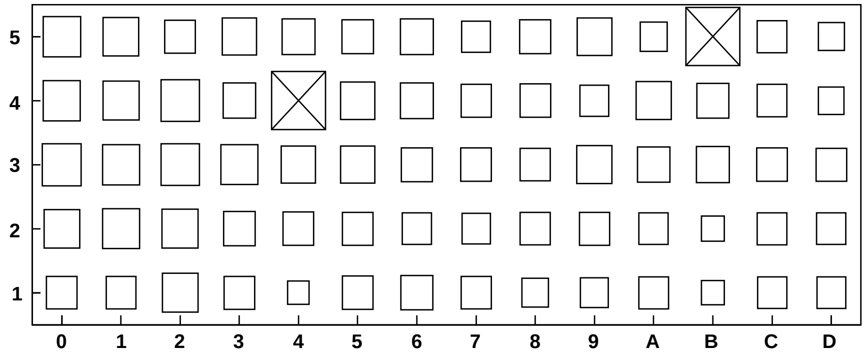

Figure 5.13: Relative damage to the fibers outside the 6m Tagger. The sizes of the boxes indicate the damage (1-relative signal) to the fibers outside the 6m Tagger between the cobalt scans number 2 and 10. The damage is uniformly distributed over all the channels. Channels 44 and B5 could not be reliably compared, which is explained in the text. For a more quantitative overview, see Fig. 5.15.

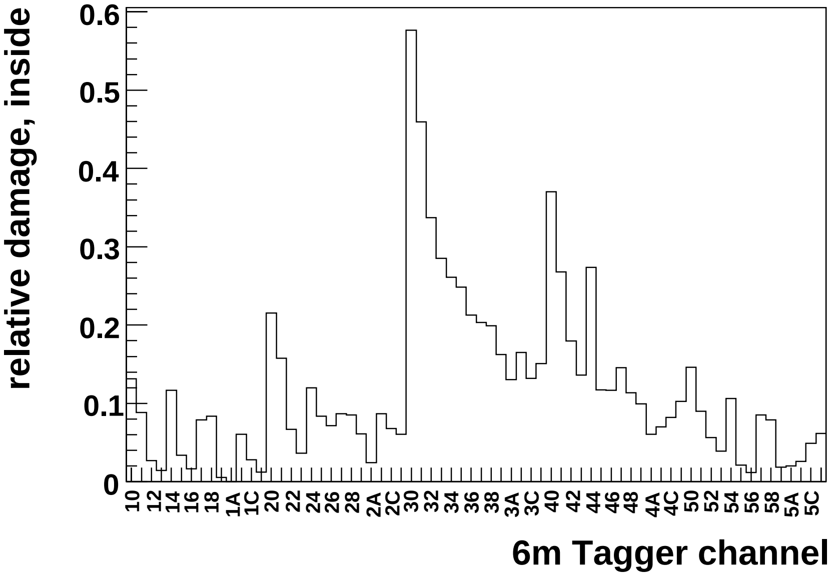

Figure 5.14: Relative damage to the fibers inside the 6m Tagger. Further description can be found in Fig. 5.12.

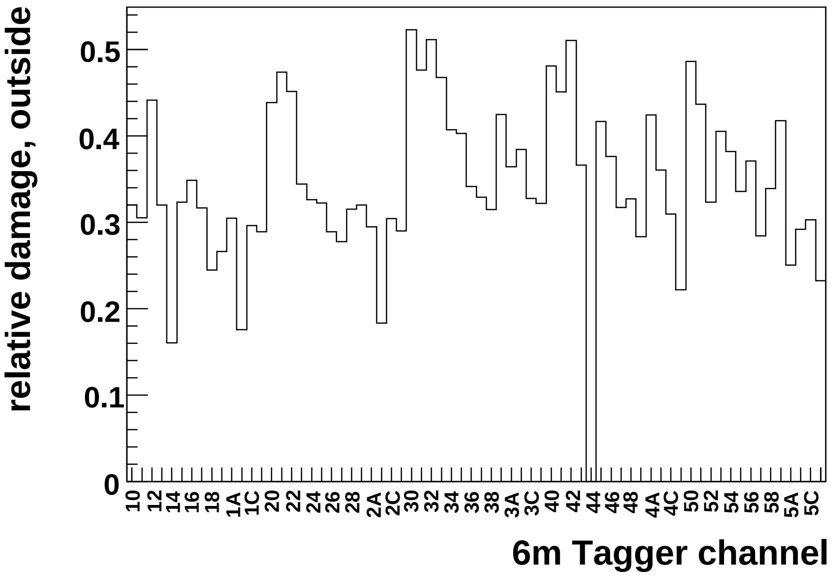

Figure 5.15: Relative damage to the fibers outside the 6m Tagger. Further description can be found in Fig. 5.13.

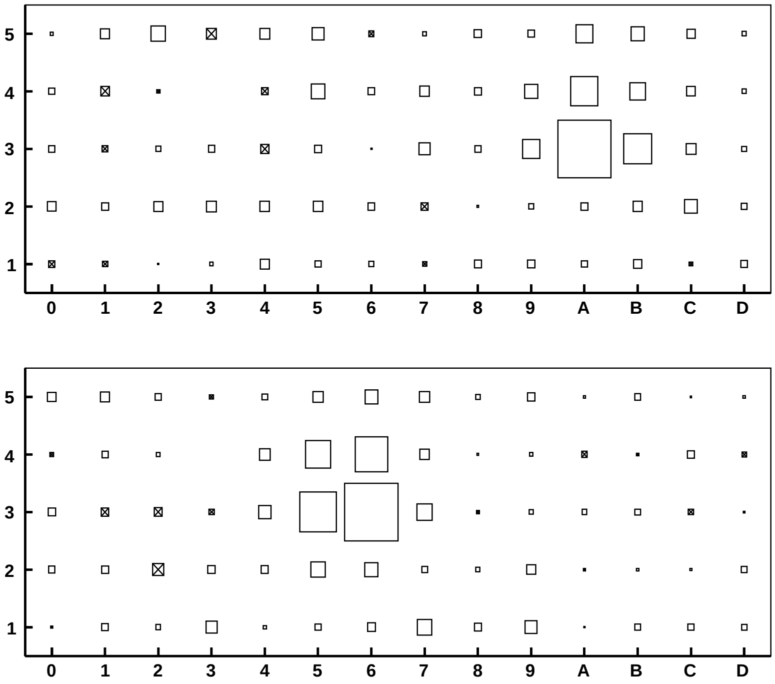

Figure 5.16: Typical 6m Tagger events. The upper picture shows an event with 6.8 GeV. The lower picture shows an event with 8.1 GeV. The sizes of the boxes indicate the relative energies in the individual cells. The boxes with crosses indicate negative values, which means that the measured signals in these cells were below the pedestals.

5.4 Event Reconstruction

When an electron hits the 6m Tagger, it produces an electromagnetic shower. A fraction of the energy of the electron is absorbed in the scintillating fibers and produces light that is converted by wavelength shifters and then guided by the same fibers to the photomultipliers. In the photomultipliers the photons produce photoelectrons which are multiplied in a cascade. The photoelectrons carry a charge that flows as a current to the ADCs. So the calibration constants, which relate the ADC signals to the particle energies, are affected by a convolution of these effects.

The 6m Tagger consists of 14 × 5 cells. Each cell has a calibration constant to convert the ADC-signal to an energy in GeV. With the given calibration constants, the energy and position of the impacting electron can be reconstructed. Two typical events in the 6m Tagger are shown in Fig. 5.16. Several reconstruction methods were employed. The energy was reconstructed by adding the contents of a certain number of cells. Either 5×5, 3×3 or all 70 cells were added. The 5×5 and 3×3 regions were centered around the cell with the highest energy. When the cell with the highest energy was too close to the edges, the center was moved so that the reconstruction region was contained in the 6m Tagger. The 5×5 method was used as the best compromise between leakage and noise. Leakage is due to energy depositions from the shower outside the reconstruction region. The calibration, see next section, has been done for the 5×5 method and thus takes into account the average leakage. The position was reconstructed by taking the weighted average of 3×3 cells around the highest-energy cell. The x- and y-coordinates of the contributing cells were multiplied with their energies and the sums were divided by the 3×3 energy sum. Because of the exponential transverse shower profile, this simple method reconstructed the position too close to the center of the reconstruction region. Therefore this position reconstruction was improved by correcting [51] the result with a polynomial function.

5.5 Calibration of the 6m Tagger

Different energy reconstruction methods require different sets of calibration constants, because the size of the reconstruction region determines the average leakage outside this region. It was decided to use the 5×5-cells method. The initial calibration of the 6m Tagger was determined in a testbeam [51]. As reference for calibrating the 6m Tagger in the ZEUS experiment the energy measurement of the Spectrometer was used. The energy of the positron, E_e, measured by the 6m Tagger and the energy of the photon, E_γ, measured by the Spectrometer add up to the energy of the positron beam, E_{eBeam}:

$$E_\gamma + E_e = E_{eBeam}.$$

The position and energy of the electrons that hit the 6m Tagger are correlated because of the magnetic field. The higher energetic electrons hit the 6m Tagger closer to the beam pipe. The same is true, when a positron beam is used. Because of a different orbit of the positron beam, the magnets in front of the 6m Tagger create a slightly different field, which leads to a shift of the energy window of the 6m Tagger to lower energies by about about 1 GeV for positrons compared to electrons. The data that are shown in this section to demonstrate the calibration procedure are from a positron run (run number 62003) from January of 2007.

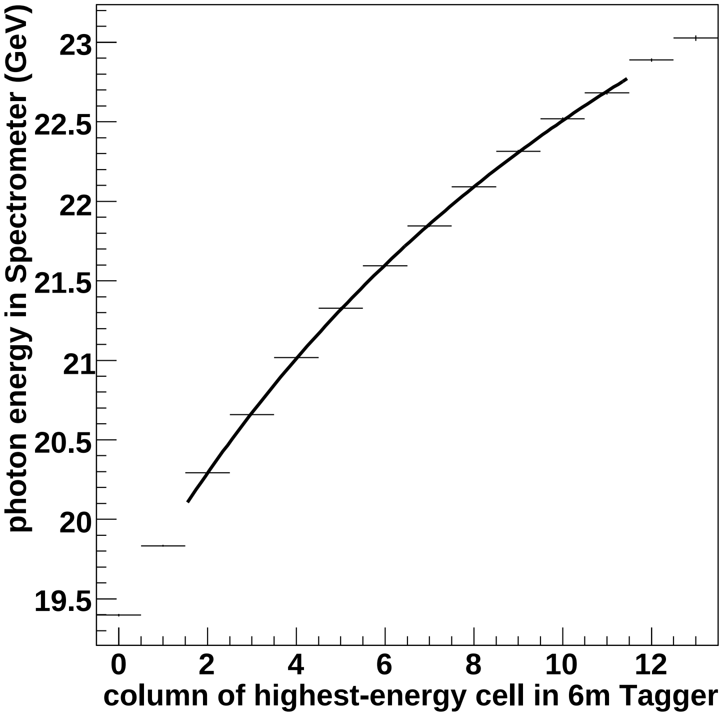

Figure 5.17: Photon energy measured in the Spectrometer vs. position of positron in the 6m Tagger. For every column in the 6m Tagger a Gaussian function was fitted to the distribution of energies in the Spectrometer. This histogram shows the mean values and the associated errors of these fits. The function $E_{photon}(x) = E_{eBeam} - \frac{a^2}{a-bx}$ is fitted to the histogram and shown as a line.

The dependence of the energy on the position was determined by taking the energy of the photon (electron-positron pair) from the Spectrometer and the reconstructed electron position in the 6m Tagger. Here the position reconstruction uses only the column with the highest energy. A function, $E_e(x) = \frac{a^2}{a-bx}$, is fit to the data, where a is the energy and b is the slope at position 0. For every column in the 6m Tagger one histogram was filled with the energies in the Spectrometer. A Gaussian function was fitted to each of these histograms. The mean values and errors of the mean values were taken from these fits and can be seen in Figure 5.17. The selection criteria of the events for the calibration were the following:

- Both local triggers, for 6m Tagger and Spectrometer: At least one has to be fired for the event to be stored by the online software, the other one is part of the coincidence condition.
- Event marked as good by Spectrometer reconstruction (symmetric coincidence): The Spectrometer has to detect both electron and positron from the pair production.
- Energy in 6m Tagger between 3.0 GeV and 15.0 GeV: The lower cut ensures sufficient energy to give a significant position reconstruction. The higher cut removes off-momentum electrons and some pile-up.
- Event should have the cell with the highest energy in the column with the highest energy.
- Highest-energy cell either in center row, or the row just above the center row: The data showed that the overwhelming majority of events were in these rows.
- Cell with the second highest energy in the same or a neighboring column: This removes pile-up events in which the 6m Tagger is hit at different positions.
- Energy in column with the highest energy at least 60% of 5×5-cell energy: This requirement selects events which are centered in the column in the highest-energy column.

With this event sample also the mean energies, Fig. 5.18, in the columns with the highest energy, and the energy fractions, Fig. 5.19, in these columns of the 5×5-cell energy were determined. After the dependence of the energy on x had been determined, the calibration constants were adjusted to match that behavior. Because of the small variation in the vertical position of

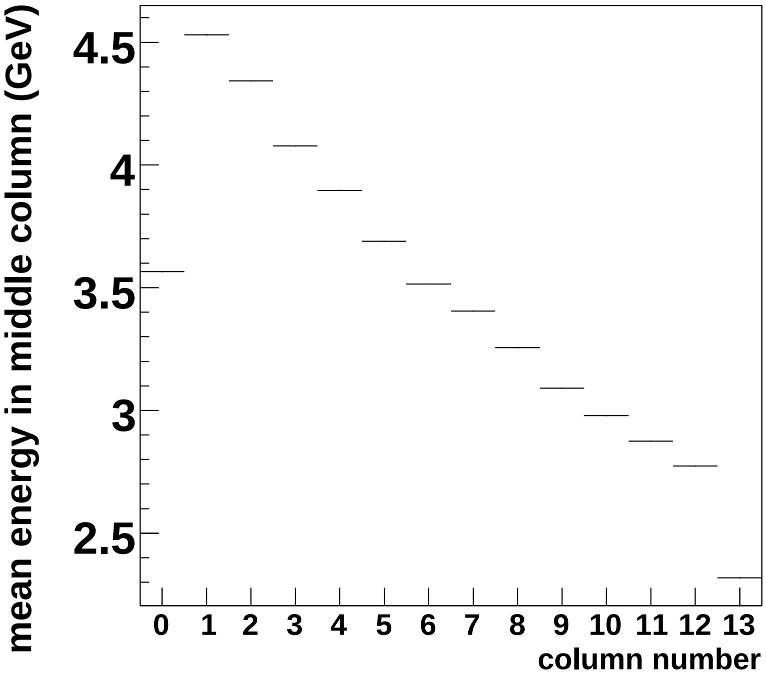

Figure 5.18: Mean energies for the columns that had the highest energy in the 6m Tagger. The event selection is described in the text.

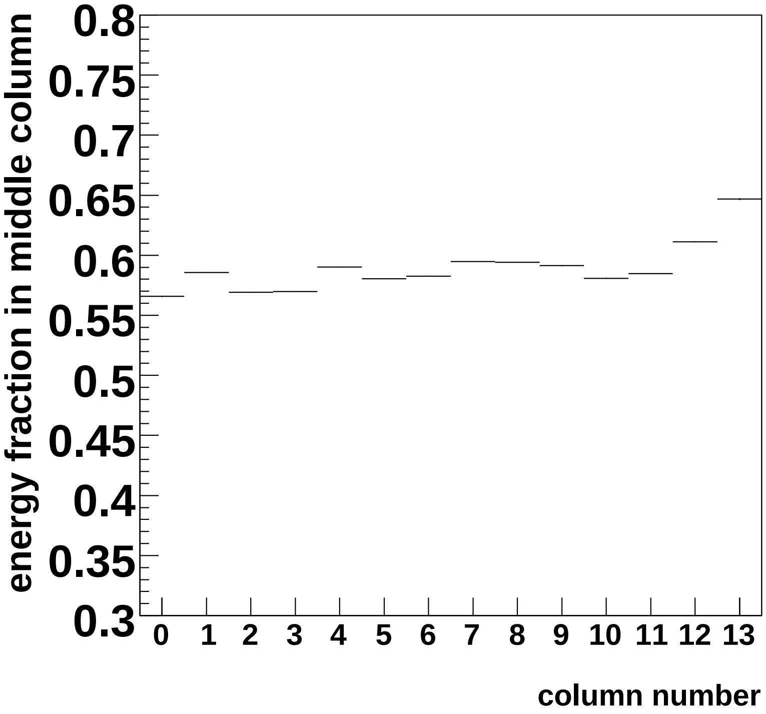

Figure 5.19: Mean energy fraction in the highest-energy column of the 5×5-cell energy. The event selection is described in the text.

the positrons hitting the 6m Tagger, it was not possible to determine the calibration constants separately for each cell, but the calibration procedure changed the calibration constants of all the cells in the same column by the same factor.

One column contains 5 cells. So exactly 5 columns are used for the 5×5 energy reconstruction. The calibration constant of the center column was corrected by the product of the mean energy fraction, f, in the center column and the expected energy, as taken from the energy vs. position fit, divided by the previously reconstructed energy, E_n:

$$c_{n+1} = f \frac{E_{expected}}{E_n} c_n,$$

where c_n and c_{n+1} are the old and new calibration constants, respectively. The calibration was iterated for a few times until the calibration constants changed by less than a percent. The initial calibration was done cell-by-cell with a test beam, as described in [51]. The mean energy fraction of the center column was determined from the events reconstructed with the previous calibration constants and was averaged over all possible center columns, thus excluding the two leftmost and two rightmost columns. This averaging assumes that the width of the shower is independent of the energy and angle of the impacting particle, which is only a rough assumption. For the columns on the edges (the first two and last two) this procedure does not work, because they are never the centers of the 5×5 reconstruction. Therefore their mean contribution to the closest possible center column is used. The leftmost column was calibrated for the mean fraction of energy it should have as being the first column to the left of the center column in events that center in the second column.

Figure 5.20 shows the sum of the positron and photon energies measured by the 6m Tagger and the Spectrometer after the 6m Tagger was calibrated. Between run 50999 from July 2004 and run 62003 from January 2007 the width of the sum distribution has increased, which indicates a degradation of the resolution of the 6m Tagger and/or the Spectrometer. Figure 5.21 shows the difference between the energies of the 5×5 reconstruction and the energy predicted from the position, which is only dependent in the 6m Tagger. That indicates that the degradation of the Spectrometer resolution gives a larger contribution to the increase of the width of the energy sum between these two runs.

This calibration relies on the quality of the calibration of the Spectrometer and the aforementioned assumptions. The described calibration procedure corrects for changes of the energy response of entire columns of five cells. A

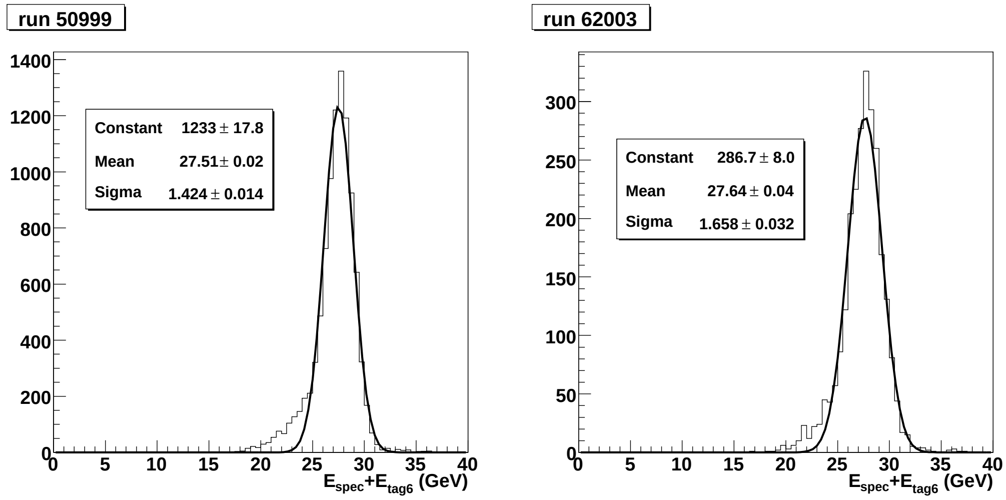

Figure 5.20: Sum of the positron and photon energies measured by the 6m Tagger and the Spectrometer. The peak should be at the energy of the positron beam. The widths show the combined resolutions of 6m Tagger and Spectrometer. The tails to lower energies come partly from mismatched 6m Tagger-Spectrometer coincidences.

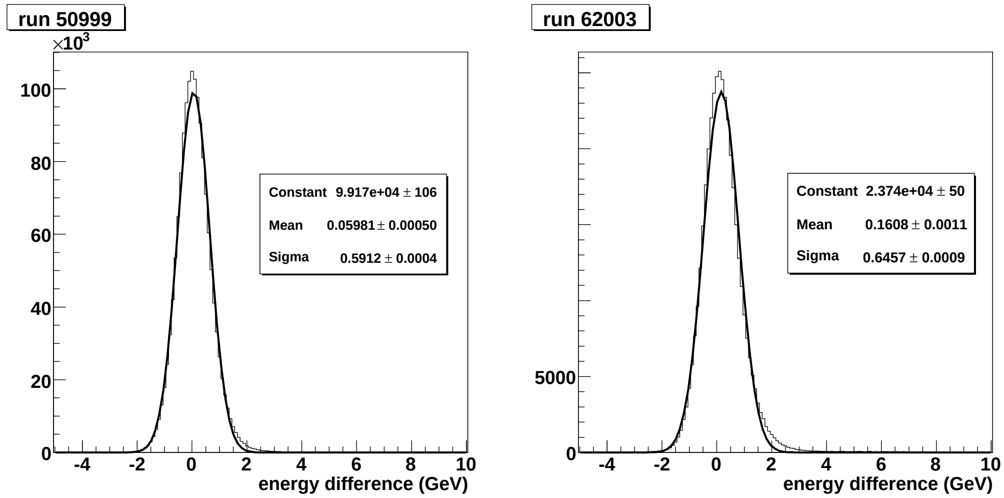

Figure 5.21: Difference of the energies from the 5×5 reconstruction and the energy reconstructed from the position. The widths show the combined resolutions of these methods. The increase in width from July 2004 to January 2007 is much smaller than the one seen in 5.20.

calibration procedure that corrects the calibration constants for each individual cell could lead to a slightly better energy resolution.

The signal from the Photon Calorimeter could not be used for the calibration of the 6m Tagger, because the energy resolution of that component was too poor.

5.6 Photon Acceptance Measurements

One task of the 6m Tagger is the determination and cross check of the acceptances of the photon detectors after the luminosity upgrade. The knowledge of the photon acceptance is essential for the determination of the Luminosity. The acceptance of the photon detectors is affected by the aperture window. On the trajectory of the photon from the interaction point to the exit window are obstacles, such as parts of magnets, that shade some of the outer part of the photon aperture window. The effect of the aperture window depends on the position of the interaction point and the average angle of the photon.

The acceptance of the photon detectors is also affected by the photon conversion probability in the exit window, which is about 10%. Only the electron-positron pairs from the converted photon hit the Spectrometer. The geometry of the electron-positron pairs that are detected by the Spectrometer influences the detection efficiency of that component. Both the electron and the positron have to be clearly detected in the upper and lower part of the detector. So only about 20% of these events are counted by the Spectrometer. This probability is dependent on the energy of the photon, while the effects of the aperture window are largely independent of energy, but affect both photon detectors in the same way.

By tagging Bremsstrahlung events with the 6m Tagger, the acceptance of the photon detectors can be determined. The total number of tagged events is counted. The fraction of events that are in coincidence with the respective photon detector (PCAL or SPEC), is the acceptance. The 6m Tagger can only tag events in a certain energy range, in which it has an acceptance of almost 100%. There are some corrections that can be applied to the simple calculation of the acceptance. There will be some background in the 6m Tagger that does not come from Bremsstrahlung events. The contribution of photoproduction is assumed to be negligible. There are also some events with high energies in the 6m Tagger, close to the electron beam energy of 27.5 GeV, which might be due to off-momentum electrons. The observation of these events with a compatible rate in electron only bunches supports this assumption. These events can be cut out without much difficulty because of their high energy outside the regular acceptance for electrons in the 6m Tagger. Other effects appear with higher luminosities and thus rates. In pile-up signals several bremsstrahlung interactions contribute to the same event. At high luminosity, about 1% of the events leave a signal in the 6m Tagger. So also 1% of the detected events have a signal from 2 electrons. The relatively small acceptance of the Spectrometer, which was intended, makes it less affected by pile-up effects. Another issue is the detection of false coincidences. At high rates the Photon Calorimeter detects a photon in almost every bunch crossing. So, when an electron is tagged in the 6m Tagger, it can happen that a photon detected in the same event by the Photon Calorimeter does not come from the same Bremsstrahlung event.

5.6.1 Acceptance of the Photon Calorimeter

As a check of the predicted aperture window for the photons, an aperture scan run with different beam tilts was conducted to measure the photon acceptances and compare them to predictions. This was the ZEUS electron-proton run 52980 in January 2005.
For the calculation of the acceptance, a clean sample of detected positrons in the 6m Tagger was selected. For the selection of coincidences with the Photon Calorimeter (PCAL), the requirement on the PCAL is just a threshold on the sum of the ADC-signals from the two photomultipliers. The prediction of the acceptance took into account the calibration, the aperture window, and other minor effects. The measured acceptance values were determined by dividing the number of coincidence events with the total number of clean 6m Tagger events. A correction for random coincidences was also applied, whereby the average number of photon per bunch crossing was taken into account. The measurement of the PCAL photon acceptance vs. time can be seen in Fig. 5.23. During the run the beam tilt was changed, so different time periods were associated with different beam tilts, as seen in Fig.5.22. Figure 5.24 summarizes the tilt scan measurements. For 8 periods of stable beam position the average photon beam positions and the acceptances are shown. The coordinates of the photon beam are given in the plane that is transverse to the line between the interaction point and the photon detectors about 100 m away. In general, the photon acceptance is lower close to the edges of the aperture window. The measured acceptances were slightly lower in the upper region and slightly higher at the two lower points. That might indicate a small vertical shift of the actual aperture window to the predicted one.

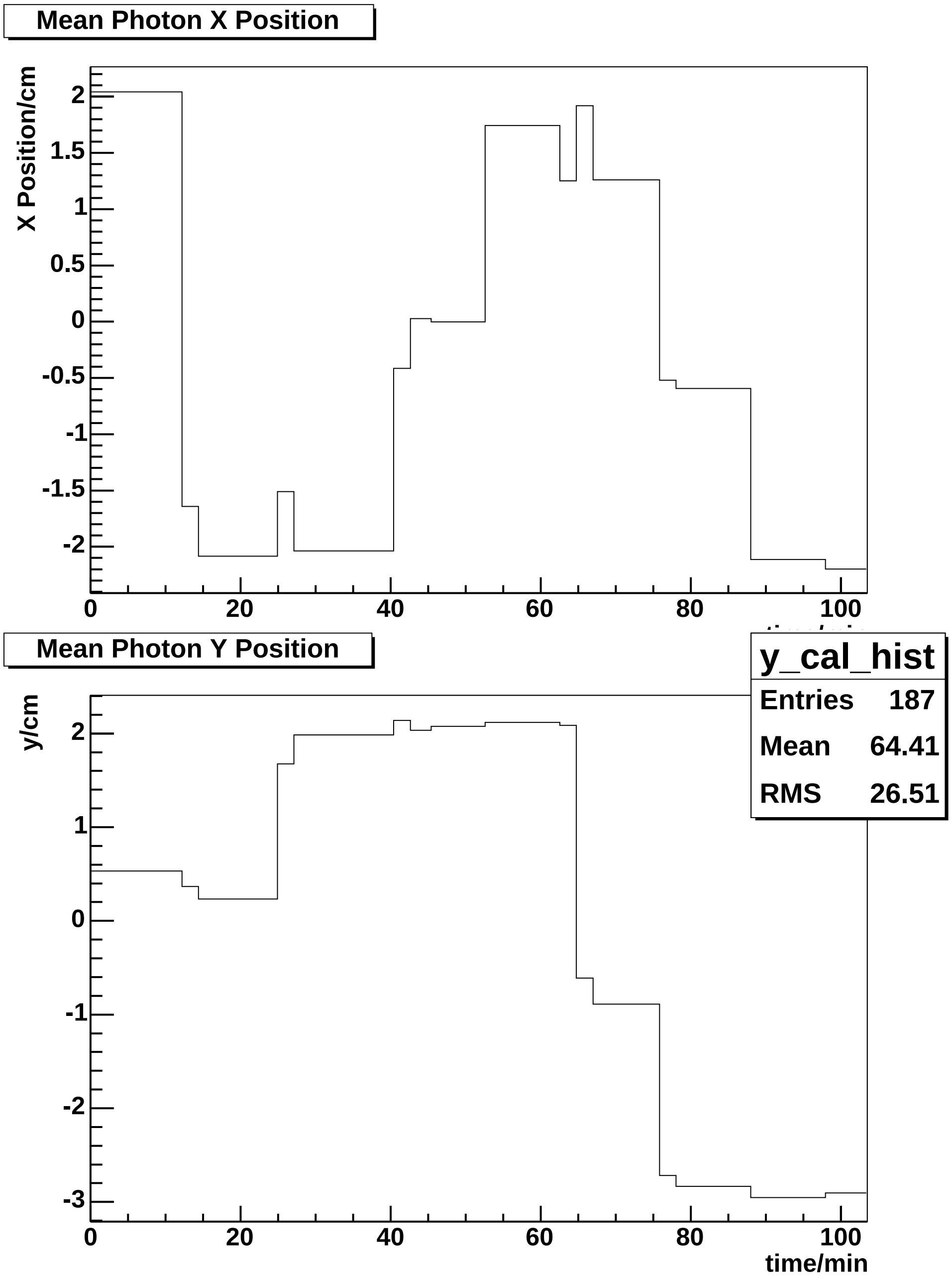

Figure 5.22: Photon beam position measured by the PCAL averaged over intervals of about a minute. These values were used for the prediction of the geometrical acceptance.

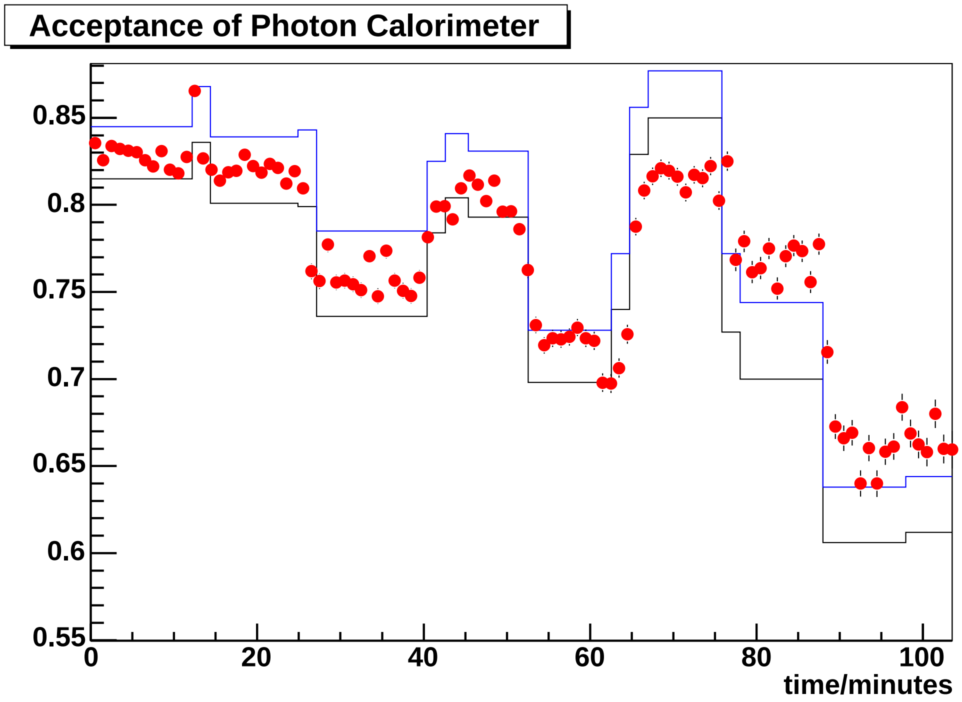

Figure 5.23: Acceptance of the Photon Calorimeter. The dots are the measurement with the 6m Tagger. The vertical bars show the statistical errors. The lines are the predictions. The upper line assumes a smaller and the lower line a larger beam spread. The variation of the data points comes not only from statistical fluctuations but also from changes in the beam steering, while the predictions are kept constant over certain periods with parameters averaged over these periods. The positions of the beam during this run can be found in Fig. 5.22.

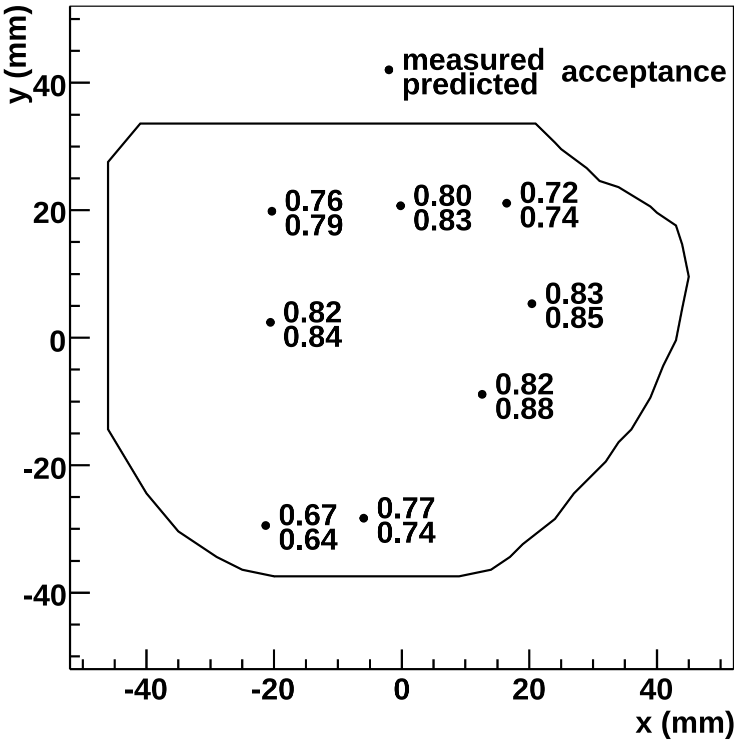

Figure 5.24: Photon beam positions and acceptances during the acceptance scan, run 52890.

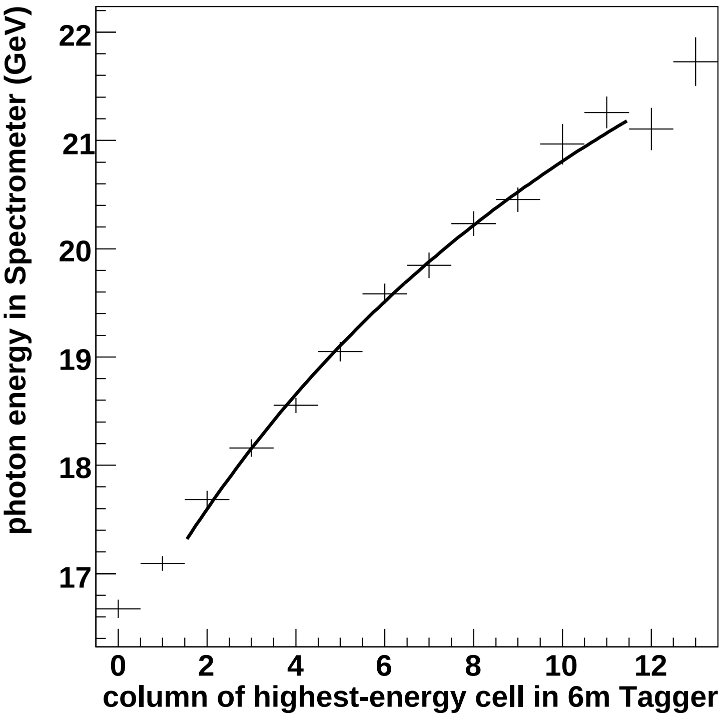

Figure 5.25: Photon energy measured in Spectrometer vs. position of electron in the 6m Tagger. This data is from the electron run 53394 from the beginning of 2005. The different energy window can be seen as compared to the positron run in Fig. 5.17

5.6.2 Acceptance of the Spectrometer

The photon acceptance of the Spectrometer is dependent on the photon energy because of the geometry of the electron-positron pair that has to be detected by the Spectrometer. A measurement of the Spectrometer acceptance as a function of the photon energy can be seen in Fig. 5.26. The data were taken during the ZEUS electron-proton run 53394 with nominal beam tilt. The photon energy was determined from the fit of the photon energies to the position of the electron in the 6m Tagger, see Fig. 5.25. The position resolution was assumed to be better than half a cell width. Translated into energies this means an energy resolution of about 0.2 GeV. The measurement was statistically limited and compatible with the prediction.

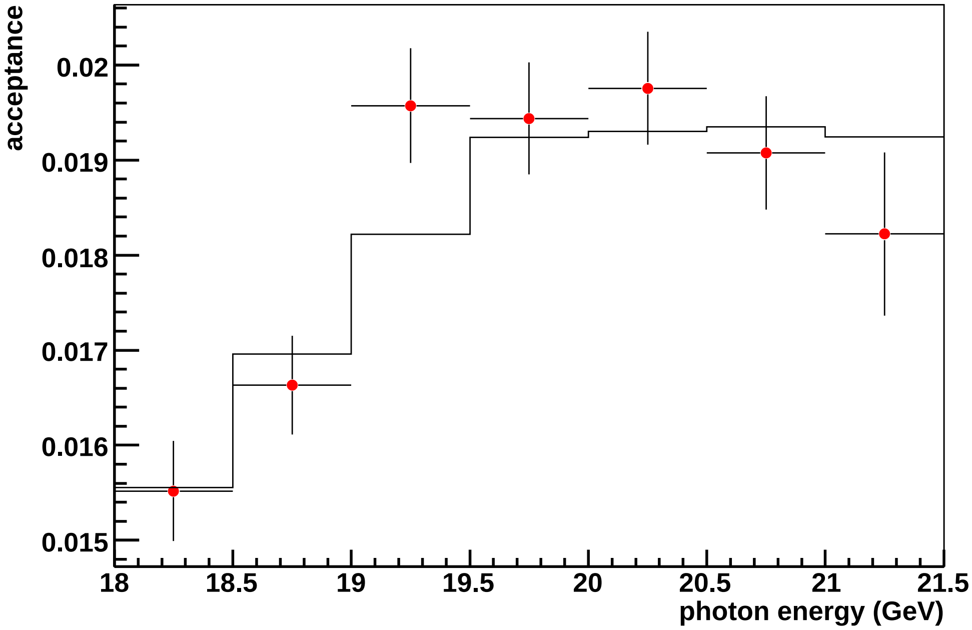

Figure 5.26: Acceptance of the Spectrometer as a function of the photon energy. The dots with the error bars are the measurement. The line is the prediction. The vertical error bars show the statistical uncertainty.

5.7 6m Tagger and Photoproduction

Photoproduction events at HERA are *ep* events with low Q^2, $Q^2 < 1\,\mathrm{GeV}^2$. The electron radiates a quasi-real photon that subsequently interacts with the proton. The electron cannot be detected inside the ZEUS detector, because it escapes through the beam pipe. But if it is in a certain energy range, it will be diverted into the 6m Tagger, where it can be detected. The kinematic quantities in photoproduction events have to be normally calculated from the detected hadronic final state. The detection of the scattered electron improves the knowledge of the kinematic quantities.

Chapter 6

Event Reconstruction

This chapter describes how the variables that were used in this analysis were calculated from the output of the detector components of ZEUS. The event reconstruction is done in the same way for the data taken with the detector and events simulated at the detector level of the Monte Carlo.

6.1 Detector Input for the Reconstruction

6.1.1 Calorimeter Cells

The most important component used in this analysis is the Uranium Calorimeter (CAL), described in chapter 4.3.2. To be used for the reconstruction of the event, the energy of an electromagnetic calorimeter cell was required to have an energy of more than 60 MeV. Cells of the hadronic part of the calorimeter were required to have more than 110 MeV. Also noisy cells were removed. A cell was considered noisy if

- the cell was in the list of noisy cells for that running period.
- the imbalance between the two photomultipliers of the cell was too large while the total energy in the cell was below 1.0 GeV:

$$|E_{PMT,1} - E_{PMT,2}| > (0.49(E_{PMT,1} + E_{PMT,2}) + 0.03\,\mathrm{GeV})$$

- the cell was isolated and had low energy: $E_{cell} < 80\,\mathrm{MeV}$ for EMC cells and $E_{cell} < 110\,\mathrm{MeV}$ for HAC cells.

For the data, as opposed to the Monte Carlo, energy scale correction factors were applied to the remaining cells. These factors were extracted by an analysis [61] of pure single-jet events in DIS that used the energy balance between scattered electron and the jet to calibrate the energy scale of the calorimeter.

6.1.2 Tracks

Tracks are reconstructed using the CTD, described in chapter 4.3.1. The tracks constrain the reconstructed vertex of the interaction and contribute to the energy flow objects, which are described in the next section.

6.1.3 Energy Flow Objects

To get the most precise information about the energy and direction of the particles, the data from the calorimeter cells and the CTD tracks are combined in energy flow objects (ZUFOs, ZEUS Unified Flow Objects). When tracks and calorimeter cells can be matched, the energy measurement of the component with the better resolution is used. Typically this is the CTD for lower and the calorimeter for higher energies. This procedure is described in more detail in [62]. In this analysis the ZUFOs are only used to reconstruct the jets. Cells and tracks associated with the scattered electron are removed.

6.2 Electron Finding

The signature of a neutral current DIS event is a scattered electron. The scattered electron is identified by an electromagnetic energy deposit in the calorimeter. In this analysis, the program Sinistra [63, 64] was used to find the electron. This program uses a neural network to determine the probability that an an energy cluster in the CAL originates from an electron. The energy of the electron is calculated from the sum of energy depositions that are associated with the cluster. The impact position of the electron in the calorimeter is calculated from the energy weighted average of the calorimeter cell positions. The position is then corrected by using data from the HES and the SRTD [65, 66]. Using the corrected position, the energy of the electron is then corrected for dead material and non-uniformities in the calorimeter response. The energy of electrons in the barrel and rear regions of the calorimeter are also corrected with information from the Presampler.

6.3 Jet Finding

Jets were reconstructed in the hadronic center of mass (HCM) frame from ZUFOs using the longitudinally-invariant k_T-clustering algorithm [35, 36]. In the HCM-frame the proton and photon collide with equal and opposite momenta. The photon momentum was reconstructed from the four-momentum difference between incoming and scattered electron. The transformation into the HCM-frame was done in such way that the proton momentum points into the positive z-direction. The k_T-clustering algorithm clusters the energy depositions according to their distance in the transverse energy plane. To get the jet variables in the laboratory frame the jets were boosted back.

6.3.1 K_T-Clustering Algorithm

The k_T-clustering algorithm was chosen for theoretical reasons, described in chapter 2.5. It takes as input a list of the particles' four-momenta. The four-momenta are combined in an iterative procedure until the four-momenta of the jets remain. In this analysis the input particles and the jets were defined to be massless. When particles were combined, the transverse energies were added and the angles averaged weighted in transverse energy (Snowmass scheme [67]), given by

$$E_T^{\text{jet}} = \sum E_{T,i}, \;\; \phi^{\text{jet}} = \frac{\sum E_{T,i}\phi i}{\sum E_{T,i}}, \;\; \eta^{\text{jet}} = \frac{\sum E_{T,i}\eta i}{\sum E_{T,i}}.$$

The k_T algorithm works in the following steps:

1. The distance between two particles i and j in transverse energy is defined as
$$d_{ij} = min\{E_{T,i}, E_{T,j}\}^2[(\Delta\eta_{ij})^2 + (\Delta\phi_{ij})^2]$$

2. To every particle i also a transverse energy relative to the beam axis is assigned:
$$d_i = E_{T,i}^2 \cdot R_0^2$$
R_0 is a parameter that controls the radius of the reconstructed jets. It is normally set to 1, as it was in this analysis.

3. The smallest distance d_{ij} or d_i is determined. If it is a distance d_{ij} between two particles, the two particles i and j are combined in the above mentioned scheme. If it is a d_i, the particle i is removed from the input list and put into the list of possible jets. The procedure is repeated until no particles can be combined anymore. All input particles end up in jets, thus the name inclusive.

6.3.2 Jet Energy Correction

The energies of the detector level jets are on average lower than the ones reconstructed from the hadrons. This is mainly due to dead material in the detector. To correct for that, the detector- and hadron level jets of the Monte Carlo were compared. The events were selected as described in chapter 7, but the requirement on the minimum jet-E_T was lowered to 3 GeV. The jets at detector- and hadron level were matched with a requirement of $\Delta R = \sqrt{(\Delta\eta_{ij})^2 + (\Delta\phi_{ij})^2} < 1$. In 17 different $\eta_{\mathrm{LAB}}^{\mathrm{jet}}$-bins the transverse energies of jets on the detector level were plotted against the hadron level energies. This was done in the laboratory frame to avoid a bias from the reconstruction of the boost into the HCM-frame. Quadratic functions were fitted to these data and yielded correction factors that were applied to the energies of the measured jets. Figures 6.1 and 6.2 illustrate the effect of the jet energy correction. After the jet energy correction the jets were ordered according to their transverse energy in the HCM-frame.

6.4 Reconstruction of Kinematic Quantities

To reconstruct Q^2, x_{Bj} and y, the scattered electron is used, the index el stands for the electron method:

$$Q^2_{el} = 2E_eE'\,(1 + cos\theta)$$

$$y_{el} = 1 - \frac{E'}{2E_e}(1 - cos\theta)$$

$$x_{el} = \frac{Q^2_{el}}{s\,y_{el}}$$

E_e is the energy of the incoming electron. E' and θ are the energy and angle with respect to the beam axis of the scattered electron. The direction of the scattered electron is computed from the position where it enters the calorimeter, taking into account the reconstructed vertex. Because of momentum and energy conservation, the exchanged photon can be reconstructed from the difference between incoming and scattered electron. Initial state (ISR) and final state radiation (FSR) cannot be taken into account by this method, but they are corrected for statistically by the later applied detector-to-hadron level correction.

For one of the cuts in this analysis, y was also reconstructed with the Jacquet-Blondel method. Here only the hadronic energy distribution but not the scattered electron is used:

$$y_{jb} = \frac{1}{2E_e}(E_h - p_{z,h})$$

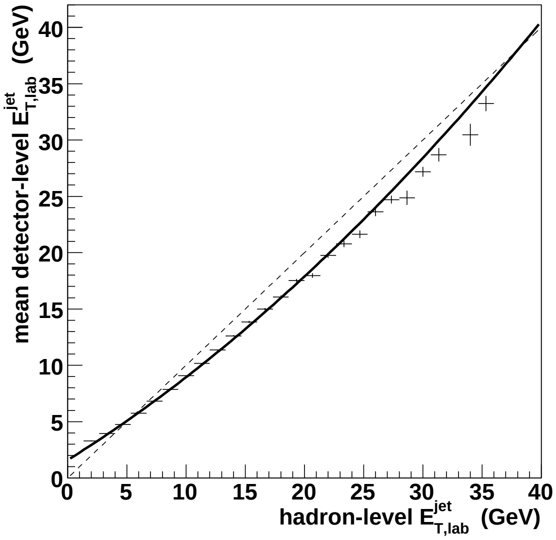

Figure 6.1: Detector level vs. hadron level $E_{T,\mathrm{LAB}}^{\mathrm{jet}}$ before jet energy corrections were applied for $0.2 \leq \eta_{\mathrm{LAB}}^{\mathrm{jet}} < 0.4$: The thick line shows the quadratic fit, the thin dashed line shows where the points would lie for perfectly matching energies on both levels.

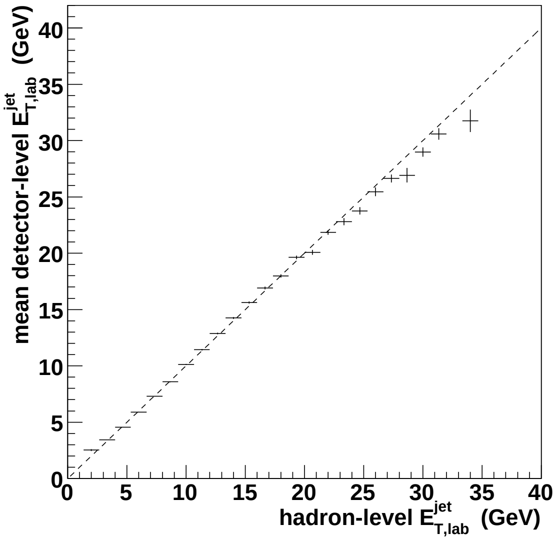

Figure 6.2: Detector level vs. hadron level $E_{T,\mathrm{LAB}}^{\mathrm{jet}}$ after jet energy corrections were applied for $0.2 \leq \eta_{\mathrm{LAB}}^{\mathrm{jet}} < 0.4$:

E_h and $p_{z,h}$ are the total hadronic energy in the calorimeter and the z-component of the total hadronic momentum, respectively.

Chapter 7

Event Selection

This chapter describes the detector level event selection for data and Monte Carlo events. The event sample used in this analysis was taken in the years from 1998 to 2000 and had an integrated luminosity of $82\,\mathrm{pb}^{-1}$.

7.1 Trigger Selection

7.1.1 Introduction

Events have to meet certain conditions on all the trigger stages to be finally written to tape and be available for analysis, as described in chapter 4.3.5. To consistently compare selected data and Monte Carlo events, both must go through the same trigger chain. The trigger chain consists of requirements on the FLT (first level trigger), SLT (second level trigger) and TLT (third level trigger). For the data taking several so-called trigger slots were defined on each trigger level. Each of these slots describes one condition that causes the event to pass that trigger level. The TLT and SLT slots require certain slots of the lower levels (SLT and FLT) to be fired. Depending on the particular analysis a subset of these trigger slots is used. Additional, stricter cuts were applied in this analysis to take changes in the trigger configuration into account. The trigger requirements that were applied in this analysis are described below.

7.1.2 FLT

The following first level trigger slots were used:

- FLT 40: electromagnetic energy in the calorimeter above 15 GeV
- FLT 41: total transverse energy in the calorimeter above 21 GeV

- FLT 42: a good track and one of the following conditions:
  - total energy in calorimeter greater than 15 GeV
  - total electromagnetic energy in the calorimeter greater than 10 GeV
  - total electromagnetic energy in the BCAL greater than 3.4 GeV
  - total electromagnetic energy in the RCAL greater than 2.0 GeV
- FLT 43: total transverse energy in the calorimeter greater than 11.5 GeV
- FLT 44: (a track found and the electromagnetic energy in the BCAL greater than 4.8 GeV) or (the electromagnetic energy in the RCAL greater than 3.4 GeV)
- FLT 46: isolated electromagnetic energy deposit and one of the following conditions:
  - total electromagnetic energy in the RCAL greater than 2.0 GeV
  - SRTD signal and a good track
  - good track and total energy in calorimeter greater than 18 GeV

FLT 40,41,43,44 or 46 was required for the DIS trigger slots. FLT 40,41,42 or 43 was required for the TLT slot HPP14.

7.1.3 SLT

Two different second level trigger slots were used:

- DIS06 requires $E - p_z + 2 \cdot E_\gamma > 29\,\text{GeV}$ (E_γ is the energy measured by the Photon Calorimeter, part of the luminosity detector, described in chapter 4.3.4) and one of the following:
  - electromagnetic energy in RCAL greater than 2.5 GeV
  - electromagnetic energy in BCAL greater than 2.5 GeV
  - electromagnetic energy in FCAL greater than 10 GeV
  - hadronic energy in FCAL greater than 10 GeV
- HPP01 requires all of the following:
  - if a vertex is reconstructed, then $|z_{\text{vertex}}| < 60\,\text{cm}$ is required
  - at least one vertex track
  - transverse energy (excluding the innermost FCAL ring) greater than 8 GeV.
  - $E - p_z > 8\,\text{GeV}$ or $p_z/E > 0.95$

7.1.4 TLT

One of the following TLT slots was required in event selection of this analysis:

- HPP14: A dijet photoproduction trigger. It requires two jets in the laboratory frame with transverse energies of at least 4.5 GeV and pseudorapidities of less than 2.5. At the beginning of the running period of the analyzed data, this energy threshold was 4.0 GeV. For consistency, two jets with a transverse energy of at least 5.0 GeV in the laboratory frame were required in this analysis in combination with this trigger slot. As this is a photoproduction trigger, no scattered electron is required to be found. Also the energy depositions of the scattered electron are not excluded from the jet reconstruction and this trigger may count them as a jet.
- DIS01: An inclusive DIS trigger. An electron with at least 4 GeV outside a rectangle of $24 \times 12\,\mathrm{cm}^2$ around the beam pipe is required. This trigger was prescaled during the analyzed data taking period. The effective luminosity for this trigger was $11.4\,\mathrm{pb}^{-1}$
- DIS03: An inclusive high-Q^2 DIS trigger. An electron with at least 4 GeV outside a circle with a radius of 35 cm around the beam pipe is required for this slot. In this analysis, the reconstructed electron was required to be outside a radius of 36 cm.

Figure 7.1 illustrates the efficiency of the TLT slots with the requirements as described above as a function of Q^2 determined with the ARIADNE Monte Carlo sample. The efficiency was calculated as the ratio of events that passed the trigger conditions over the events that fulfilled that kinematic and jet selection on hadron level.

7.2 Background Removal Cuts

To remove background and events that are likely to be badly reconstructed, several cleaning cuts were applied.

To make sure the electron hit the calorimeter in a region where it could be well constructed,

$$|x_e| > 13\,\mathrm{cm} \text{ or } |y_e| > 7\,\mathrm{cm}$$

was required for the reconstructed position of the electron. The hadronic energy in a cone around the scattered electron was required to be less than 10% of the reconstructed electron energy:

$$E_{had,cone}/E_e < 0.1$$

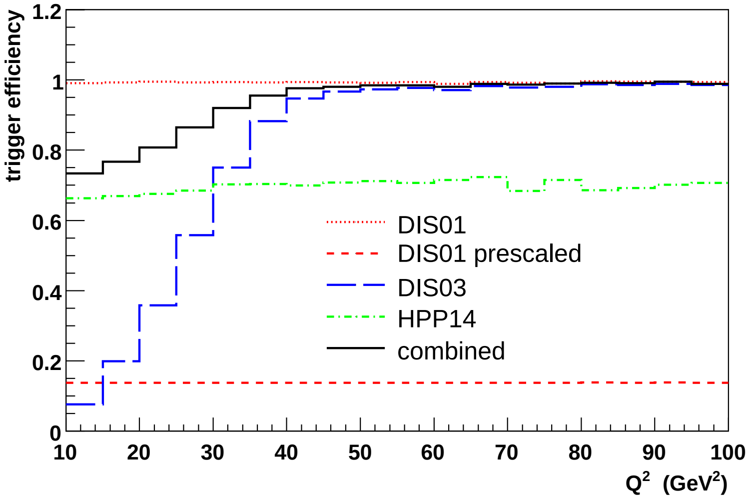

Figure 7.1: Trigger efficiencies as determined with the ARIADNE sample for the TLT slots HPP14, DIS01 and DIS03 with their associated trigger chain as described in the text. The solid line shows the combined trigger efficiency.

To avoid electrons with a too high reconstructed energy at low angles,

$$(E_e - p_{z,e}) < 54\,\mathrm{GeV}$$

was required. The cut

$$40\,\mathrm{GeV} < E - p_z < 60\,\mathrm{GeV}$$

removes beam gas events and events that suffer from cosmic background. The $E - p_z$ in events from electron-proton collisions at HERA is $2E_e = 55\,\mathrm{GeV}$. The $E - p_z$ of the initial proton is zero, because it points into the positive z-direction. If only the part of the proton remnant that goes straight down the beam pipe remains undetected, the measured $E - p_z$ of the event is still expected to be 55 GeV.

In the following cut p_T is the absolute value of the vectorial sum of energy depositions in the calorimeter perpendicular to the beam axis. A large value of p_T indicates that either highly energetic particles from the interaction left the detector undetected or particles not coming from the interaction point deposited energy in the calorimeter. E_T is just the absolute sum of transverse energies.

$$p_T/\sqrt{E_T} < 3\sqrt{\mathrm{GeV}}$$

cuts out mainly cosmic background.

The nominal position of the interaction lies at $z_{\text{vertex}} = 0\,\text{cm}$. So

$$-50\,\text{cm} < z_{\text{vertex}} < 50\,\text{cm}$$

cuts out mainly interactions from the beam with residual gas.

7.3 Kinematic Selection

The kinematic quantities in this analysis were calculated from the energy and angle of the scattered electron. The four-momentum of the exchanged virtual photon was assumed to be the difference of the four-momenta of the incoming electron and the scattered electron. The DIS regime is defined by a virtuality of the photon, Q^2, greater than $1\,\text{GeV}^2$. The analyzed kinematic phase space in this analysis is

$$10\,\text{GeV}^2 < Q^2 < 100\,\text{GeV}^2$$

and

$$10^{-4} < x_{\text{Bj}} < 10^{-2}.$$

The inelasticity of the photon was required to be

$$y_{el} < 0.6\,\text{GeV}$$

and

$$y_{jb} > 0.1\,\text{GeV}.$$

The indices *el* and *jb* indicate if the electron- or the Jacquet-Blondel-method were used to reconstruct y. The upper cut also implies a minimum energy of the electron of 11 GeV.

7.4 Jet Selection

The jets were reconstructed in the hadronic center of mass frame. To check jet quantities in the laboratory frame, their four-vectors were boosted back. The pseudorapidity of the jets was required to be $-1 < \eta^{\text{jet}}_{\text{LAB}} < 2.5$ so that they are in the region of the best acceptance of the calorimeter. As described in the previous chapter, the jet energy was corrected for dead material effects. All jets were required to have $E^{\text{jet,uncorr}}_{T,\text{HCM}} > 3\,\text{GeV}$ and $E^{\text{jet,uncorr}}_{T,\text{lab}} > 4\,\text{GeV}$ before the correction. The following cuts were applied on the corrected energies of the jets:

$$E^{\text{jet1}}_{T,\text{HCM}} > 7\,\text{GeV}$$

$$E_{T,\mathrm{HCM}}^{\mathrm{jet2,3}} > 5\,\mathrm{GeV}$$

For the dijet sample at least two jets were required. The trijet sample was a subsample of the dijet sample with the additional requirement on the third jet. The reason for the asymmetric jet energy cut is given in chapter 2.5.

Chapter 8

Cross Section Measurements

8.1 Cross Section Definition

The hadron-level cross section, σ_{hadron}, is defined as

$$\sigma_{hadron} = C_{corr} C_{\mathrm{QED}} \frac{\sum_{i=1}^{N_{events}} w_i}{\mathcal{L}_{int}},$$

where N_{events} is the number of events in the sample that passed the cuts. The w_i are the weights of the events, described in section 8.3. $\mathcal{L}_{int}$ is the integrated luminosity of the analyzed data sample. C_{corr} is the detector to hadron level correction, also called acceptance correction. C_{QED} corrects the data to Born level QED.

Differential cross sections are functions of one or more variables. This dependence is continuous, but for practical reasons they are measured in bins of the variables. The bins are chosen in a way such that the migration between bins on hadron and detector level is not too large and that each bin has enough events. The migration is mainly determined by the resolution of the measured variable. The width of the bins should be at least twice the resolution. The differential cross section in a bin i is then calculated as the cross section of the events that fall into bin i, divided by the width of the bin i:

$$\frac{\Delta\sigma}{\Delta X}(X_i) = \frac{\sigma_i}{\mathrm{width}_i}$$

X is the variable in which the differential cross section is measured. X_i is a value of X in bin i. For the plots it was chosen to use the center of the bin for X_i.

8.2 Hadron Level

Theoretical predictions and data were compared at the hadron level. The acceptance correction converts this into a detector independent hadron level cross section. The perturbative QCD calculation calculates parton level cross sections. The hadronization process is non-perturbative, so the Monte Carlo predictions are used to correct the parton level cross sections to hadron level. The selection at hadron and parton level was the same as at detector level without detector-specific cuts:

$$10\,\mathrm{GeV}^2 < Q^2 < 100\,\mathrm{GeV}^2, 10^{-4} < x_{\mathrm{Bj}} < 10^{-2}, 0.1 < y < 0.6$$

The kinematics at the hadron and parton levels were calculated from the momentum of the boson that was exchanged in the hard process. The jets were reconstructed with the k_T-algorithm in the HCM-frame from the final hadrons or the partons after the parton cascade before the fragmentation for the Monte Carlo events, from the resulting partons for the NLO calculation. The jet requirements were also the same at all levels:

$$E_{T,\mathrm{HCM}}^{\mathrm{jet1}} > 7\,\mathrm{GeV}, E_{T,\mathrm{HCM}}^{\mathrm{jet2,3}} > 5\,\mathrm{GeV}$$

Like the detector level sample, the dijet sample is inclusive, e.g. with no restrictions on any further jets, and the trijet sample is a subset of the dijet sample with a third jet above 5 GeV in transverse energy.

8.3 Reweighting

The events in the cross section formula above were given weights:

$$N_{weighted} = \sum_{i=1}^{N_{events}} w_i$$

For the data events these weights were in general 1. Only the events exclusively triggered by TLT DIS01 were given a higher weight to account for the prescaling, see chapter 7.1.4. The Monte Carlo events were reweighted depending on Q^2, as described in [29].

8.4 Comparison to Monte Carlo

The data were compared to the ARIADNE and LEPTO Monte Carlo models, see chapter 3. The ARIADNE sample had a simulated integrated luminosity

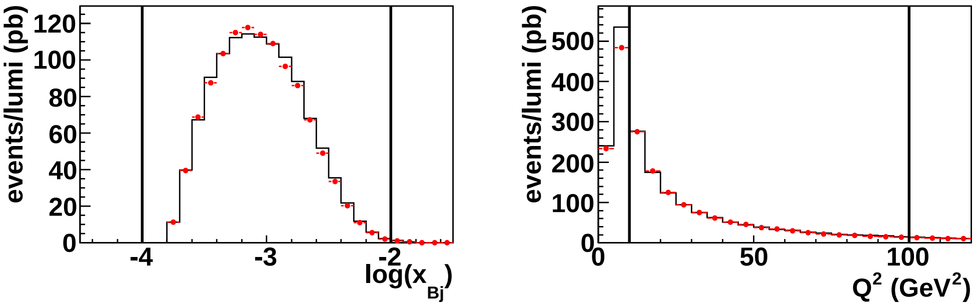

Figure 8.1: Events per luminosity in bins of x_{Bj} and Q^2, data (dots) vs. ARIADNE (lines) at detector level. The number of MC events has been normalized to the number of data events. Further comparison plots can found in Appendix A.

of $56\,\mathrm{pb}^{-1}$ and an observed Q^2 greater than $2.0\,\mathrm{GeV}^2$. The observed Q^2 is the Q^2 calculated from the initial and final electrons. They could be affected by initial or final state radiation, so that the observed Q^2 does not exactly equal the Q^2 of the boson that is exchanged in the hard process. The LEPTO sample consisted of 2 subsamples with the observed Q^2 greater than $3.0\,\mathrm{GeV}^2$ of $23\,\mathrm{pb}^{-1}$ and greater than $10.0\,\mathrm{GeV}^2$ of $94\,\mathrm{pb}^{-1}$. The LEPTO samples were combined and the events weighted according to the luminosity. The Monte Carlo samples were put through the simulation of the ZEUS detector. Monte Carlo and data were compared at the detector level. The Monte Carlo distributions were normalized to match the number of events of the data. In Figure 8.1 the x_{Bj}- and Q^2-distributions of data and ARIADNE are compared, more comparison plots can be found in Appendix A.

8.5 Resolutions

Variables determined by using detector quantities suffer from various detector-dependent effects. For the Monte Carlo events, the original values at the hadron level are available. The resolution of a measured variable can be determined by looking at the difference of the value at the detector level and at the hadron level. The average deviation and the resolution are calculated from the mean and the width of the distribution of this difference. Depending on the variable, the absolute, $x_{detector} - x_{true}$, or the relative difference, $(x_{detector} - x_{true})/x_{true}$, is more adequate to use. The resolution of the variable Q^2 is shown in Figure 8.2.

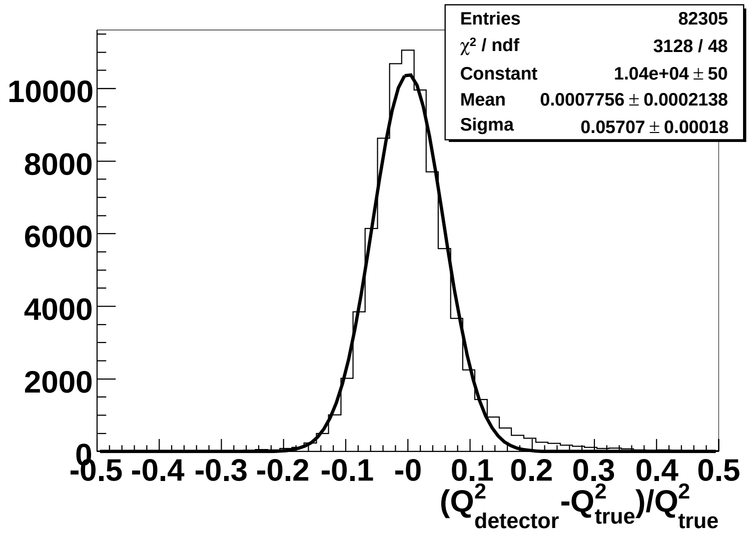

Figure 8.2: Resolution of the variable Q^2 calculated with the electron method.

8.6 Acceptance Correction

The measured cross sections were corrected for detector effects. Therefore the same cuts were applied to the Monte Carlo at the detector level as to the data. At the hadron level only the kinematic and jet requirements were applied. The data were corrected in each bin with the ratio of the number of hadron level events to the number of detector level events.

$$C_{corr} = \frac{N_{weighted,hadron}}{N_{weighted,detector}}$$

To check how well the detector quantities reproduce the hadron level, efficiencies, $\mathcal{E}$, and purities, $\mathcal{P}$, can be calculated:

$$\mathcal{E} = \frac{N_{weighted,detector \wedge hadron}}{N_{weighted,hadron}}, \mathcal{P} = \frac{N_{weighted,detector \wedge hadron}}{N_{weighted,detector}}$$

The efficiencies and purities are calculated in each bin. To fulfill $(detector \wedge hadron)$ an event has to pass the cuts at both the detector and hadron levels and the values of the considered variable have to fall in into the same bin. The purity measures the fraction of detected events that are in that same bin at hadron level. The efficiency measures the fraction of hadron level events that are detected in the same bin at detector level.

8.7 QED Corrections

The NLO QCD calculation only contains QED at $\mathcal{O}(\alpha_{em})$. Both Monte Carlo samples were generated including higher order QED effects. Two large additional LEPTO samples without detector simulation were created, one with and one without higher order QED effects. The ratio of the hadron level cross sections between these samples was used to correct the data.

$$C_{\text{QED}} = \frac{\sigma_{noQED}}{\sigma_{\text{QED}}}$$

So both data and theoretical calculation were compared at Born level in QED.

8.8 Statistical Error

The statistical errors originate from counting a limited number of events. The number of events were assumed to be distributed according to Poisson statistics. Thus the square root of the number of events was taken as the error. More generally, when the events were given different weights, the error was calculated from the square root of the sum of the squares of the weights:

$$N_{weighted} = \sum_{i}^{N_{events}} w_i, \delta N_{weighted} = \sqrt{\sum_i w_i^2}$$

Statistical errors were calculated for data as well as Monte Carlo events. When ratios of correlated event samples were calculated, e.g. the correction factors, the correlation was taken into account. These errors were propagated to the final cross sections as statistical errors. The statistical error of the presented cross sections contains also the statistical errors of all corrections.

8.9 Systematic Uncertainties

To check the stability of the cross section measurement, cuts on detector level were varied by their resolutions. With unlimited statistics and a perfect detector simulation, the correction factors would compensate the varying event counts. The following systematic variations were checked:

- Q^2 was varied by its resolution.
- The cut on y_{el} was varied.

- The cut on y_{jb} was varied.
- x_{Bj} was varied by its resolution.
- The upper and lower cuts on $E - p_z$ were varied separately.
- The cuts on the transverse energy of the jets was varied separately.
- The cut on Z_{vertex} was tightened and loosened.
- LEPTO was used for the hadron to detector level correction instead of ARIADNE.

For each of these variations the cross section was calculated. The detector level requirements for the Monte Carlo were also changed in the same way to get a set of correction factors for each variation. The differences to the presented cross sections were added in quadrature, separately for positive and negative differences.

$$\delta_{syst\pm} = \sqrt{\sum_i (\sigma_{syst,i} - \sigma)^2}, \text{for } \sigma_{syst,i} \gtrless \sigma$$

The systematic uncertainties, added in quadrature to the statistical errors, are shown in the figures as the outer error bars:

$$\delta_{combined\pm} = \sqrt{\delta^2_{stat} + \delta^2_{syst\pm}}$$

Additionally the jet energies on detector level were varied by ±3%. This systematic check was not added to the total systematics, but can be found in the plots as the jet energy scale uncertainty.

8.10 Parton to Hadron Level Corrections of NLO Calculations

The NLO calculation predicts cross sections on the parton level. Data and NLO were compared at the hadron level. Therefore the NLO cross sections were corrected to hadron level. The hadronization correction factor is the ratio of the hadron level cross section to the parton level cross section of the Monte Carlo.

$$C_{had} = \frac{\sigma_{hadron}}{\sigma_{parton}}$$

For this correction the LEPTO Monte Carlo sample was used, because the parton level of this Monte Carlo had a closer resemblance to the parton level of NLOjet.

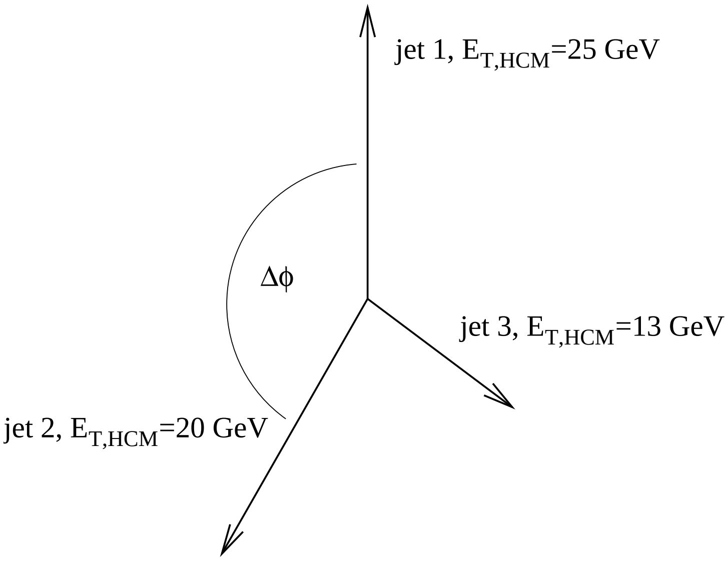

Figure 8.3: Example trijet configuration. This figure is shown in the transverse momentum plane of the hadronic center of mass frame.

8.11 Definition of the Chosen Variables

The di- and trijet cross sections were measured and calculated single-differentially as functions of Q^2, $x_{\rm Bj}$, $E_{T,\rm HCM}^{\rm jet1,2(,3)}$ and $\eta_{\rm LAB}^{\rm jet1,2(,3)}$. These variables have been described above. Also $|\Delta\eta_{\rm HCM}^{\rm jet1,2}|$, the absolute difference in pseudorapidity of the two highest-E_T jets in the HCM-frame, was measured.
Double-differential cross sections were measured as functions of $x_{\rm Bj}$ and variables depending on the configuration of the first two (i.e. highest-E_T) jets. These were the following:

- $|\Delta\phi_{\rm HCM}^{\rm jet1,2}|$: The absolute difference in azimuthal angle of the two highest-E_T jets in the HCM-frame.

- $\Delta E_{T,\rm HCM}^{\rm jet1,2}$: The absolute difference in transverse energy of the two highest-E_T jets in the HCM-frame.

- $|\Delta\vec{p}_{T,\rm HCM}^{\rm jet1,2}|$: The magnitude of the vectorial difference of the transverse momenta of the two highest-E_T jets in the HCM-frame.

- $|\Delta\vec{p}_{T,\rm HCM}^{\rm jet1,2}|/(2E_{T,\rm HCM}^{\rm jet1})$: The magnitude of the vectorial difference of the transverse momenta of the two highest-E_T jets in the HCM-frame divided by two times the transverse energy of the highest-E_T jet. This variable only depends on the geometrical configuration of the jets and the ratio of their transverse energies:

$$|\Delta\vec{p}_{T,\mathrm{HCM}}^{\,\mathrm{jet1,2}}|/(2E_{T,\mathrm{HCM}}^{\mathrm{jet1}}) = \sqrt{1+r^2-2rcos(\Delta\phi_{\mathrm{HCM}}^{\mathrm{jet1,2}})}, \text{with } r = \frac{E_{T,\mathrm{HCM}}^{\mathrm{jet2}}}{E_{T,\mathrm{HCM}}^{\mathrm{jet1}}}$$

- $|\Sigma\vec{p}_{T,\mathrm{HCM}}^{\,\mathrm{jet1,2}}|$:The magnitude of the vectorial sum of the transverse momenta of the two highest-E_T jets in the HCM-frame.

The variable x_{Bj} was chosen because the applicability of the DGLAP-evolution is expected to depend on x_{Bj}, as described in chapter 2.

All the variables that were double-differentially measured are dependent on the balance of the transverse momenta. Figure 8.3 shows an exemplary trijet configuration. In the ideal picture, the momenta of the jets add up to zero. In an exclusive two-jet event, the jets point into opposite directions ($|\Delta\phi_{\mathrm{HCM}}^{\mathrm{jet1,2}}| = 180° = \pi$). With exactly three jets, the minimum angle between the two highest-$E_{T,\mathrm{HCM}}$ jets is $|\Delta\phi_{\mathrm{HCM}}^{\mathrm{jet1,2}}| = 120° = 2/3\pi$. Smaller angles indicate four or more jets. Some of these additional jets can remain unobserved outside the measured pseudorapidity region. This makes the measurement sensitive to highly energetic forward jets.

The variables $\Delta\phi_{\mathrm{HCM}}^{\mathrm{jet1,2}}$ and $\Delta E_{T,\mathrm{HCM}}^{\mathrm{jet1,2}}$ are sensitive to higher order processes. Because of momentum conservation pure dijets would be back-to-back with equal E_T[1]. Further radiations will change the configuration of the first two jets, so that they are no longer back-to-back.

$\Delta\vec{p}_{T,\mathrm{HCM}}^{\,\mathrm{jet1,2}}/(2E_{T,\mathrm{HCM}}^{\mathrm{jet1}})$ has its maximum at unity, when the first two jets are back-to-back with equal transverse energy. This variable gives a handle on the geometrical configuration of the jets and thus gives information similar to $\Delta\phi_{\mathrm{HCM}}^{\mathrm{jet1,2}}$, but taking into account the energy ratio of the jets.

$\Sigma\vec{p}_{T,\mathrm{HCM}}^{\,\mathrm{jet1,2}}$ is very similar to $\Delta E_{T,\mathrm{HCM}}^{\mathrm{jet1,2}}$, because the first two jets are mostly pointing into opposite directions in the transverse momentum plane. It adds a dependence on the azimuthal correlation between the first two jets. Otherwise it is very similar to $\Delta E_{T,\mathrm{HCM}}^{\mathrm{jet1,2}}$.

---

[1] This neglects the transverse momentum of the initial parton with respect to the direction of the proton momentum

Chapter 9

Results

9.1 Single-differential cross sections $d\sigma/dQ^2$, $d\sigma/dx_{\mathrm{Bj}}$ and trijet to dijet cross section ratios

The single-differential cross-sections $d\sigma/dQ^2$ and $d\sigma/dx_{\mathrm{Bj}}$ for dijet and trijet production are presented in Figs. 9.1(a) and (c), and Tables B.1 – B.13. The ratio $\sigma_{\mathrm{trijet}}/\sigma_{\mathrm{dijet}}$ of the trijet cross section to the dijet cross section, as a function of Q^2 and of x_{Bj} are presented in Figs. 9.1(b) and 9.1(d), respectively. The ratio $\sigma_{\mathrm{trijet}}/\sigma_{\mathrm{dijet}}$ is almost Q^2 independent, as shown in Fig. 9.1(b), but falls steeply with increasing x_{Bj}, as shown in Fig. 9.1(d). In cross-section ratios, the experimental and theoretical uncertainties partially cancel, providing a possibility to test the pQCD calculations more precisely than can be done with the individual cross sections. Both the cross sections and the cross-section ratios are well-described by the NLOJET calculations.

9.2 Transverse energy and pseudorapidity dependencies of cross sections

The single-differential cross sections $d\sigma/dE^{\mathrm{jet}}_{T,\mathrm{HCM}}$ for two (three) jet events are presented in Fig. 9.2. The measured cross sections are well-described by the NLOJET calculations over the whole range in $E^{\mathrm{jet}}_{T,\mathrm{HCM}}$ considered.

The single-differential cross sections $d\sigma/d\eta^{\mathrm{jet}}_{\mathrm{LAB}}$ for dijet and trijet production are presented in Figs. 9.3(a) and 9.3(c). For this figure, the two (three) jets with highest $E^{\mathrm{jet}}_{T,\mathrm{HCM}}$ were ordered in $\eta^{\mathrm{jet}}_{\mathrm{LAB}}$. Also shown are the measurements of the single-differential cross sections $d^2\sigma/d|\Delta\eta^{\mathrm{jet1,2}}_{\mathrm{HCM}}|$, where $|\Delta\eta^{\mathrm{jet1,2}}_{\mathrm{HCM}}|$ is the absolute difference in pseudorapidity of the two jets with highest $E^{\rm jet}_{T,\rm HCM}$ (see Figs. 9.3(b) and 9.3(d)). The NLOJET predictions describe the measurements well.

9.3 Jet transverse energy and momentum correlations

Correlations in transverse energy of the jets have been investigated by measuring the double-differential cross-sections $d^2\sigma/dx_{\rm Bj}d\Delta E^{\rm jet1,2}_{T,\rm HCM}$, where $\Delta E^{\rm jet1,2}_{T,\rm HCM}$ is the difference in transverse energy between the two jets with the highest $E^{\rm jet}_{T,\rm HCM}$. The measurement was performed in $x_{\rm Bj}$ bins, which are defined in Table B.2, for dijet and trijet production. Figures 9.4 and 9.5 show the cross-sections $d^2\sigma/dx_{\rm Bj}d\Delta E^{\rm jet1,2}_{T,\rm HCM}$ for all bins in $x_{\rm Bj}$ for the dijet and trijet samples, respectively.

The NLOJET calculations at $\mathcal{O}(\alpha_s^2)$ do not describe the high-$\Delta E^{\rm jet1,2}_{T,\rm HCM}$ tail of the dijet sample at low $x_{\rm Bj}$, where the calculations fall below the data. Since these calculations give the lowest-order non-trivial contribution to the cross section in the region $\Delta E^{\rm jet1,2}_{T,\rm HCM} > 0$, they are affected by large uncertainties from the higher-order terms in α_s. A higher-order calculation for the dijet sample is possible with NLOJET if the region $\Delta E^{\rm jet1,2}_{T,\rm HCM}$ near zero is avoided. NLOJET calculations at $\mathcal{O}(\alpha_s^3)$ for the dijet sample have been obtained for the region $\Delta E^{\rm jet1,2}_{T,\rm HCM} > 4\,{\rm GeV}$ and are compared to the data in Fig. 9.4. With the inclusion of the next term in the perturbative series in α_s, the NLOJET calculations describe the data within the theoretical uncertainties. The NLOJET calculations at $\mathcal{O}(\alpha_s^3)$ for trijet production are consistent with the measurements.

As a refinement of the studies of the correlations between the transverse energies of the jets, further correlations of the jet tranverse momenta have been investigated. The correlations in jet transverse momenta were examined by measuring the two sets of double-differential cross sections, the first of which is $d^2\sigma/dx_{\rm Bj}d|\Sigma\vec{p}^{\rm\, jet1,2}_{T,\rm HCM}|$, where $|\Sigma\vec{p}^{\rm\, jet1,2}_{T,\rm HCM}|$ is the transverse component of the vector sum of the jet momenta of the two jets with the highest $E^{\rm jet}_{T,\rm HCM}$. For events with only two jets $|\Sigma\vec{p}^{\rm\, jet1,2}_{T,\rm HCM}| = 0$, additional QCD radiation increases this value. The second cross section used to study the correlations in jet transverse momenta is $d^2\sigma/dx_{\rm Bj}d(|\Delta\vec{p}^{\rm\, jet1,2}_{T,\rm HCM}|/(2E^{\rm jet1}_{T,\rm HCM}))$, where $|\Delta\vec{p}^{\rm\, jet1,2}_{T,\rm HCM}|/(2E^{\rm jet1}_{T,\rm HCM})$ is the magnitude of the vector difference of the transverse momenta of the two jets with the highest $E^{\rm jet}_{T,\rm HCM}$ scaled by twice the transverse energy of the hardest jet. For events with only two jets $|\Delta\vec{p}^{\rm\, jet1,2}_{T,\rm HCM}|/(2E^{\rm jet1}_{T,\rm HCM}) = 1$. Additional QCD radiation decreases this value.

Figures 9.6 – 9.9 show the cross-sections $d^2\sigma/dx_{\rm Bj}d|\Sigma\vec{p}_{T,{\rm HCM}}^{\rm jet1,2}|$ and the cross-sections $d^2\sigma/dx_{\rm Bj}d|\Delta\vec{p}_{T,{\rm HCM}}^{\rm jet1,2}|/(2E_{T,{\rm HCM}}^{\rm jet1})$ in bins of $x_{\rm Bj}$ for the dijet and trijet samples.
At low $x_{\rm Bj}$, the NLOJET calculations at $\mathcal{O}(\alpha_s^2)$ underestimate the dijet cross sections at high values of $|\Sigma\vec{p}_{T,{\rm HCM}}^{\rm jet1,2}|$ and low values of $|\Delta\vec{p}_{T,{\rm HCM}}^{\rm jet1,2}|/(2E_{T,{\rm HCM}}^{\rm jet1})$. The description of the data by the NLOJET calculations at $\mathcal{O}(\alpha_s^2)$ improves at higher values of $x_{\rm Bj}$. A higher-order calculation with NLOJET at $\mathcal{O}(\alpha_s^3)$ for the dijet sample has been obtained for the region $|\Sigma\vec{p}_{T,{\rm HCM}}^{\rm jet1,2}| > 4\,{\rm GeV}$, which is compared to the data in Fig. 9.6; and for the region $|\Delta\vec{p}_{T,{\rm HCM}}^{\rm jet1,2}|/(2E_{T,{\rm HCM}}^{\rm jet1}) < 0.85$, which is compared to the data in Fig. 9.8. With the inclusion of the next term in the perturbative series in α_s, the NLOJET calculations describe the data well. The NLOJET calculations at $\mathcal{O}(\alpha_s^3)$ for trijet production are consistent with the measurements.

9.4 Azimuthal distributions of the jets

Measurements of the double-differential cross section $d^2\sigma/dx_{\rm Bj}d|\Delta\phi_{\rm HCM}^{\rm jet1,2}|$, where $|\Delta\phi_{\rm HCM}^{\rm jet1,2}|$ is the azimuthal separation of the two jets with the largest $E_{T,{\rm HCM}}^{\rm jet}$, for dijet and trijet production are shown in Figs. 9.10 and 9.11 for all bins in $x_{\rm Bj}$. For dijet and trijet production the cross section falls with $|\Delta\phi_{\rm HCM}^{\rm jet1,2}|$. The NLOJET calculations at $\mathcal{O}(\alpha_S^2)$ for dijet production decrease more rapidly with $|\Delta\phi_{\rm HCM}^{\rm jet1,2}|$ than the data and the calculations disagree with the data at low $|\Delta\phi_{\rm HCM}^{\rm jet1,2}|$. A higher-order NLOJET calculation at $\mathcal{O}(\alpha_S^3)$ for the dijet sample has been obtained for the region $|\Delta\phi_{\rm HCM}^{\rm jet1,2}| < 3\pi/4$ and describes the data well. The measurements for trijet production are reasonably well described by the NLOJET calculations at $\mathcal{O}(\alpha_S^3)$.
A further investigation has been performed by measuring the cross-section $d^2\sigma/dQ^2dx_{\rm Bj}$ for dijet (trijet) events with $|\Delta\phi_{\rm HCM}^{\rm jet1,2}| < 2\pi/3$ as a function of $x_{\rm Bj}$. For the two-jet final states, the presence of two leading jets with $|\Delta\phi_{\rm HCM}^{\rm jet1,2}| < 2\pi/3$ is an indication of another high-E_T jet outside the measured η range. These cross sections are presented in Fig. 9.12. The NLOJET calculations at $\mathcal{O}(\alpha_S^2)$ for dijet production underestimate the data, the difference increasing towards low $x_{\rm Bj}$. The NLOJET calculations at $\mathcal{O}(\alpha_S^3)$ are up to one order of magnitude larger than the $\mathcal{O}(\alpha_S^2)$ calculations and are consistent with the data, demonstrating the importance of the higher-order terms in the description of the data especially at low $x_{\rm Bj}$. The NLOJET calculations at $\mathcal{O}(\alpha_S^3)$ describe the trijet data within the renormalisation scale uncertainties.

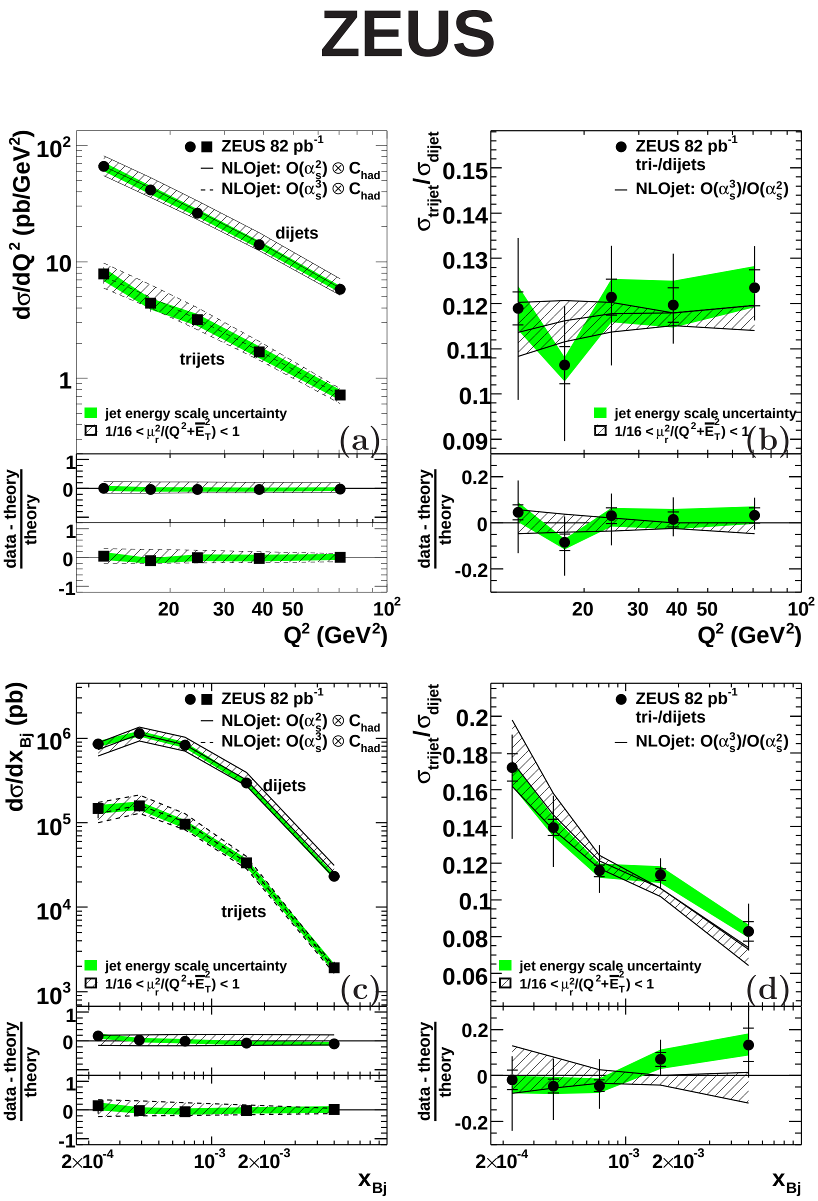

Figure 9.1: Inclusive dijet and trijet cross sections as functions of (a) Q^2 and (c) x_{Bj}. (b) and (d) show the ratios of the trijet and dijet cross sections. The inner error bars represent the statistical uncertainties. The outer error bars represent the quadratic sum of statistical and systematic uncertainties not associated with the jet energy scale. The shaded band indicates the jet energy scale uncertainty. The predictions of perturbative QCD at NLO, corrected for hadronisation effects and using the CTEQ6 parameterisations of the proton PDFs, are compared to data. The lower plots show the relative difference between the data and the corresponding theoretical prediction. The hatched band represents the renormalisation scale uncertainty of the QCD calculation.

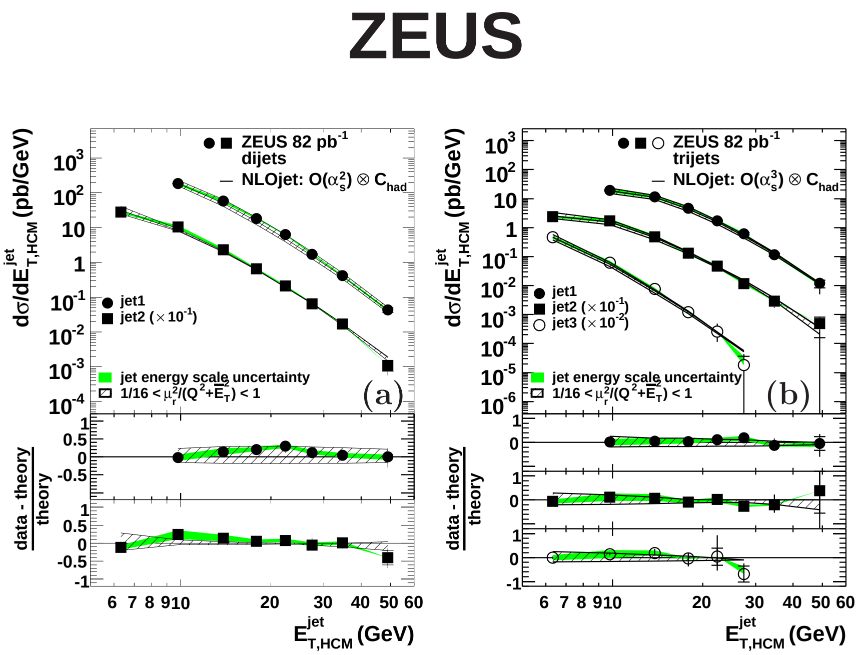

Figure 9.2: Inclusive dijet (a) and trijet (b) cross sections as functions of $E^{\rm jet}_{T,{\rm HCM}}$ with the jets ordered in $E^{\rm jet}_{T,{\rm HCM}}$. The cross sections of the second and third jet were scaled for readability. Other details as in the caption to Fig. 9.1.

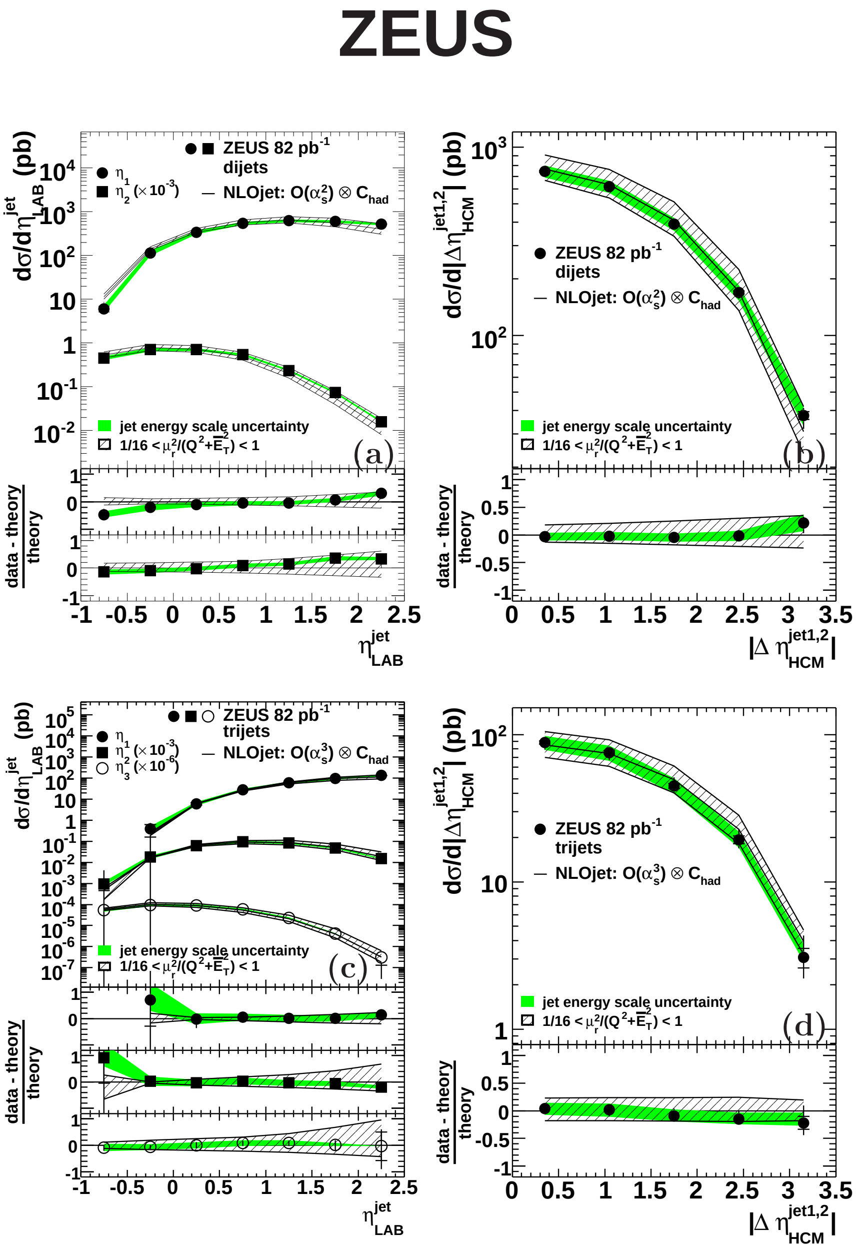

Figure 9.3: (a) and (c) show the inclusive dijet and trijet cross sections as functions of $\eta_{\rm LAB}^{\rm jet}$ with the jets ordered in $\eta_{\rm LAB}^{\rm jet}$: $\eta_{\rm LAB}^{\rm jet1} > \eta_{\rm LAB}^{\rm jet2} > \eta_{\rm LAB}^{\rm jet3}$. The cross sections of the second and third jet were scaled for readability. (b) and (d) show the dijet and trijet cross sections as functions of $|\Delta\eta_{\rm HCM}^{\rm jet1,2}|$. Other details as in the caption in Fig. 9.1.

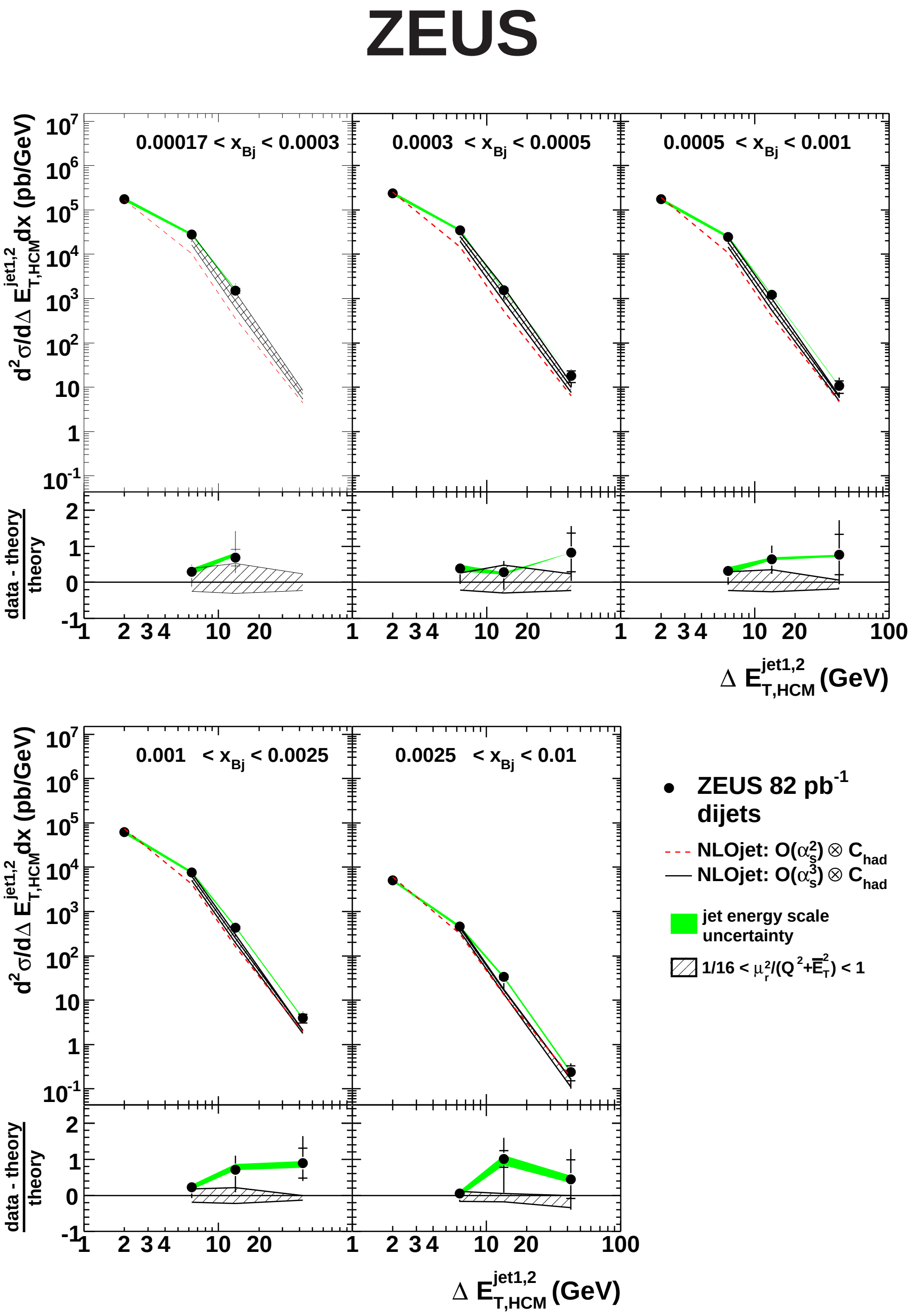

Figure 9.4: Dijet cross sections as functions of $\Delta E_{T,\mathrm{HCM}}^{\mathrm{jet1,2}}$. For comparison with the dijet measurements, NLOjet calculations at $\mathcal{O}(\alpha_s^2)$ ($\mathcal{O}(\alpha_s^3)$) are shown as dashed (solid) lines. The lower plots show the relative difference between the data and the $\mathcal{O}(\alpha_s^3)$ predictions. The boundaries for the bins in $\Delta E_{T,\mathrm{HCM}}^{\mathrm{jet1,2}}$ are given in Table B.25. Other details as in the caption to Fig. 9.1.

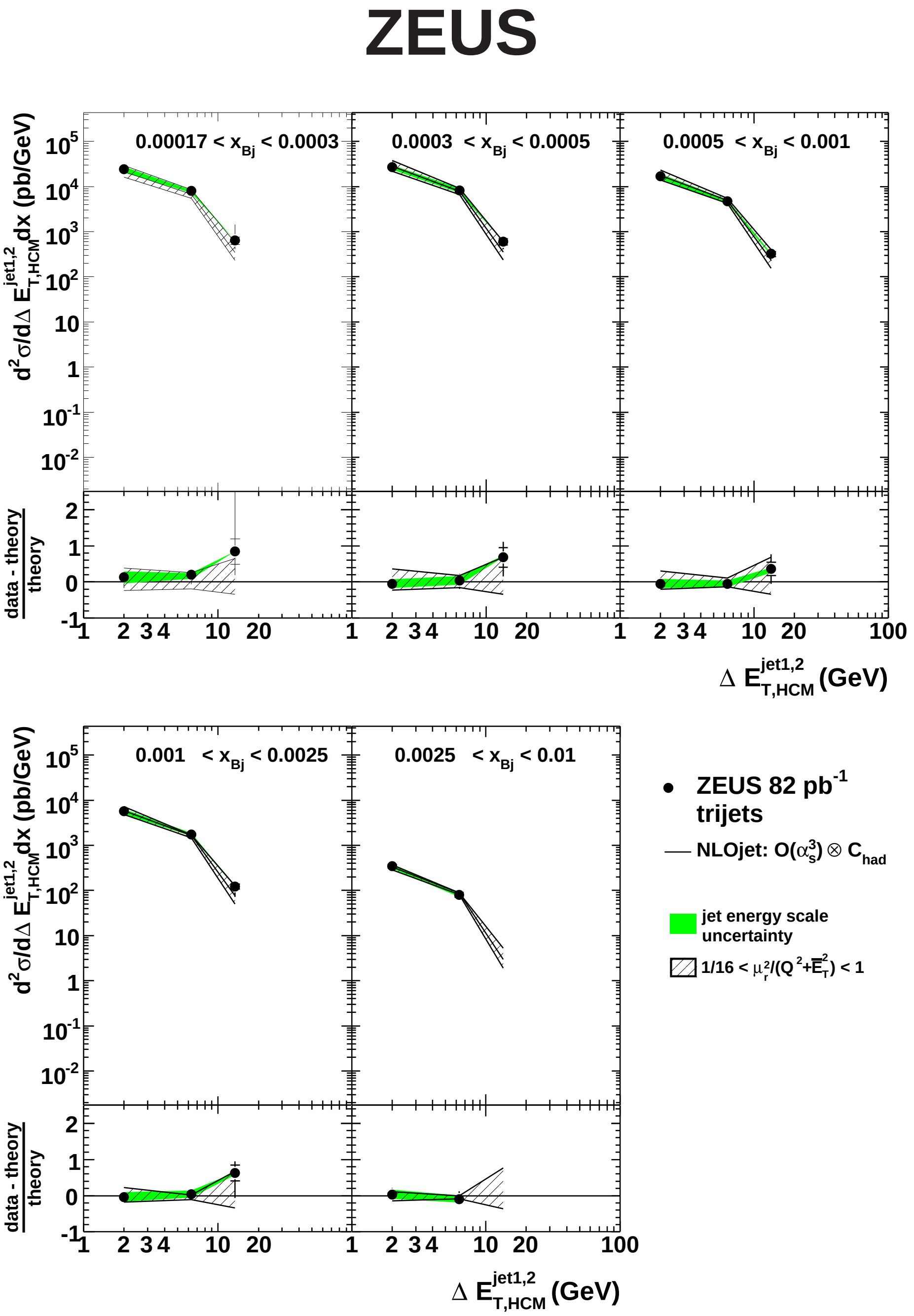

Figure 9.5: Trijet cross sections as functions of $\Delta E^{\text{jet1,2}}_{T,\text{HCM}}$. The measurements are compared to NLOJET calculations at $\mathcal{O}(\alpha_s^3)$. The boundaries for the bins in $\Delta E^{\text{jet1,2}}_{T,\text{HCM}}$ are given in Table B.25. Other details as in the caption to Fig. 9.1.

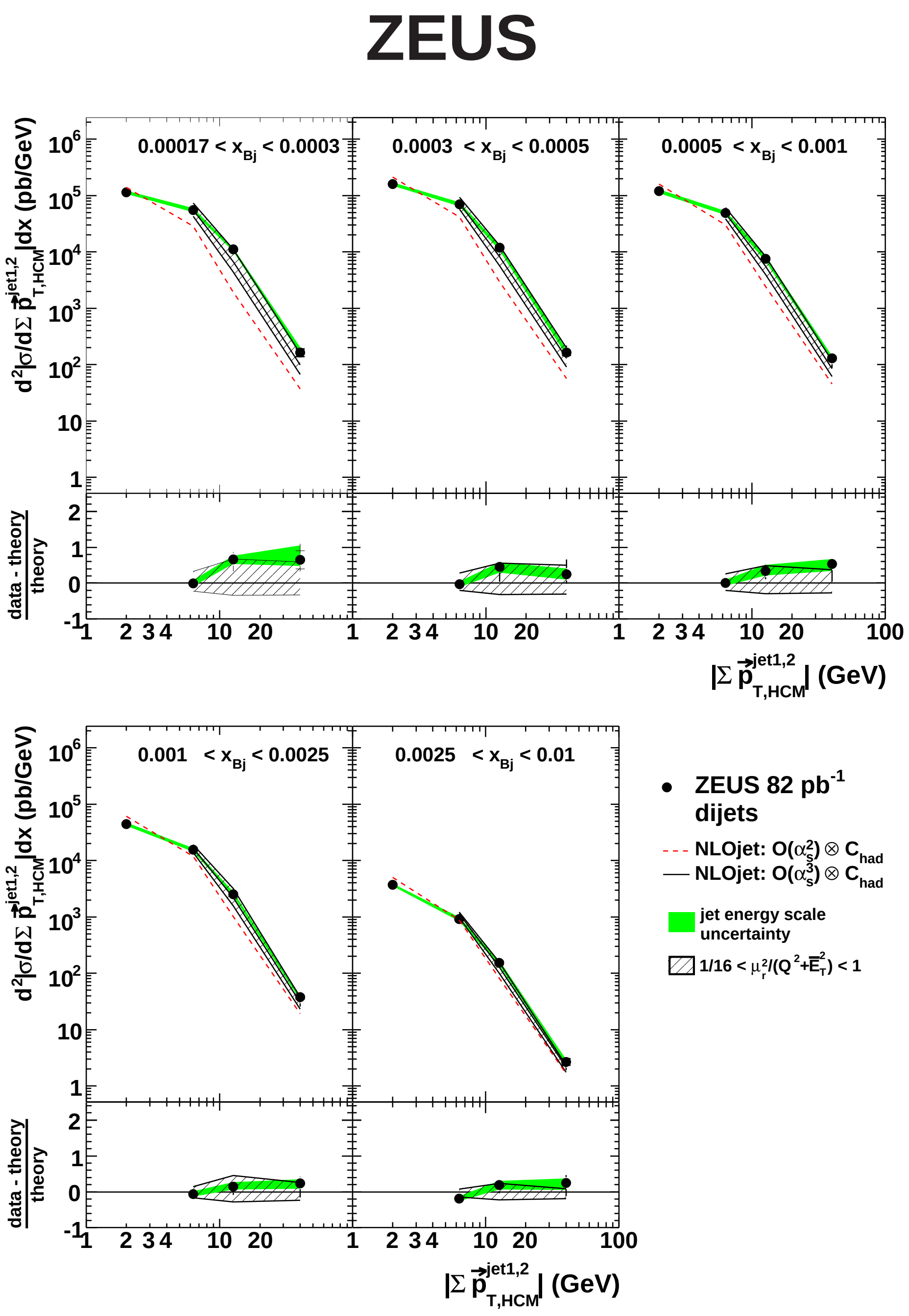

Figure 9.6: Dijet cross sections as functions of $|\Sigma p_{T,\mathrm{HCM}}^{\mathrm{jet1,2}}|$. For comparison with the dijet measurements, NLOJET calculations at $\mathcal{O}(\alpha_s^2)$ ($\mathcal{O}(\alpha_s^3)$) are shown as dashed (solid) lines. The lower plots show the relative difference between the data and the $\mathcal{O}(\alpha_s^3)$ predictions. The boundaries for the bins in $|\Sigma p_{T,\mathrm{HCM}}^{\mathrm{jet1,2}}|$ are given in Table B.25. Other details as in the caption to Fig. 9.1.

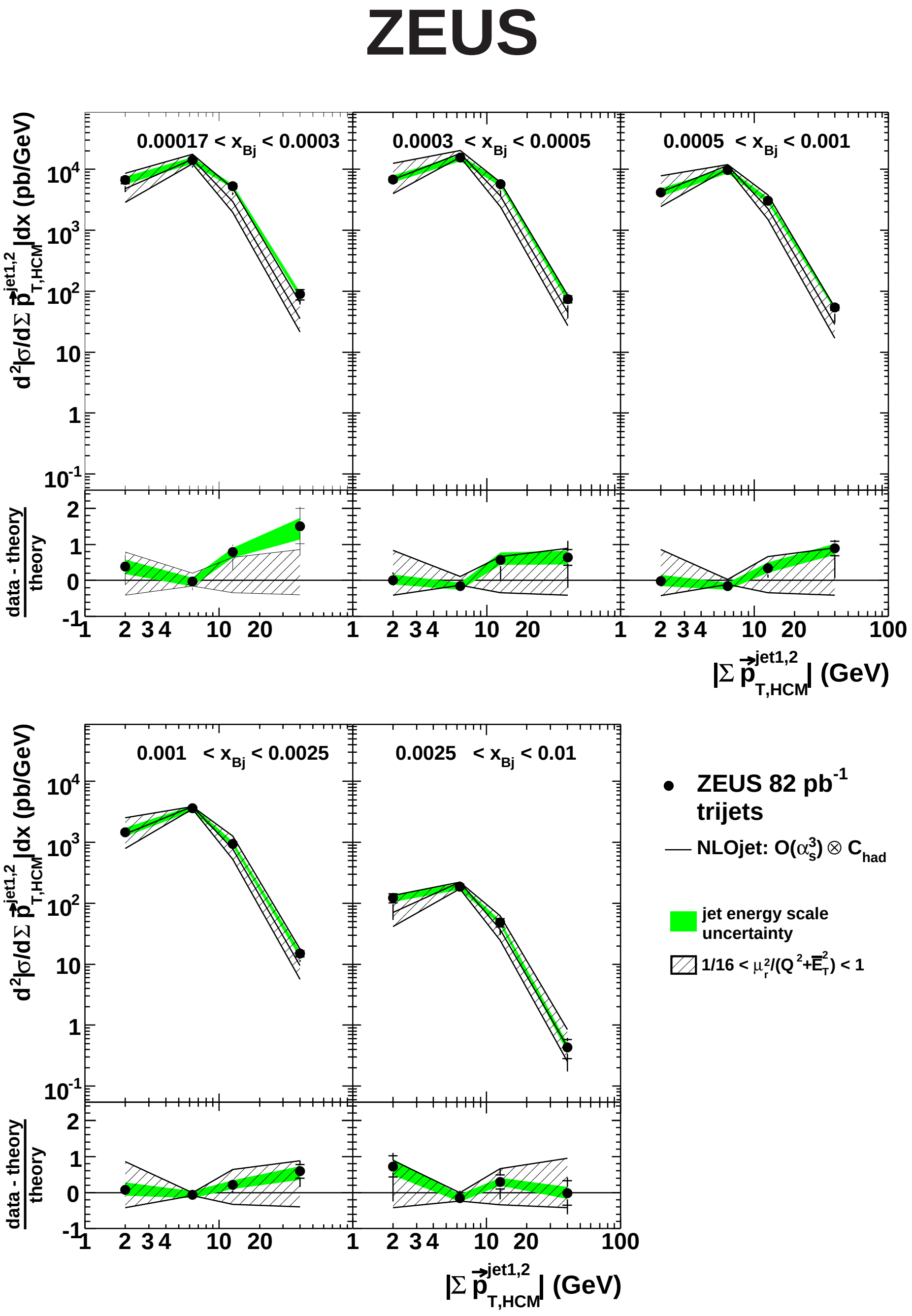

Figure 9.7: Trijet cross sections as functions of $|\Sigma p_{T,\mathrm{HCM}}^{\mathrm{jet1,2}}|$. The measurements are compared to NLOJET calculations at $\mathcal{O}(\alpha_s^3)$. The boundaries for the bins in $|\Sigma p_{T,\mathrm{HCM}}^{\mathrm{jet1,2}}|$ are given in Table B.25. Other details as in the caption to Fig. 9.1.

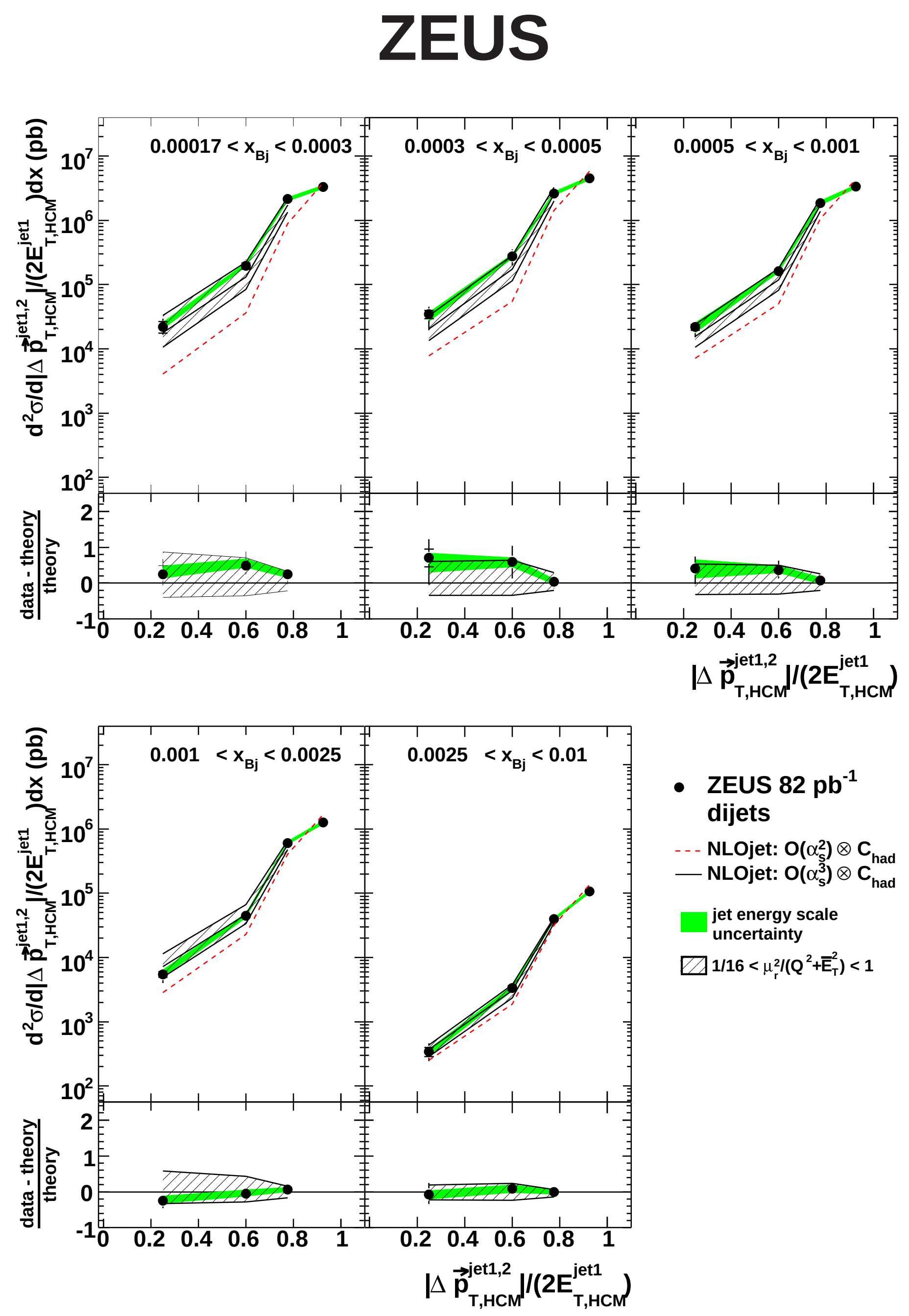

Figure 9.8: Dijet cross sections as functions of $|\Delta p_{T,\mathrm{HCM}}^{\mathrm{jet1,2}}|/(2E_{T,\mathrm{HCM}}^{\mathrm{jet1}})$. For comparison with the dijet measurements, NLOJET calculations at $\mathcal{O}(\alpha_s^2)$ ($\mathcal{O}(\alpha_s^3)$) are shown as dashed (solid) lines. The lower plots show the relative difference between the data and the $\mathcal{O}(\alpha_s^3)$ predictions. The boundaries for the bins in $|\Delta p_{T,\mathrm{HCM}}^{\mathrm{jet1,2}}|/(2E_{T,\mathrm{HCM}}^{\mathrm{jet1}}$ are given in Table B.25. Other details as in the caption to Fig. 9.1.

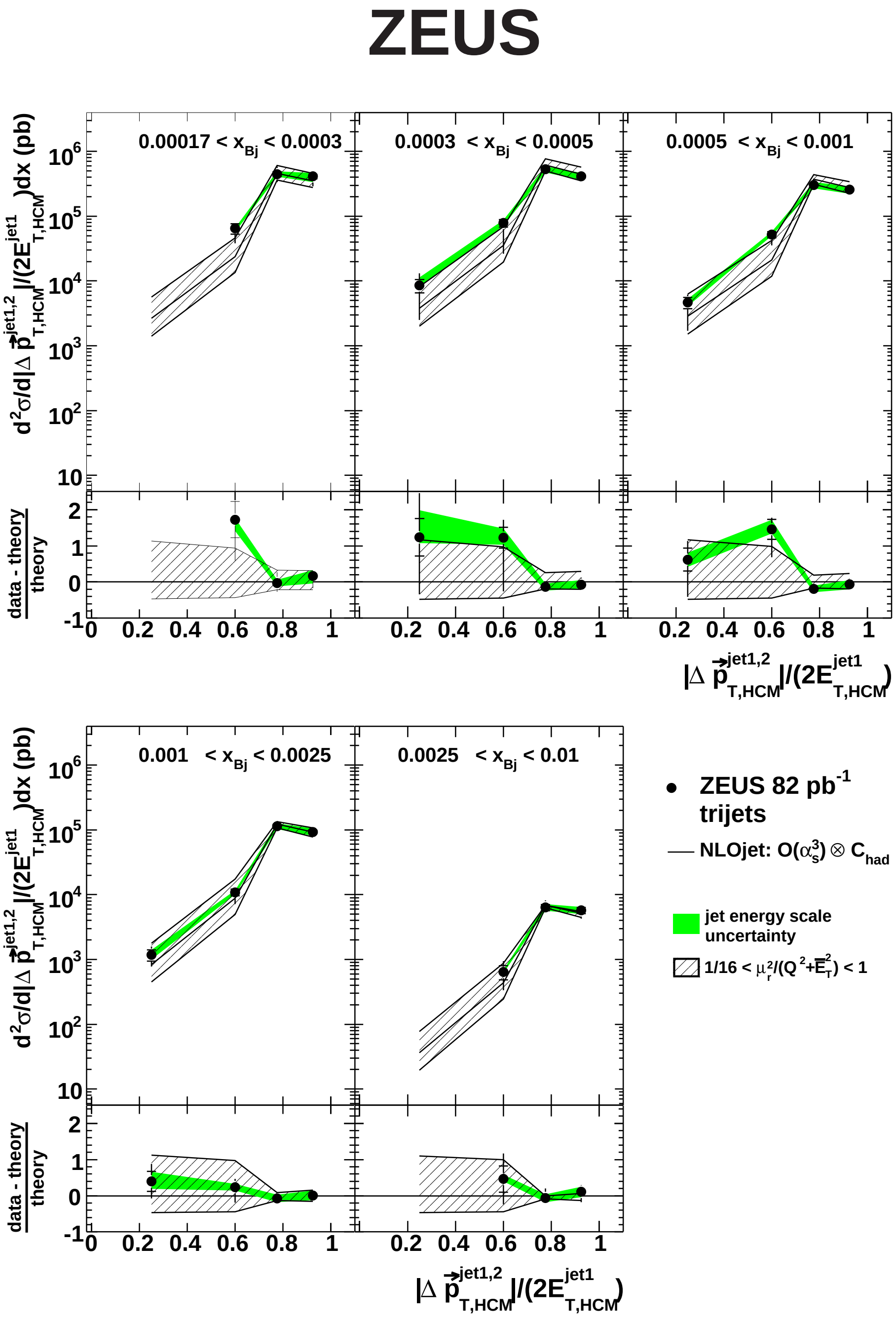

Figure 9.9: Trijet cross sections as functions of $|\Delta p_{T,\mathrm{HCM}}^{\mathrm{jet1,2}}|/(2E_{T,\mathrm{HCM}}^{\mathrm{jet1}})$. The measurements are compared to NLOJET calculations at $\mathcal{O}(\alpha_s^3)$. The boundaries for the bins in $|\Delta p_{T,\mathrm{HCM}}^{\mathrm{jet1,2}}|/(2E_{T,\mathrm{HCM}}^{\mathrm{jet1}})$ are given in Table B.25. Other details as in the caption to Fig. 9.1.

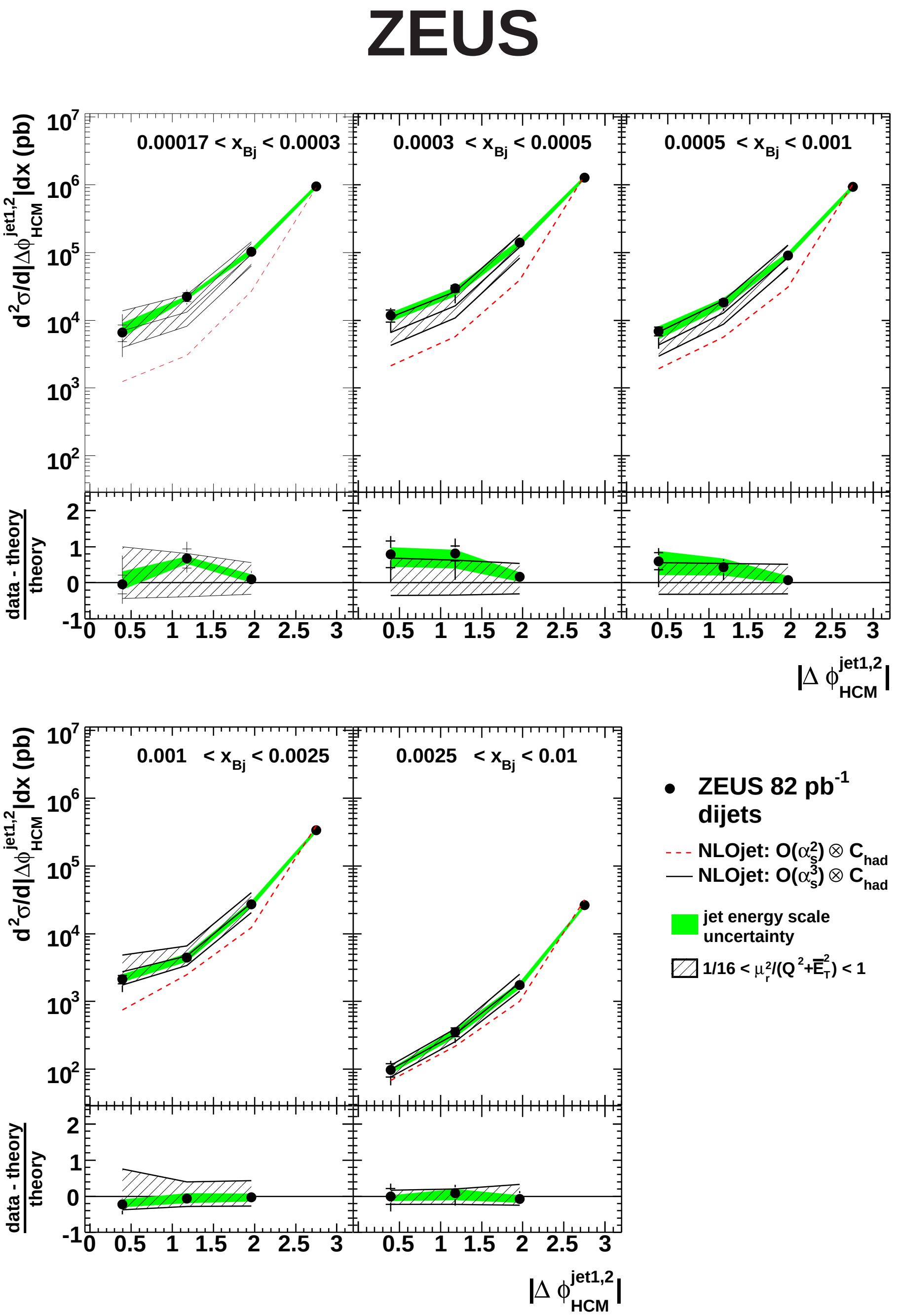

Figure 9.10: Dijet cross sections as functions of $|\Delta\phi^{\rm jet1,2}_{\rm HCM}|$. For comparison with the dijet measurements, NLOJET calculations at $\mathcal{O}(\alpha_s^2)$ ($\mathcal{O}(\alpha_s^3)$) are shown as dashed (solid) lines. The lower plots show the relative difference between the data and the $\mathcal{O}(\alpha_s^3)$ predictions. The boundaries for the bins in $|\Delta\phi^{\rm jet1,2}_{\rm HCM}|$ are given in Table B.25. Other details as in the caption to Fig. 9.1.

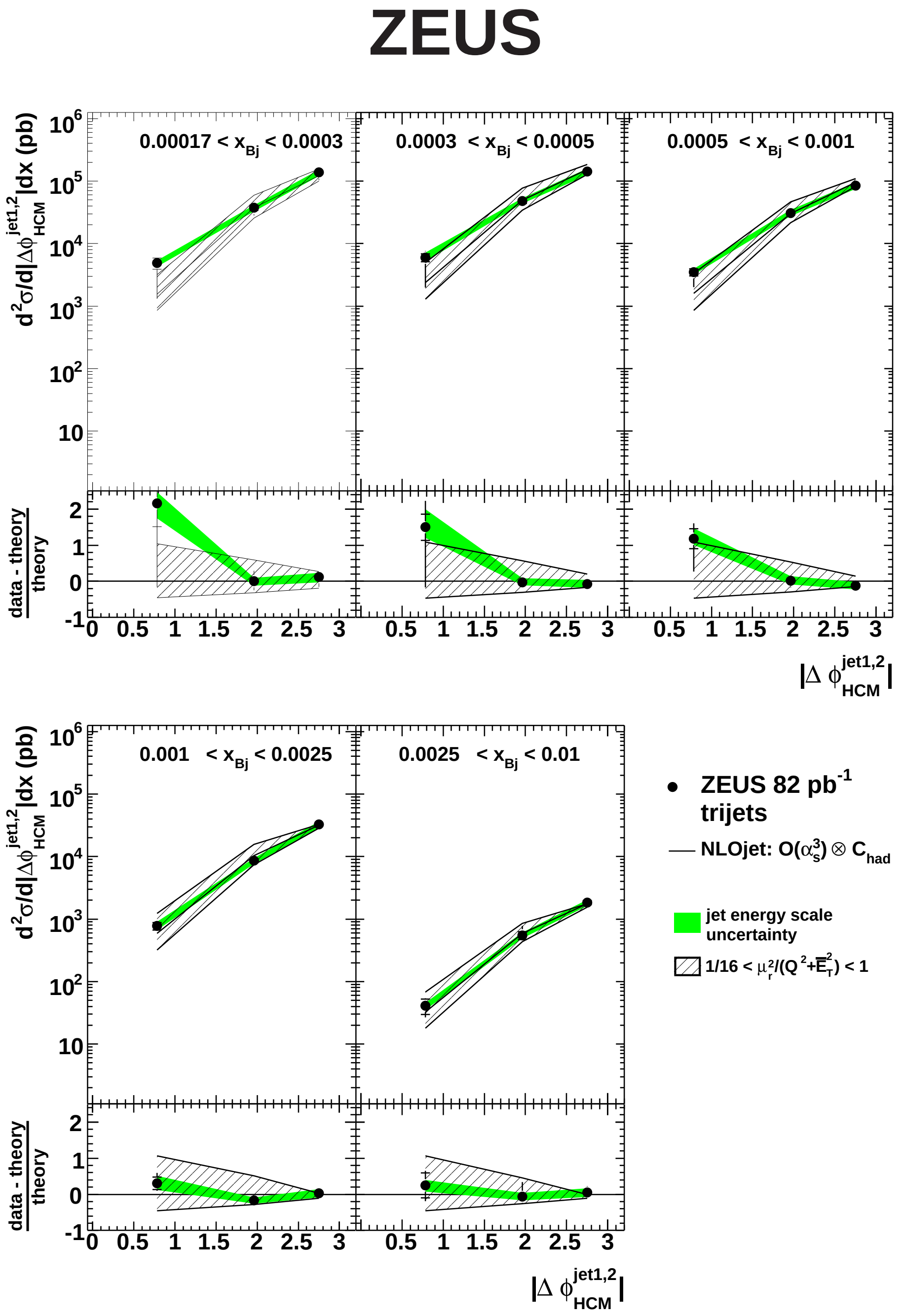

Figure 9.11: Trijet cross sections as functions of $|\Delta\phi^{\rm jet1,2}_{\rm HCM}|$. The measurements are compared to NLOJET calculations at $\mathcal{O}(\alpha_s^3)$. The boundaries for the bins in $|\Delta\phi^{\rm jet1,2}_{\rm HCM}|$ are given in Table B.25. Other details as in the caption to Fig. 9.1.

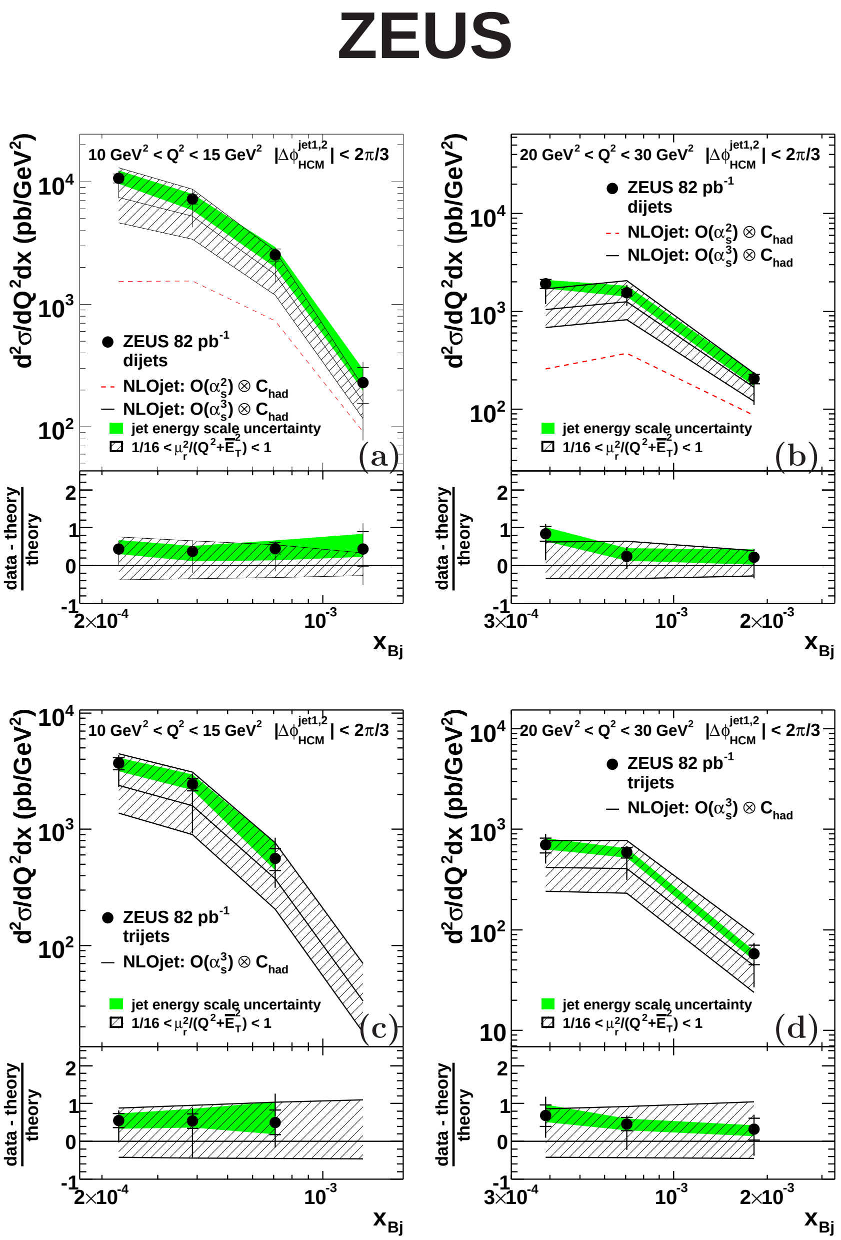

Figure 9.12: The dijet and trijet cross sections for events with $|\Delta\phi_{\rm HCM}^{\rm jet1,2}| < 120°$ as functions of x_{Bj} in two different Q^2-bins. For comparison with the dijet measurements, NLOJET calculations at $\mathcal{O}(\alpha_s^2)$ ($\mathcal{O}(\alpha_s^3)$) are shown as dashed (solid) lines. The trijet measurements are compared to NLOJET calculations at $\mathcal{O}(\alpha_s^3)$. The lower plots in (a) and (b) show the relative difference between the data and the $\mathcal{O}(\alpha_s^3)$ predictions. Other details as in the caption to Fig. 9.1.

Chapter 10

Summary and Conclusions

Dijet and trijet production in deep inelastic *ep* scattering has been measured in the phase space region $10\,\mathrm{GeV}^2 < Q^2 < 100\,\mathrm{GeV}^2$ and $10^{-4} < x_{\mathrm{Bj}} < 10^{-2}$ using an integrated luminosity of 82 pb^{-1} collected by the ZEUS experiment. The high statistics have made possible detailed studies of multijet production at low x_{Bj}. The dependence of dijet and trijet production on the kinematic variables Q^2 and x_{Bj} and on the jet variables $E_{T,\mathrm{HCM}}^{\mathrm{jet}}$ and $\eta_{\mathrm{LAB}}^{\mathrm{jet}}$ is well described by perturbative QCD calculations which include next-to-lowest-order corrections. To investigate possible deviations with respect to the collinear factorization approximation used in the standard pQCD approach, measurements of the correlations between the two jets with highest $E_{T,\mathrm{HCM}}^{\mathrm{jet}}$ have been made. At low x_{Bj}, measurements of dijet production with low azimuthal separation are reproduced by the perturbative QCD calculations provided that higher-order terms ($\mathcal{O}(\alpha_s^3)$) are accounted for. Such terms increase the predictions by pQCD calculations by up to one order of magnitude when the two jets with the highest $E_{T,\mathrm{HCM}}^{\mathrm{jet1,2}}$ are not balanced in transverse momentum. This demonstrates their importance in the low-x_{Bj} region.
Compared to the studies in [20], the phase space was the same, except for the region below $Q^2 = 10\,\mathrm{GeV}^2$, but the agreement between data and the theoretical calculations was found to be reasonable even for the azimuthal correlations in dijet events, when the $\mathcal{O}(\alpha_s^3)$ terms were included.

The 6m Tagger was calibrated and measurements of the photon acceptance of the Photon Calorimeter and the Spectrometer were performed. For the future, a cell-by-cell calibration of the 6m Tagger would be desirable. The acceptance measurement of the Photon Calorimeter showed the importance of the knowledge of the beam spread. The combination of the data from several runs could increase the statistical accuracy and could further constrain the acceptances.

Appendix A

Comparison of Data and Monte Carlo at Detector Level

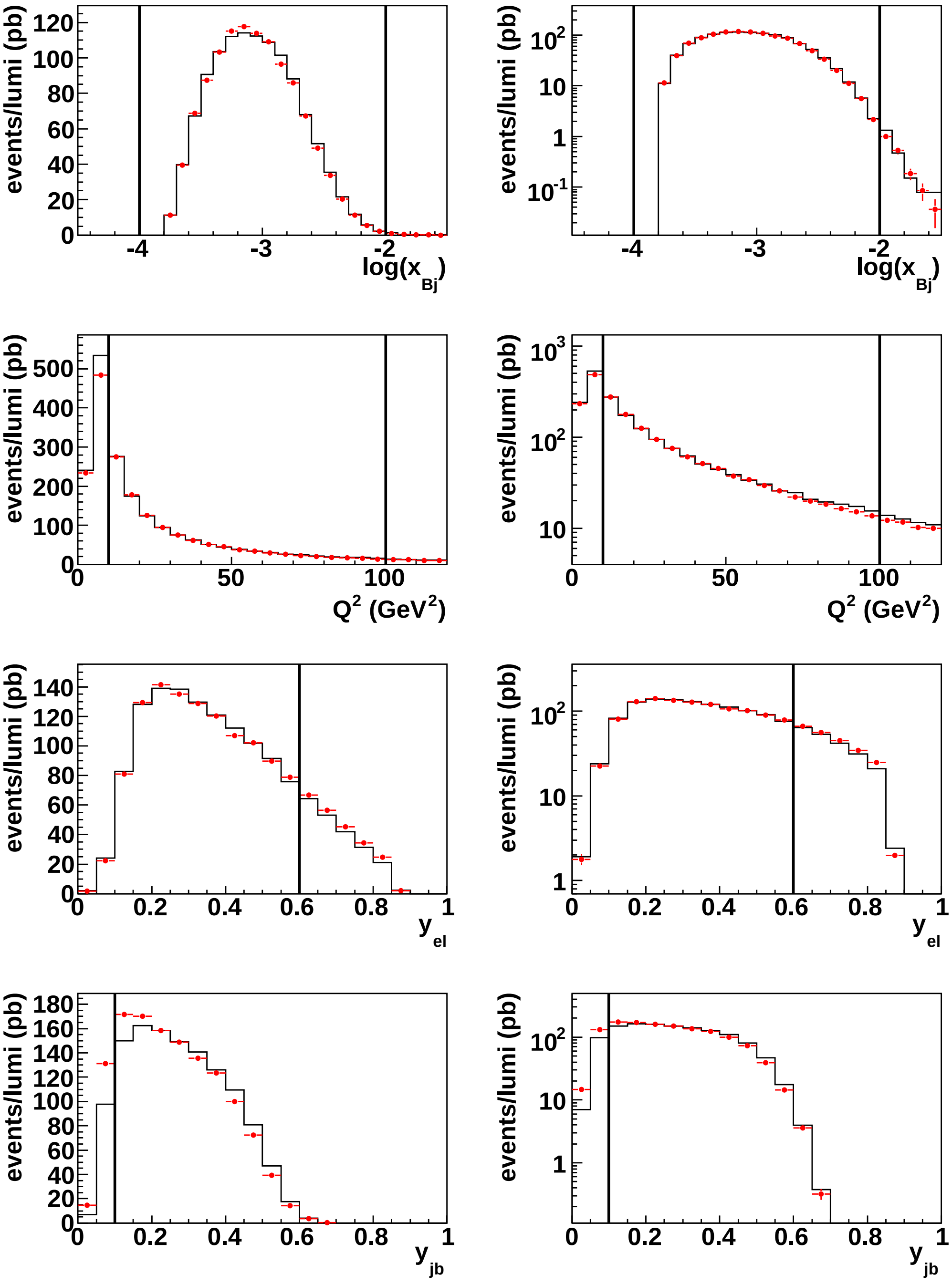

Figure A.1: Comparison of data and ARIADNE at detector level for dijet events. The data are the dots, the Monte Carlo is shown as histograms. The Monte Carlo has been normalized to the data inside the cuts. The vertical lines show the cuts on the variables. On the left side is linear scale, on the right log scale.

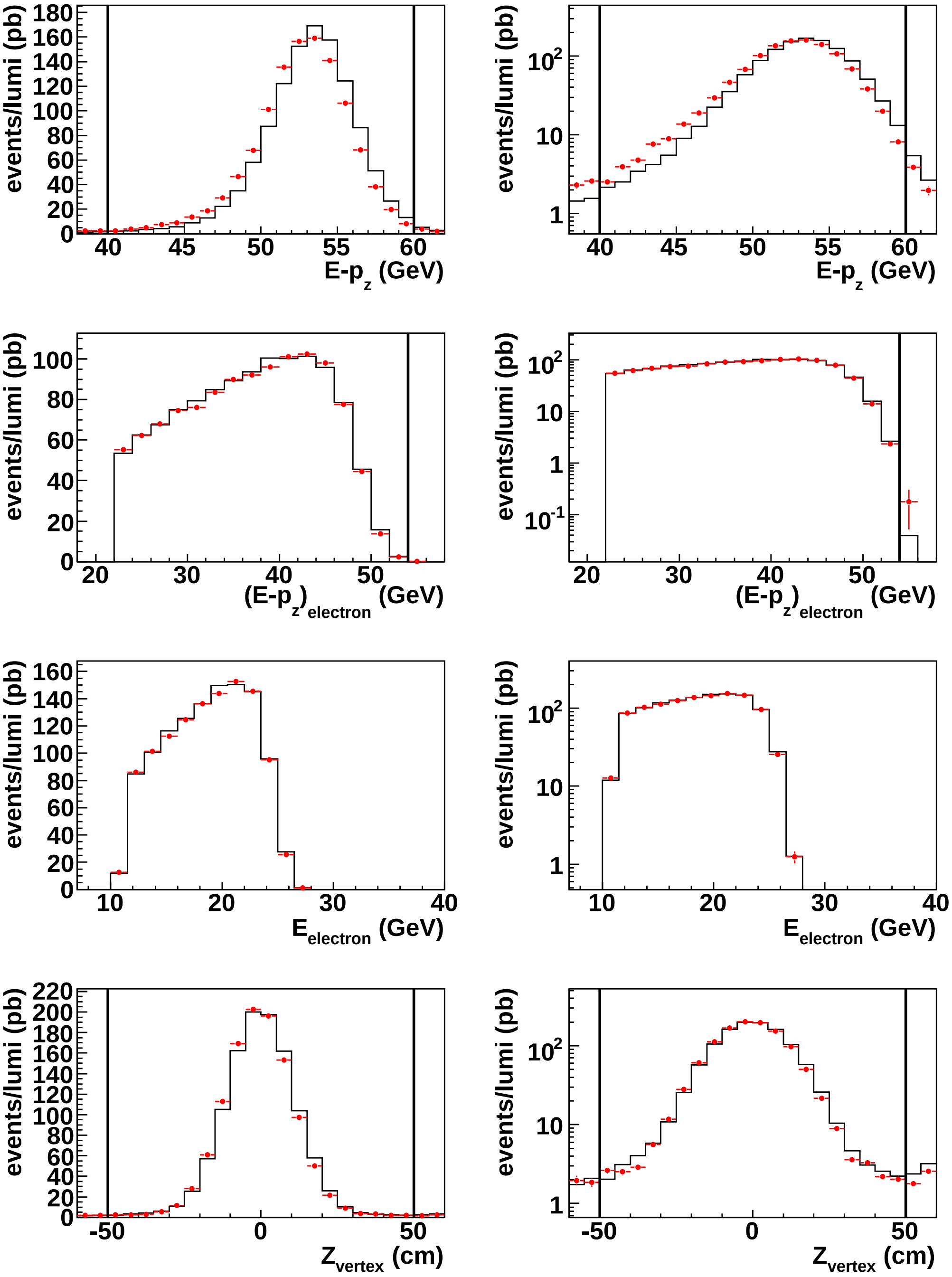

Figure A.2: Data vs. ARIADNE, dijet, continued

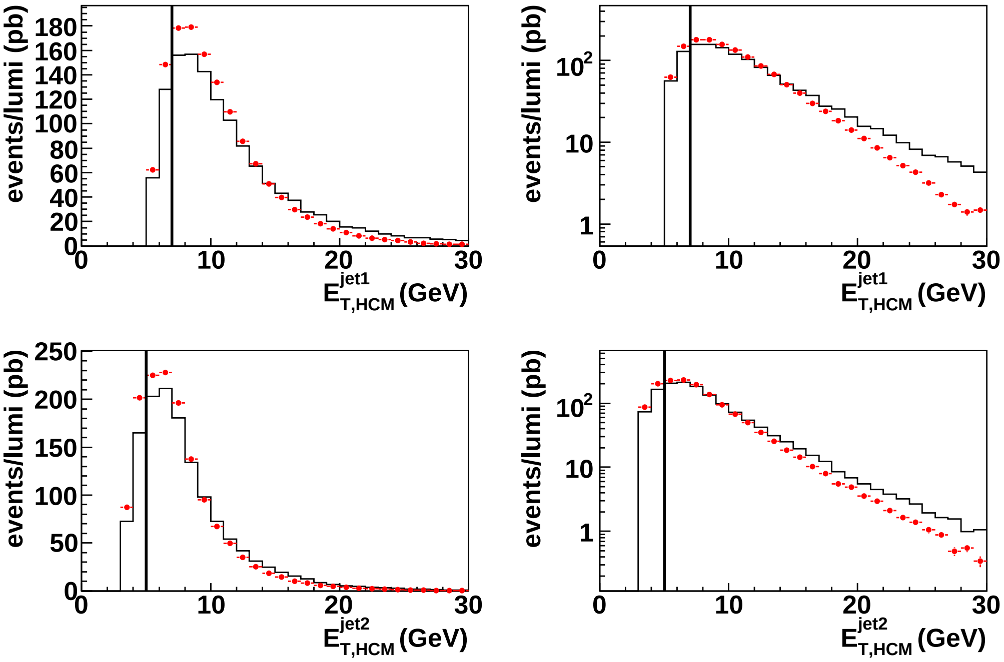

Figure A.3: Data vs. ARIADNE, dijet, jet transverse energies

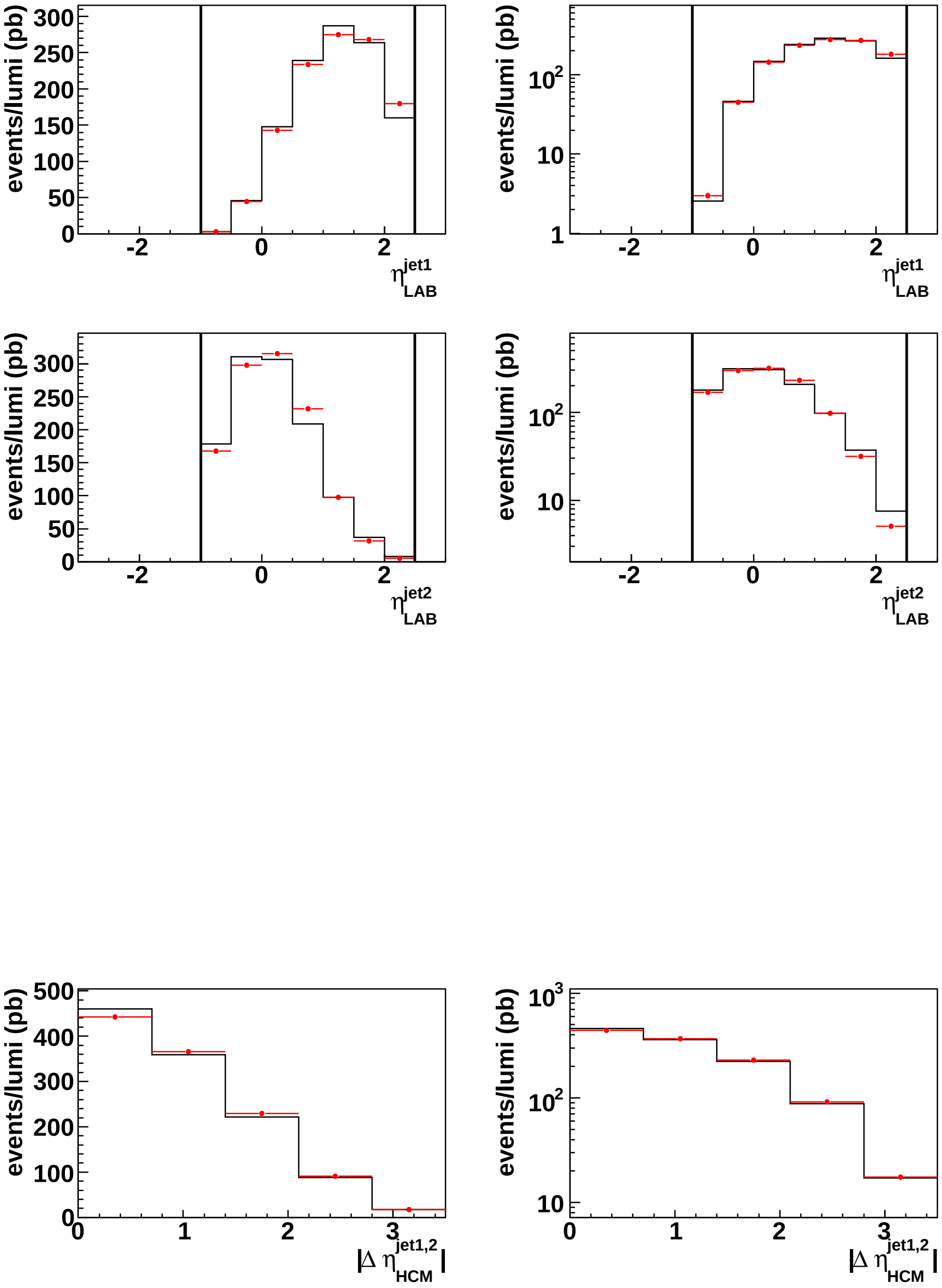

Figure A.4: Data vs. ARIADNE, dijet, jet pseudorapidities

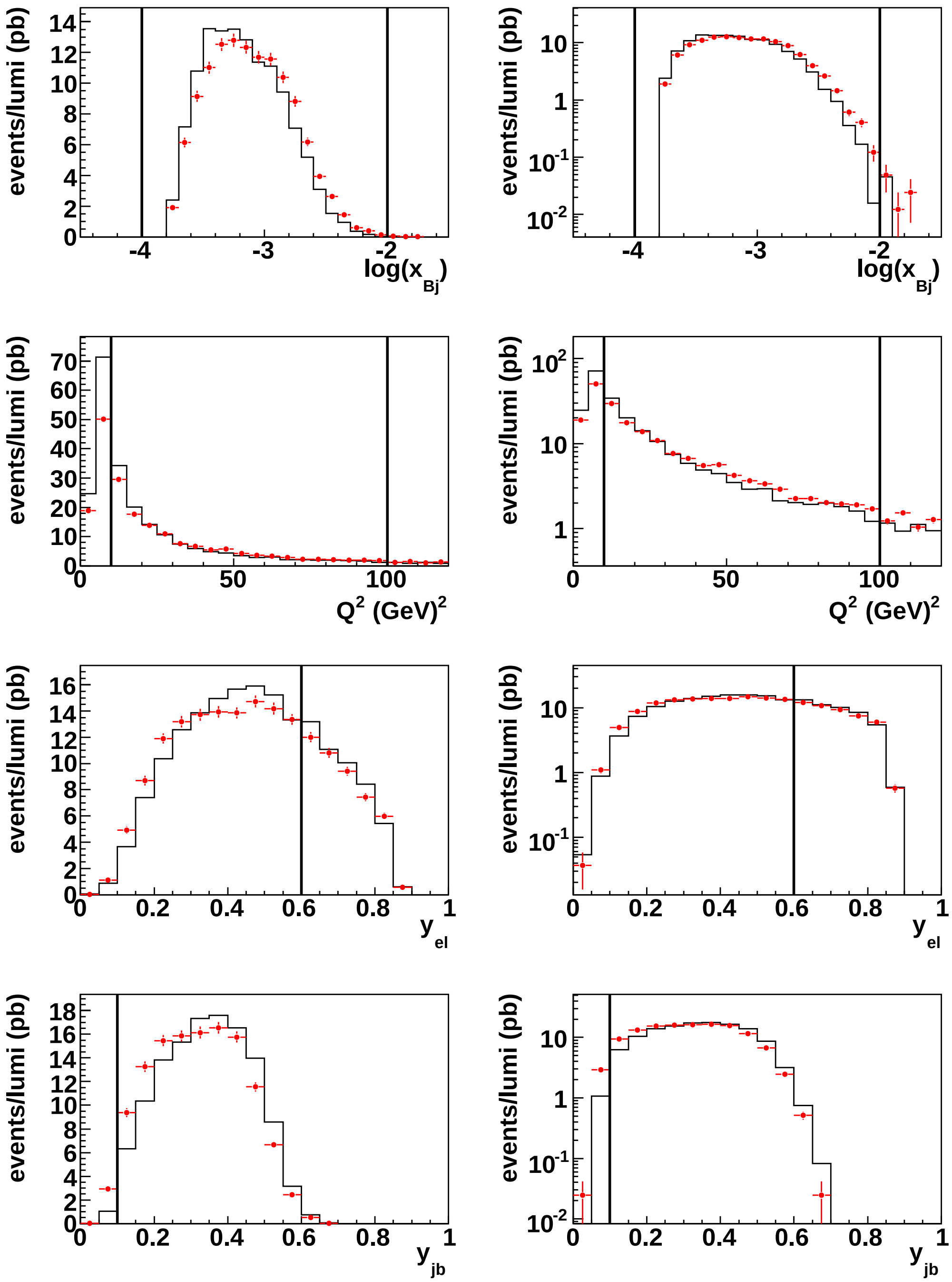

Figure A.5: Data vs. ARIADNE, trijet

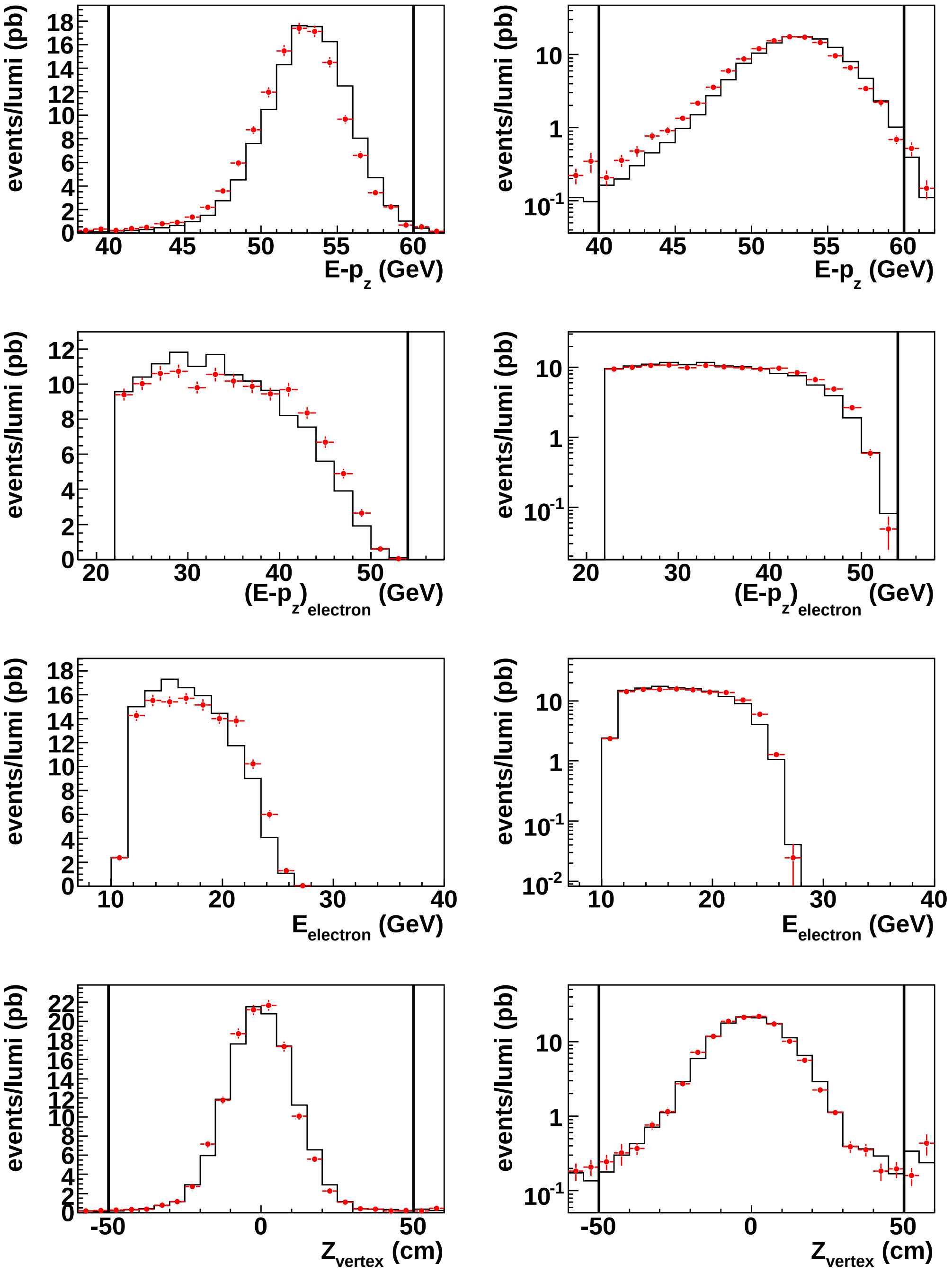

Figure A.6: Data vs. ARIADNE, trijet, continued

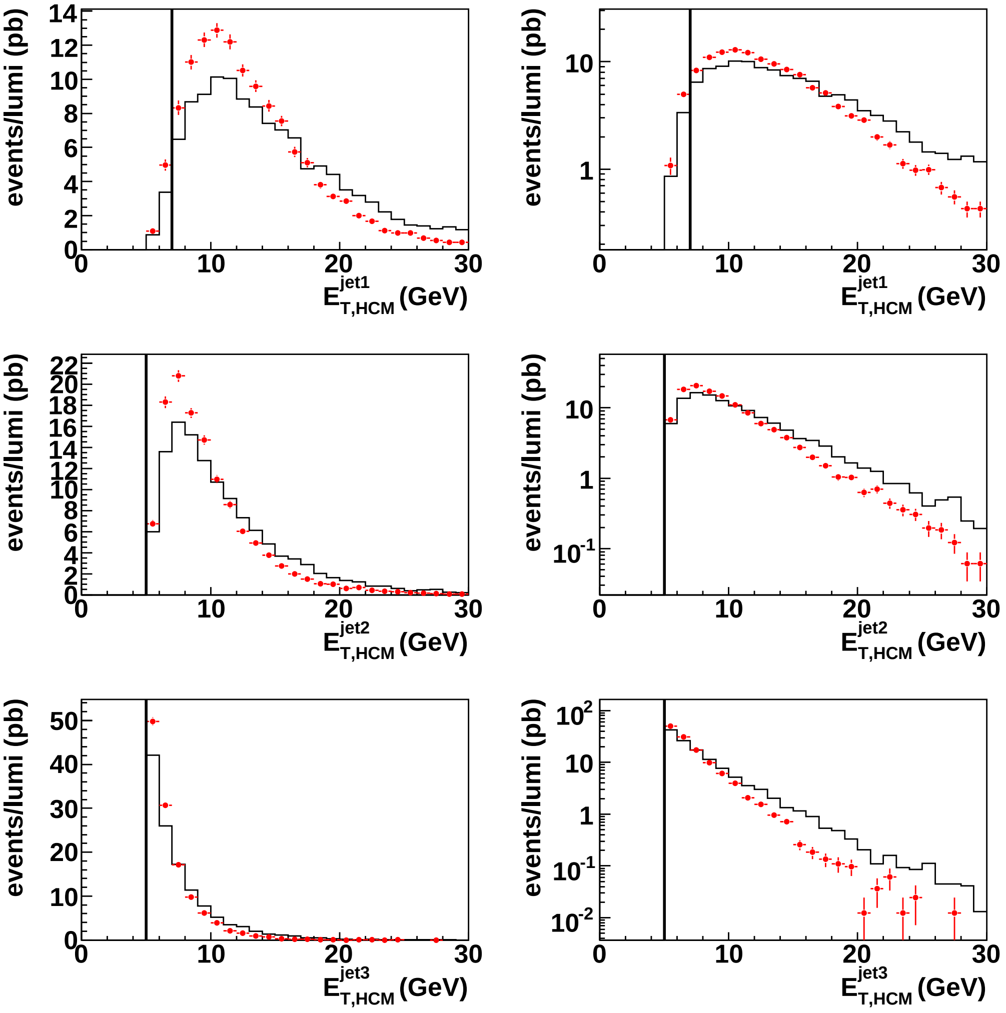

Figure A.7: Data vs. ARIADNE, trijet, jet transverse energies

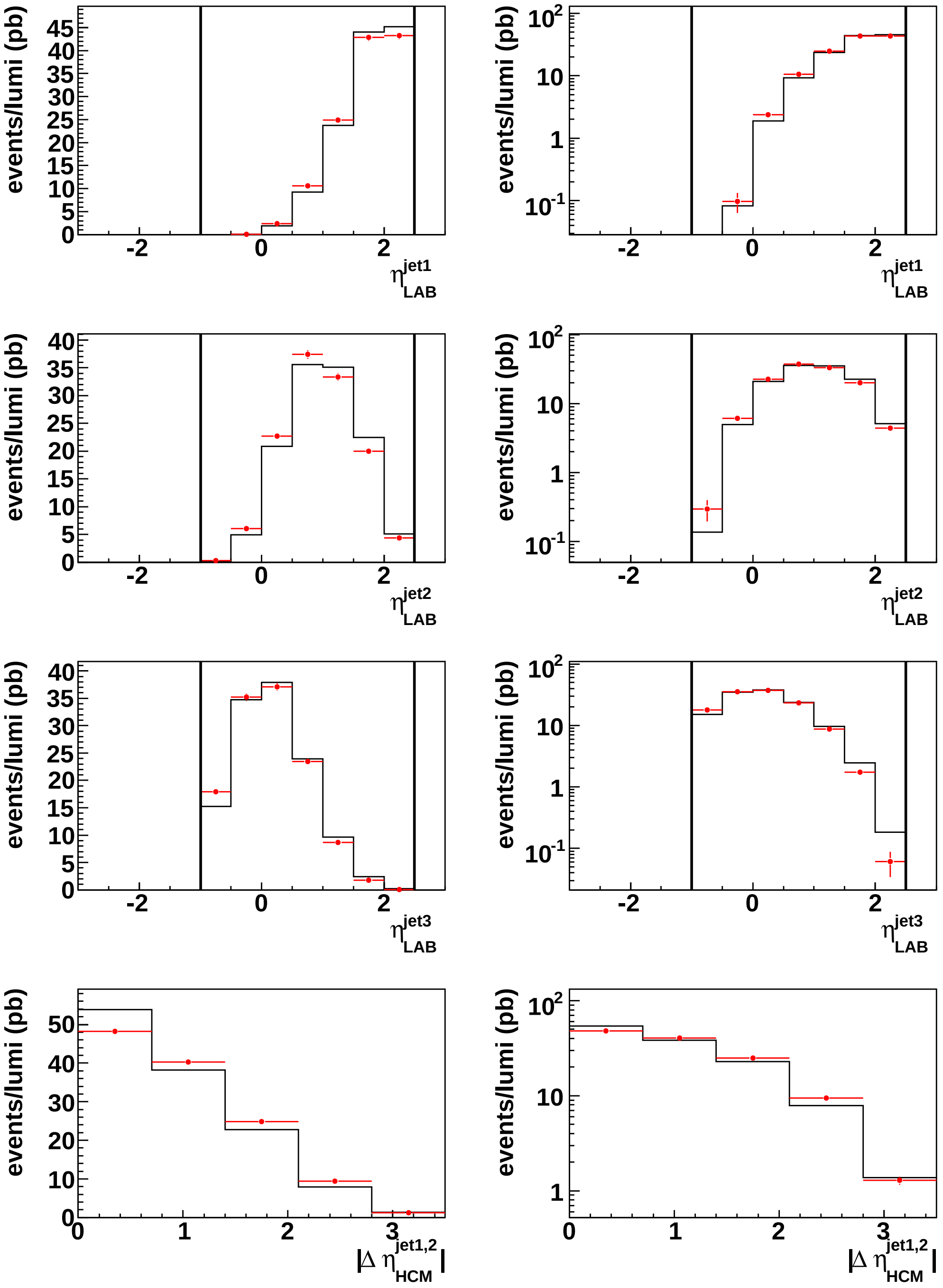

Figure A.8: Data vs. ARIADNE, trijet, jet pseudorapidities

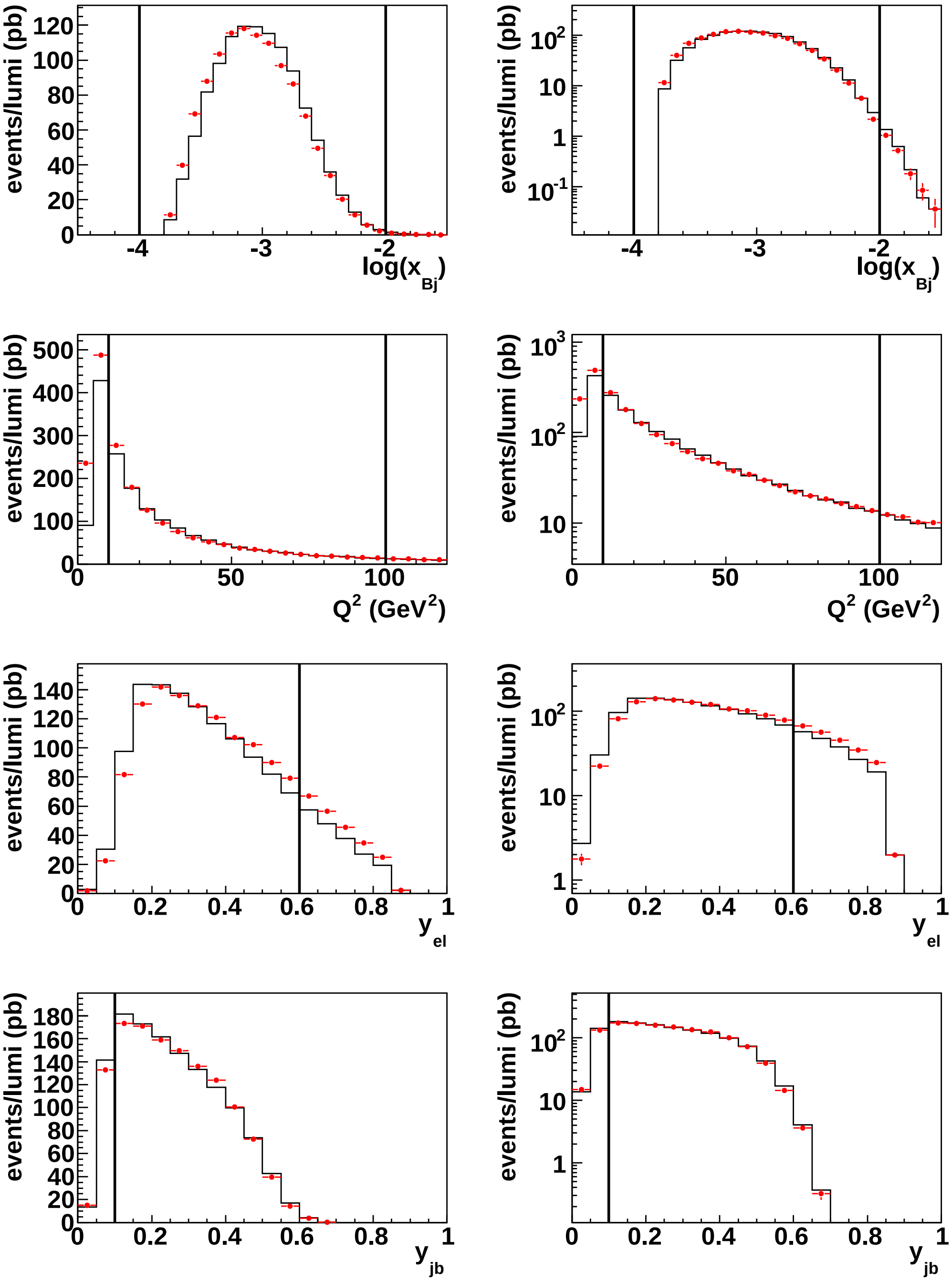

Figure A.9: Data vs. LEPTO, dijet

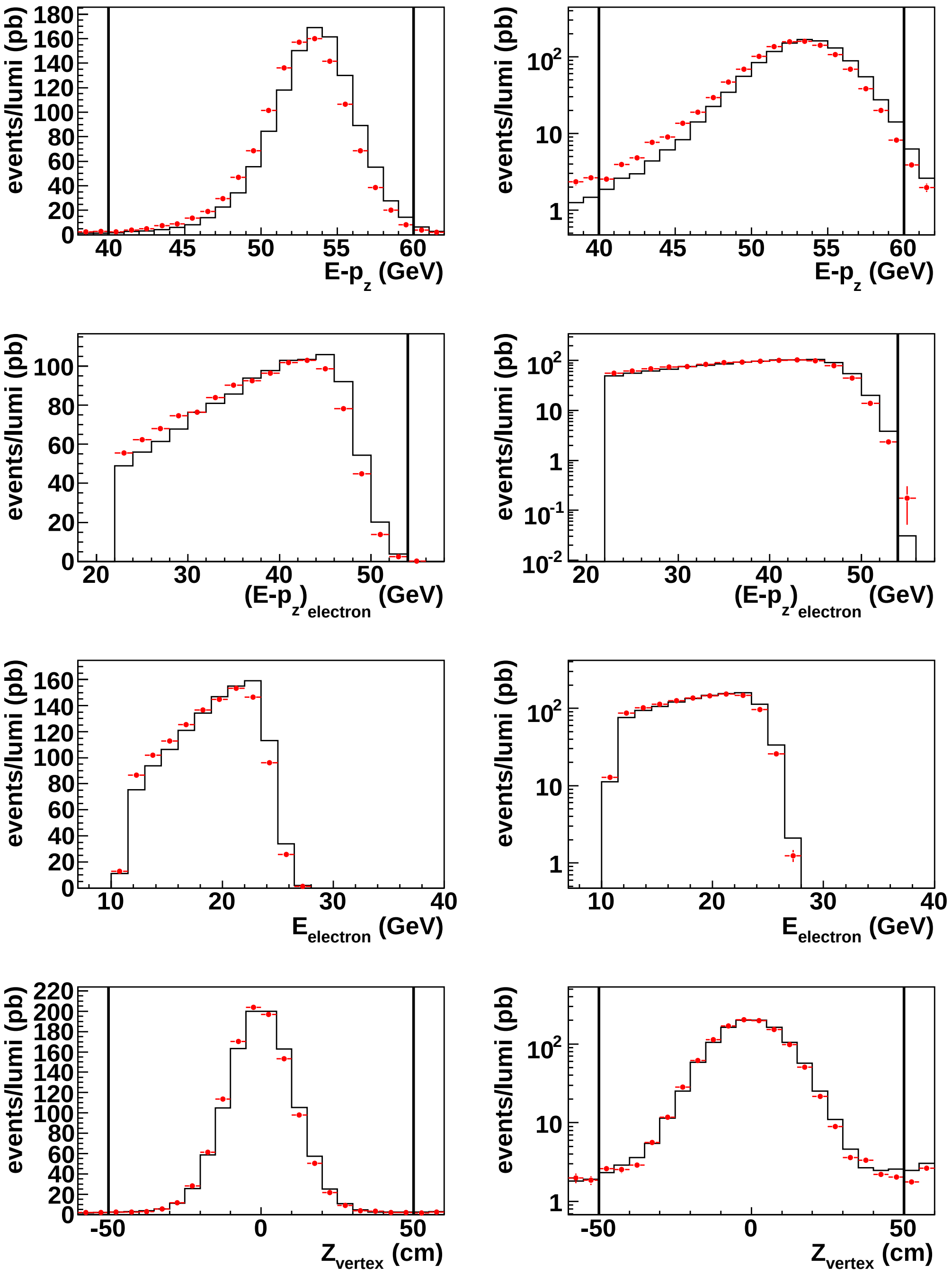

Figure A.10: Data vs. LEPTO, dijet, continued

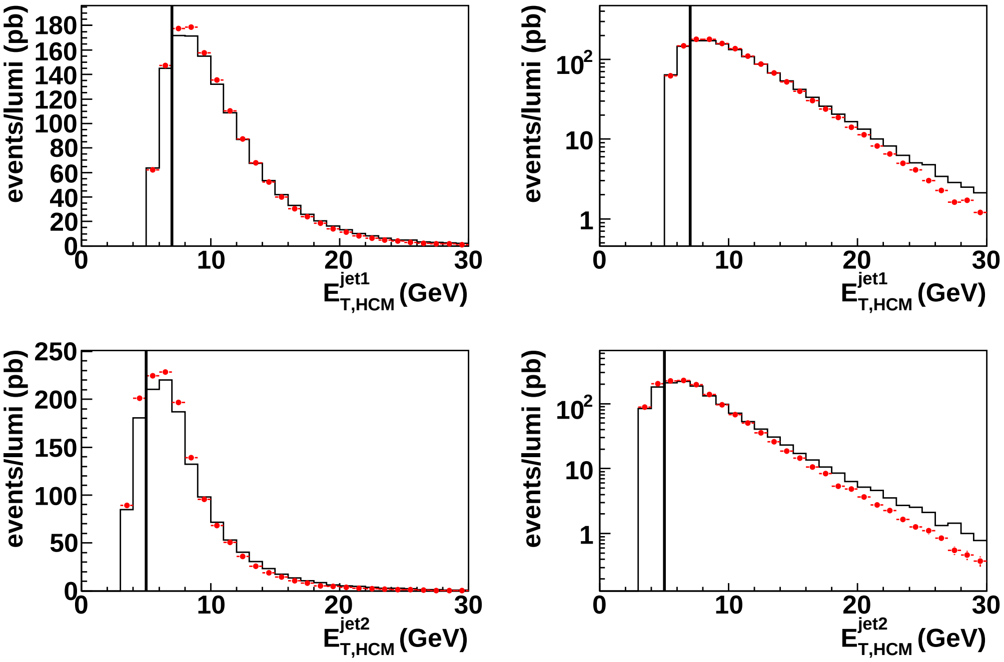

Figure A.11: Data vs. LEPTO, dijet, jet transverse energies

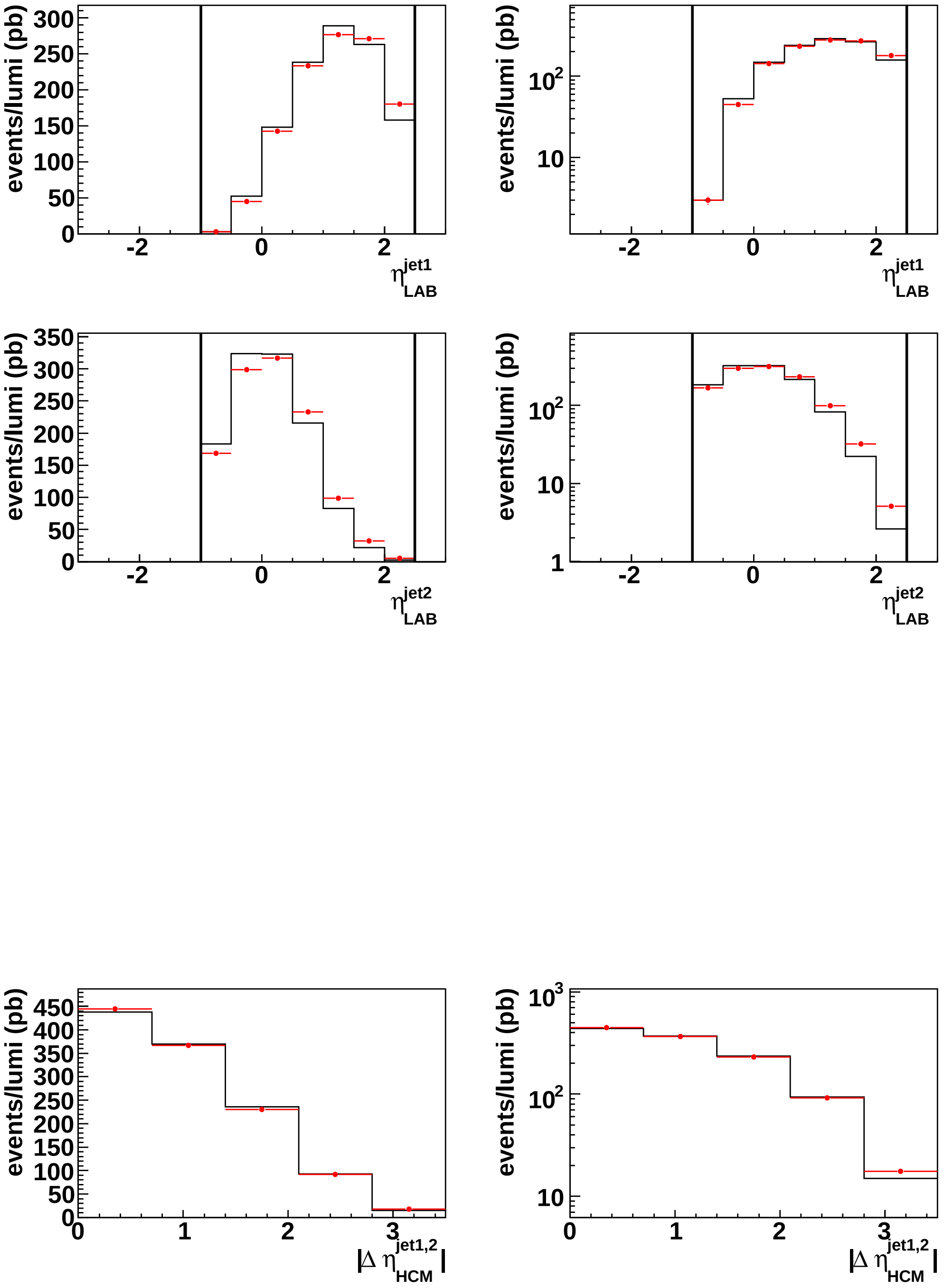

Figure A.12: Data vs. LEPTO, dijet, jet pseudorapidities

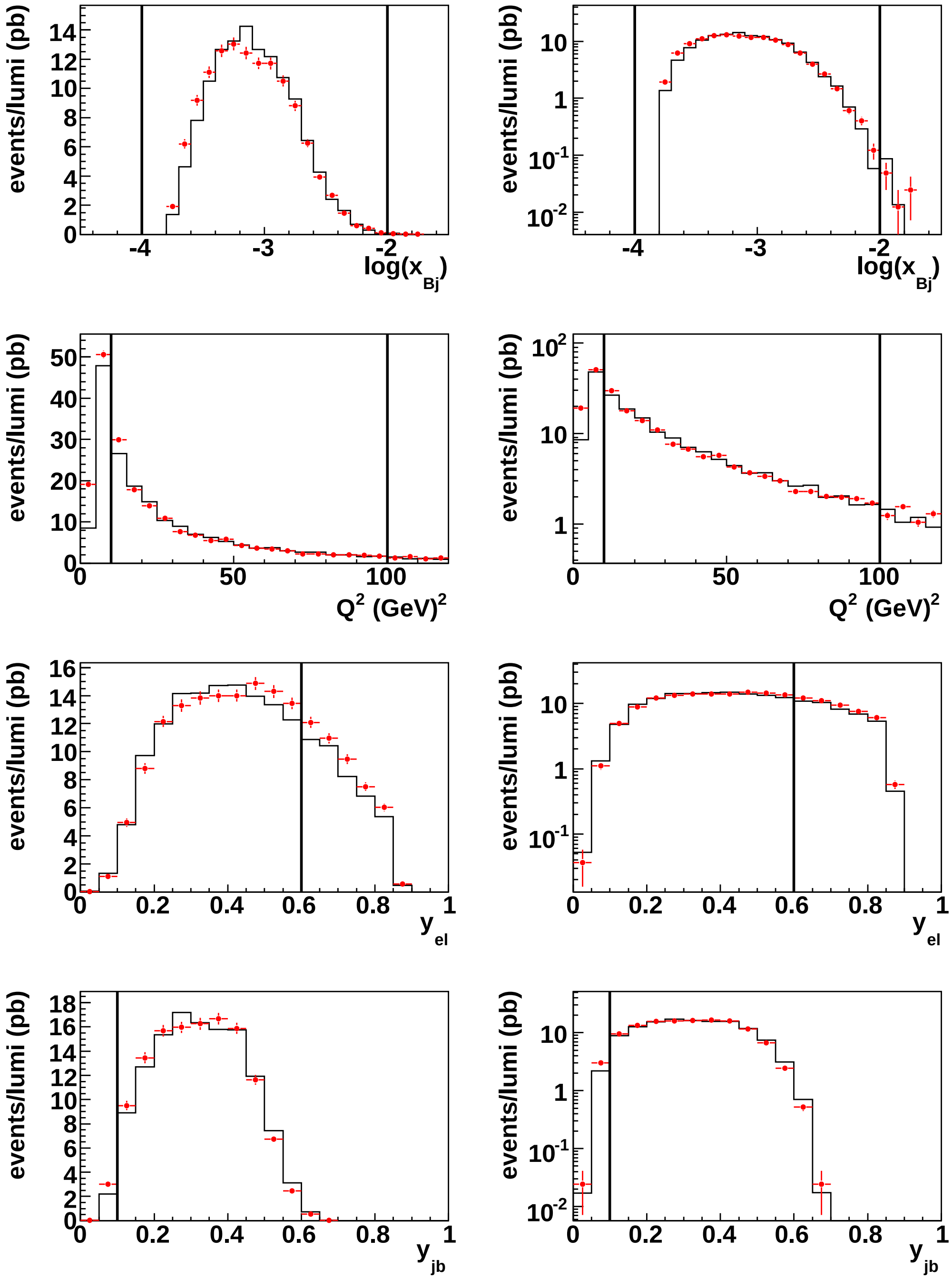

Figure A.13: Data vs. LEPTO, trijet

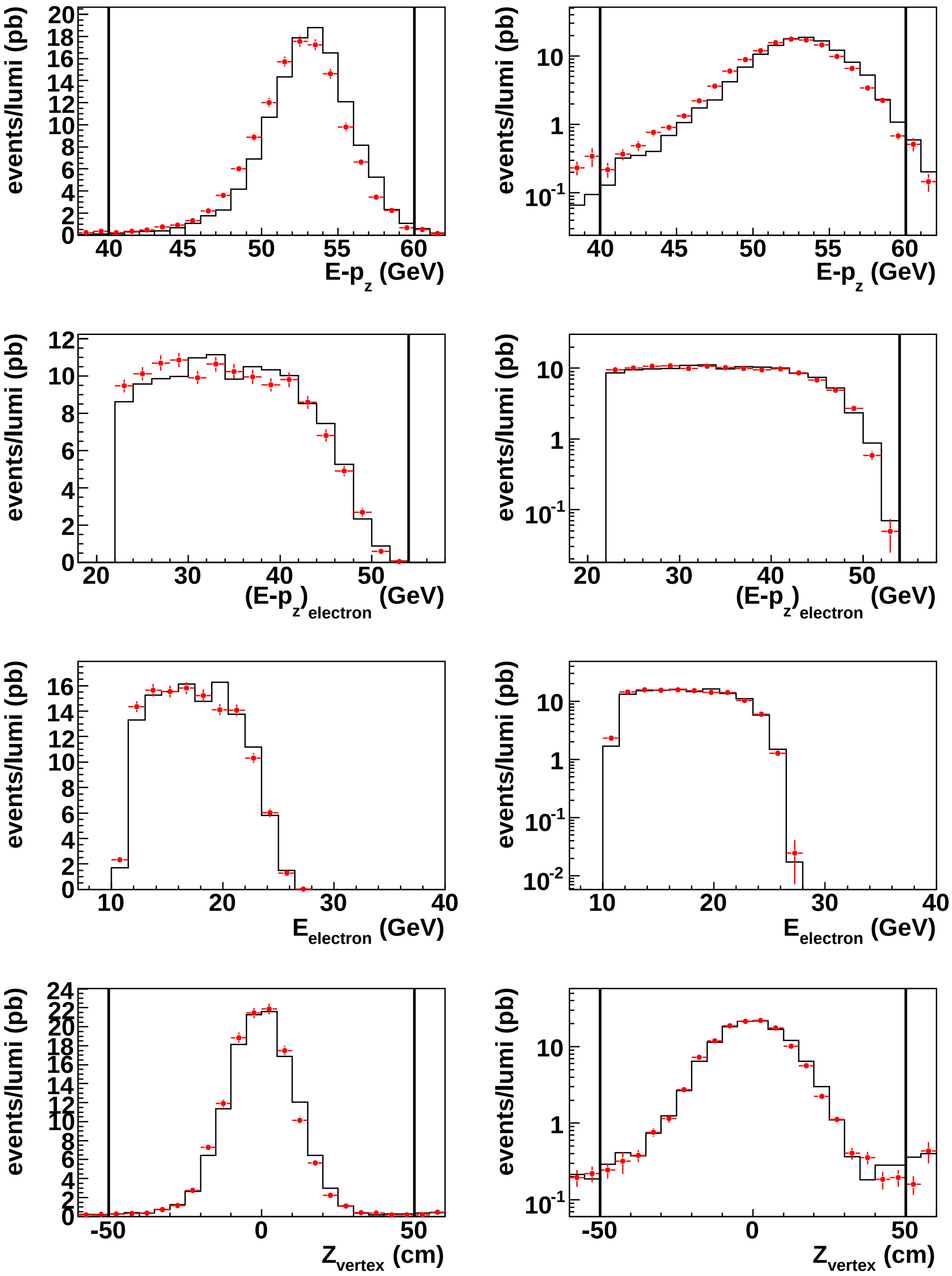

Figure A.14: Data vs. LEPTO, trijet, continued

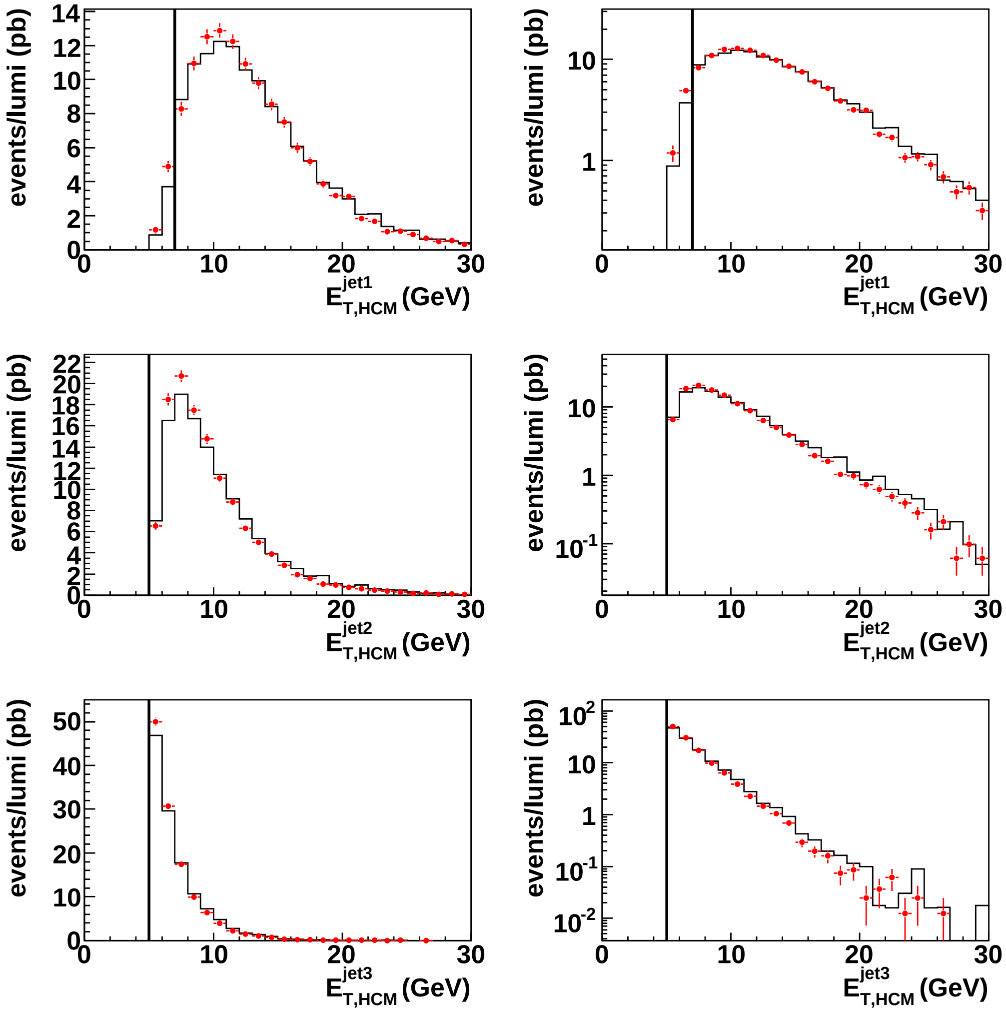

Figure A.15: Data vs. LEPTO, trijet, jet transverse energies

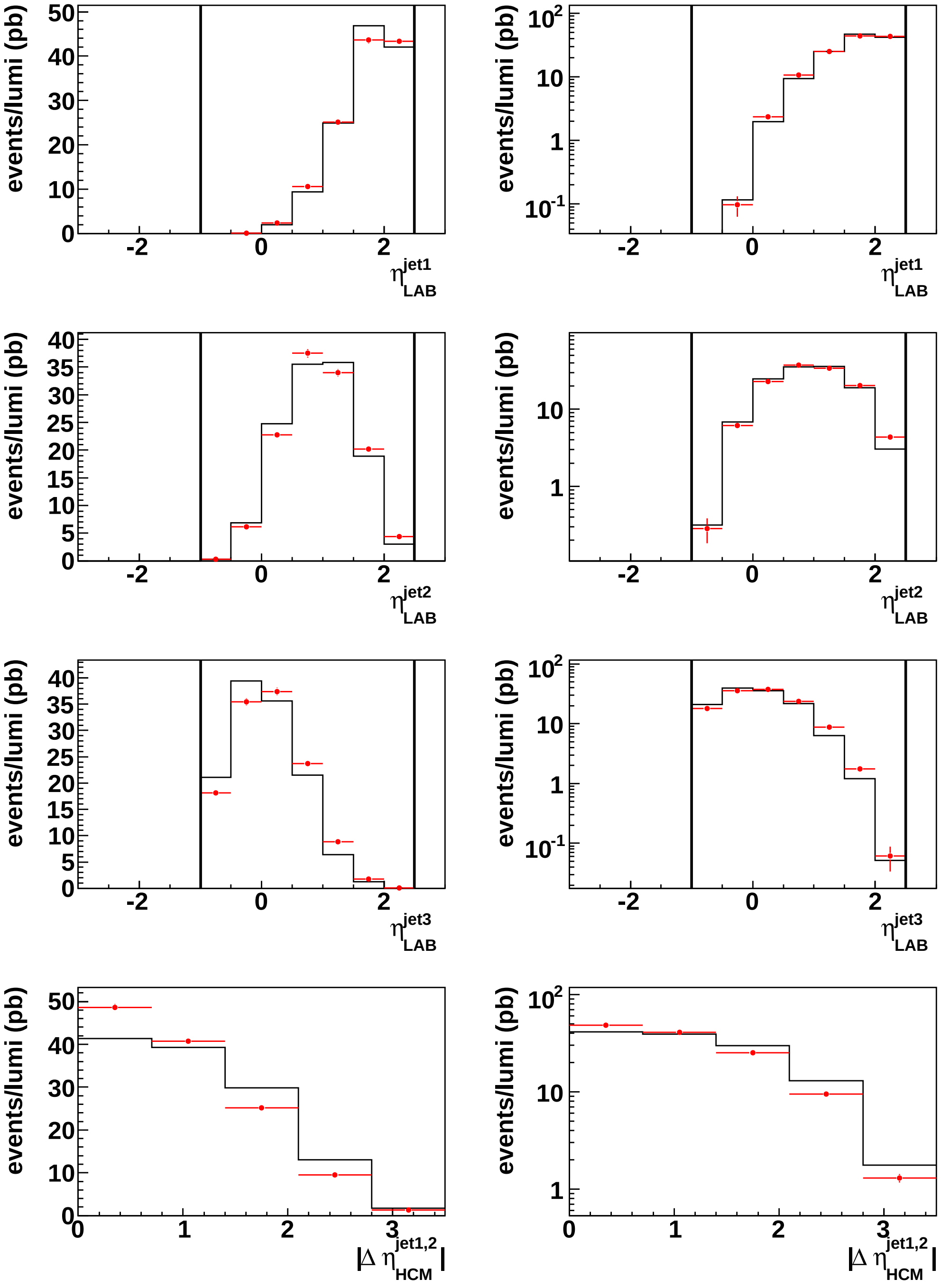

Figure A.16: Data vs. LEPTO, trijet, jet pseudorapidities

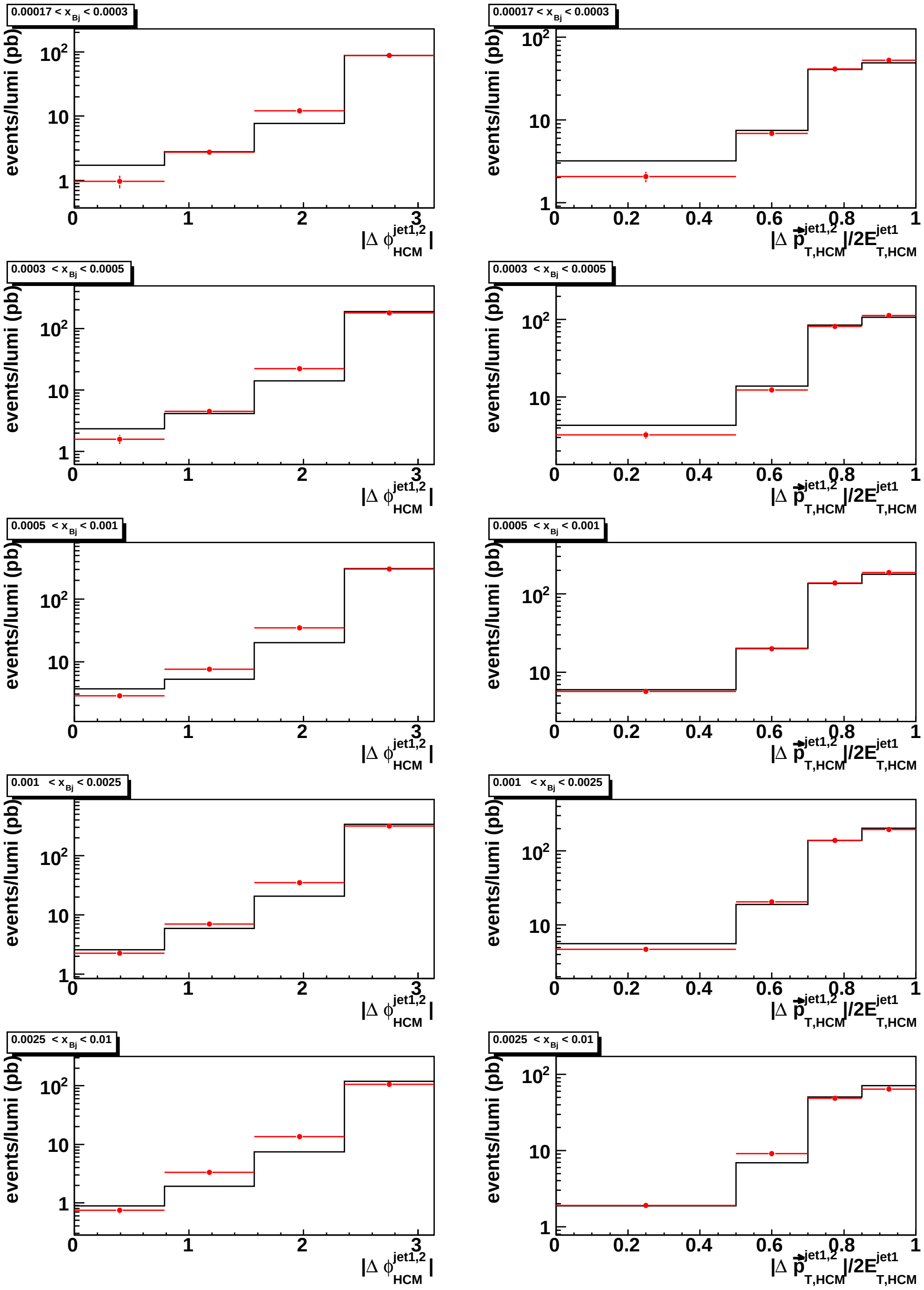

Figure A.17: Comparison of data and ARIADNE, dijet events per integrated luminosity in bins of $|\Delta\phi^{\text{jet1,2}}_{\text{HCM}}|$ and $|\Delta\vec{p}^{\,\text{jet1,2}}_{T,\text{HCM}}|/(2E^{\text{jet1}}_{T,\text{HCM}})$, respectively, in different ranges of x_{Bj}. MC has been normalized to the data

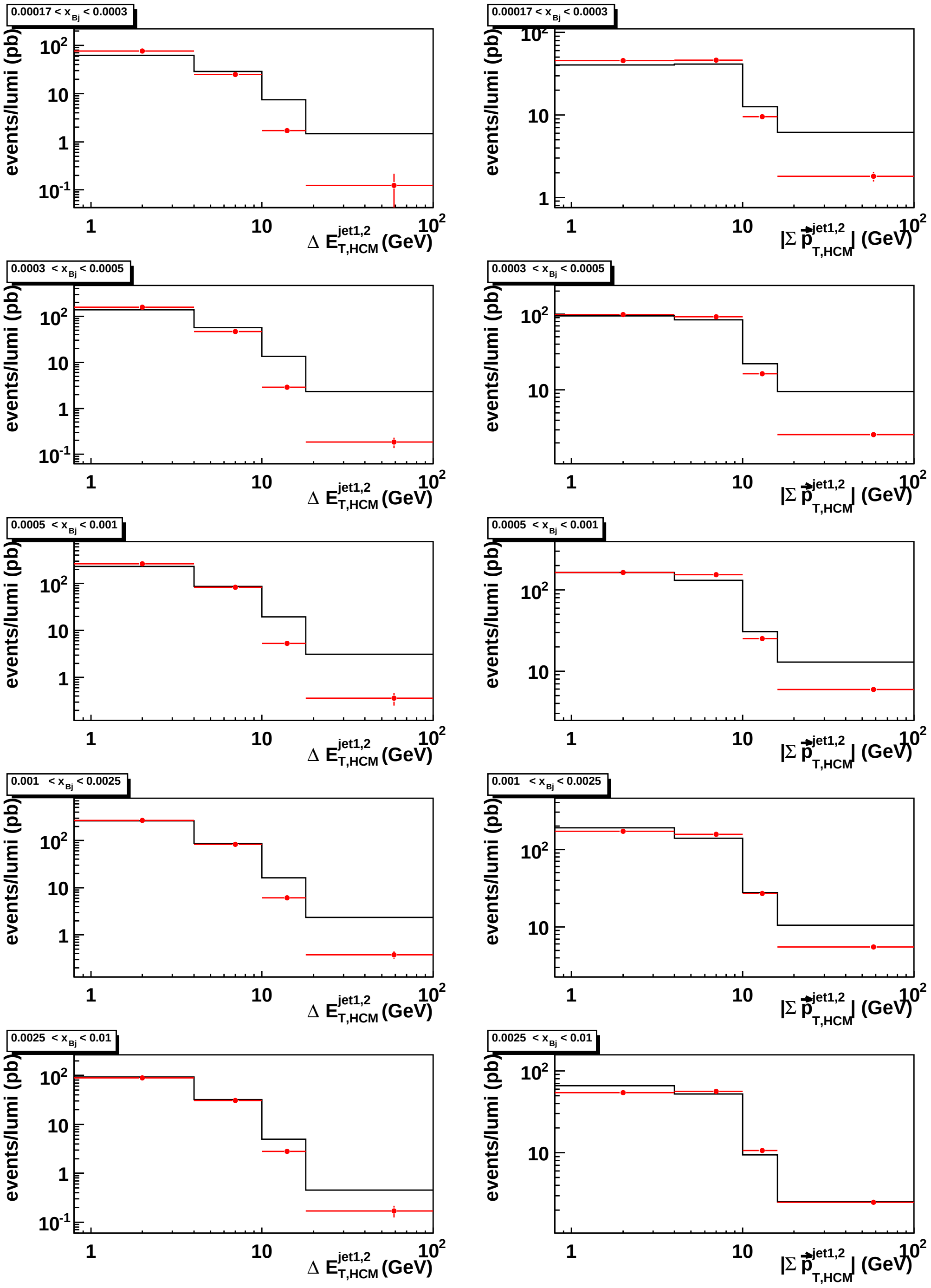

Figure A.18: Comparison of data and ARIADNE, dijet events per integrated luminosity in bins of $\Delta E_{T,\mathrm{HCM}}^{\mathrm{jet1,2}}$ and $|\Sigma\vec{p}_{T,\mathrm{HCM}}^{\,\mathrm{jet1,2}}|$, respectively, in different ranges of x_{Bj}. MC has been normalized to the data

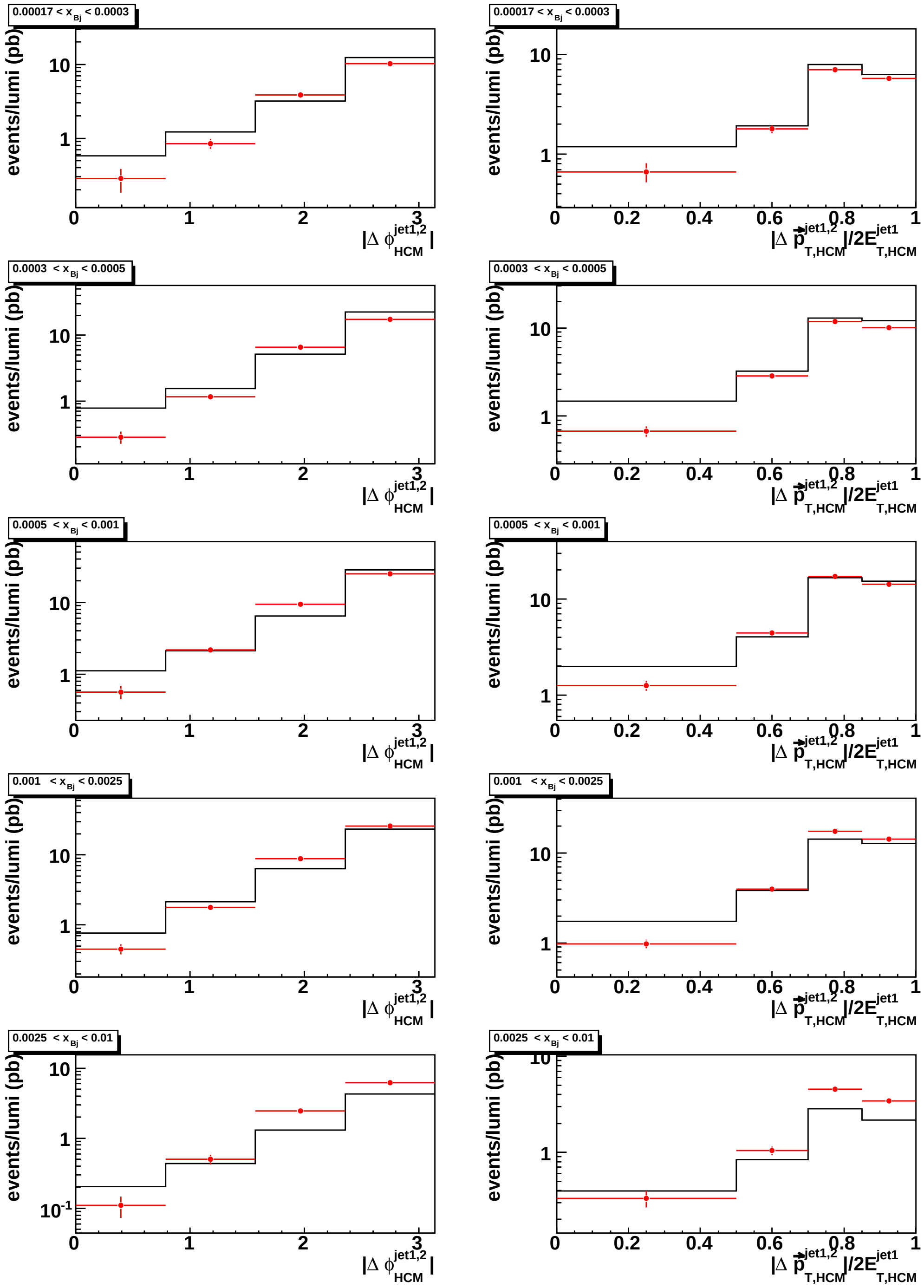

Figure A.19: Comparison of data and ARIADNE, trijet events per integrated luminosity in bins of $|\Delta\phi^{\rm jet1,2}_{\rm HCM}|$ and $|\Delta\vec{p}^{\,\rm jet1,2}_{T,\rm HCM}|/(2E^{\rm jet1}_{T,\rm HCM})$, respectively, in different ranges of $x_{\rm Bj}$. MC has been normalized to the data

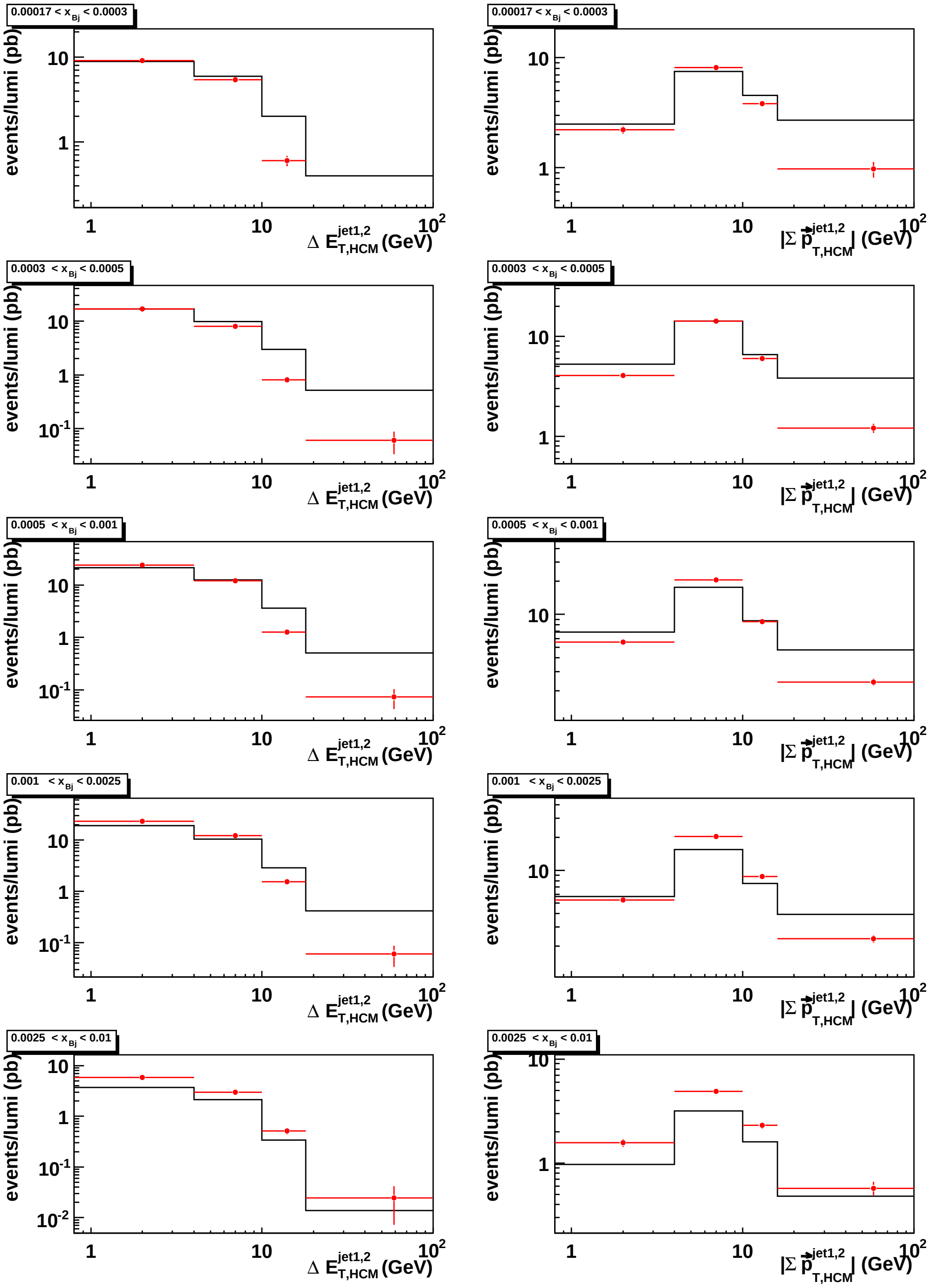

Figure A.20: Comparison of data and ARIADNE, trijet events per integrated luminosity in bins of $\Delta E_{T,\mathrm{HCM}}^{\mathrm{jet1,2}}$ and $|\Sigma\vec{p}_{T,\mathrm{HCM}}^{\mathrm{jet1,2}}|$, respectively, in different ranges of x_{Bj}. MC has been normalized to the data

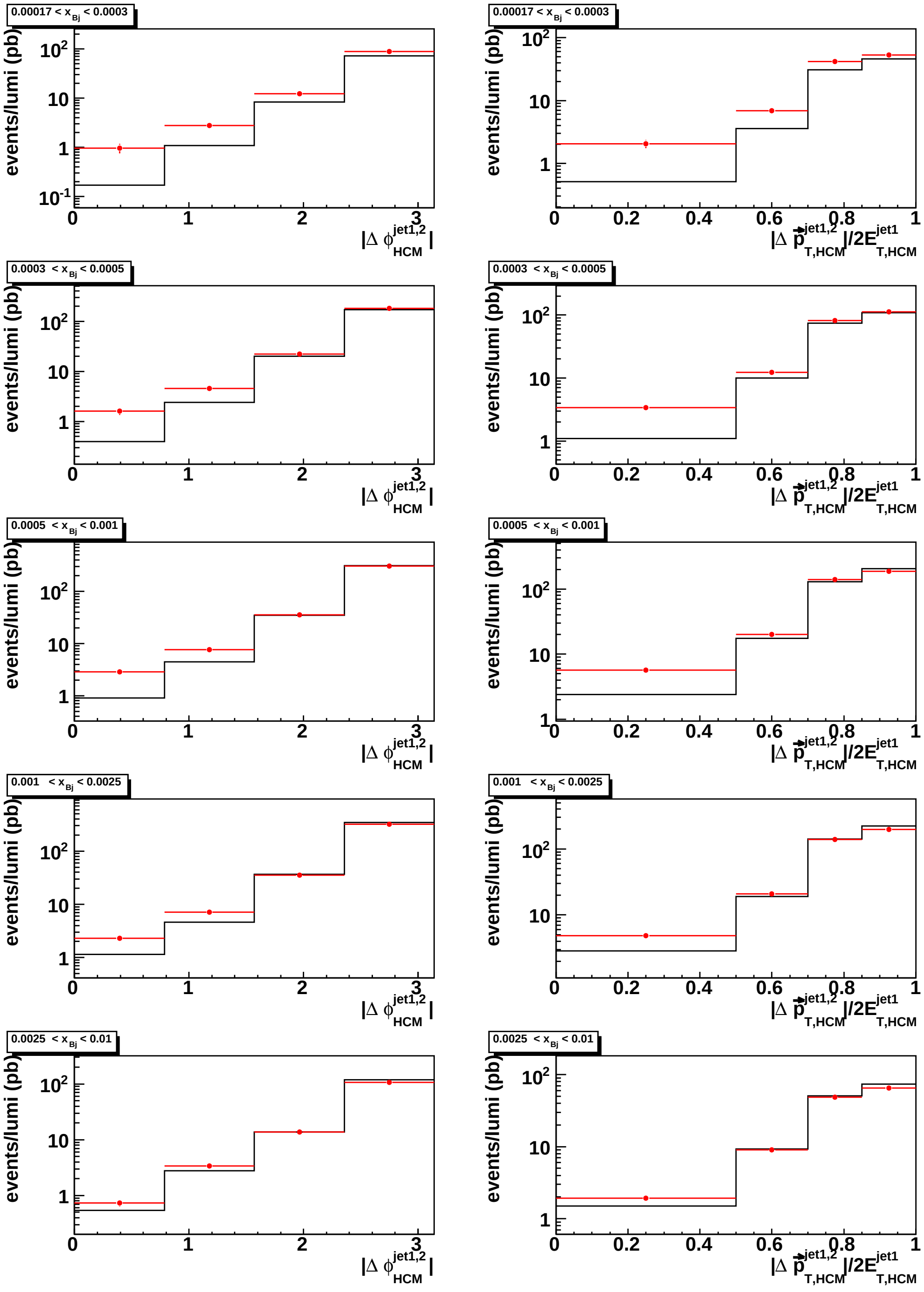

Figure A.21: Comparison of data and LEPTO, dijet events per integrated luminosity in bins of $|\Delta\phi^{\mathrm{jet1,2}}_{\mathrm{HCM}}|$ and $|\Delta\vec{p}^{\,\mathrm{jet1,2}}_{T,\mathrm{HCM}}|/(2E^{\mathrm{jet1}}_{T,\mathrm{HCM}})$, respectively, in different ranges of x_{Bj}. MC has been normalized to the data

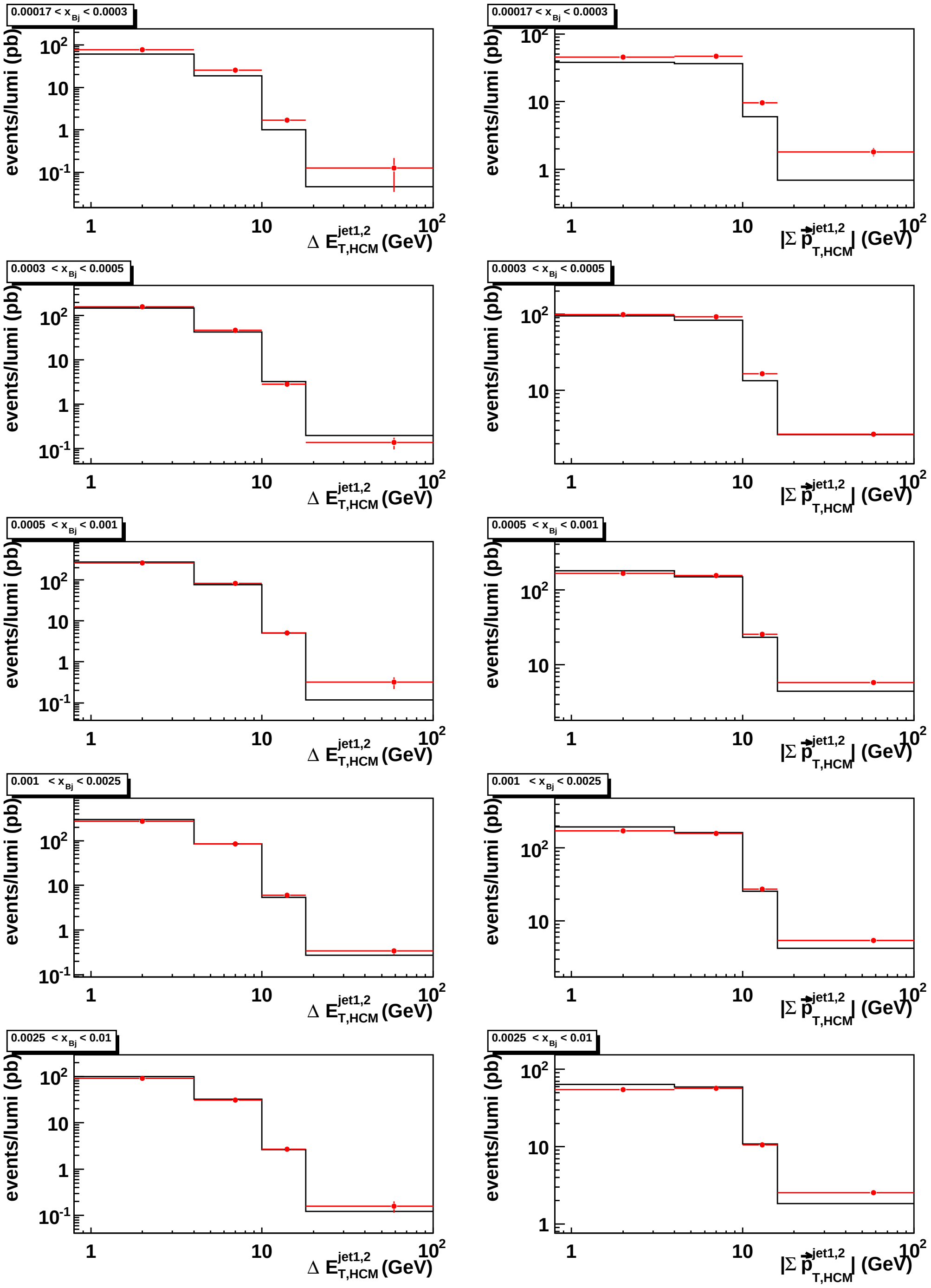

Figure A.22: Comparison of data and LEPTO, dijet events per integrated luminosity in bins of $\Delta E_{T,\mathrm{HCM}}^{\mathrm{jet1,2}}$ and $|\Sigma\vec{p}_{T,\mathrm{HCM}}^{\mathrm{jet1,2}}|$, respectively, in different ranges of x_{Bj}. MC has been normalized to the data

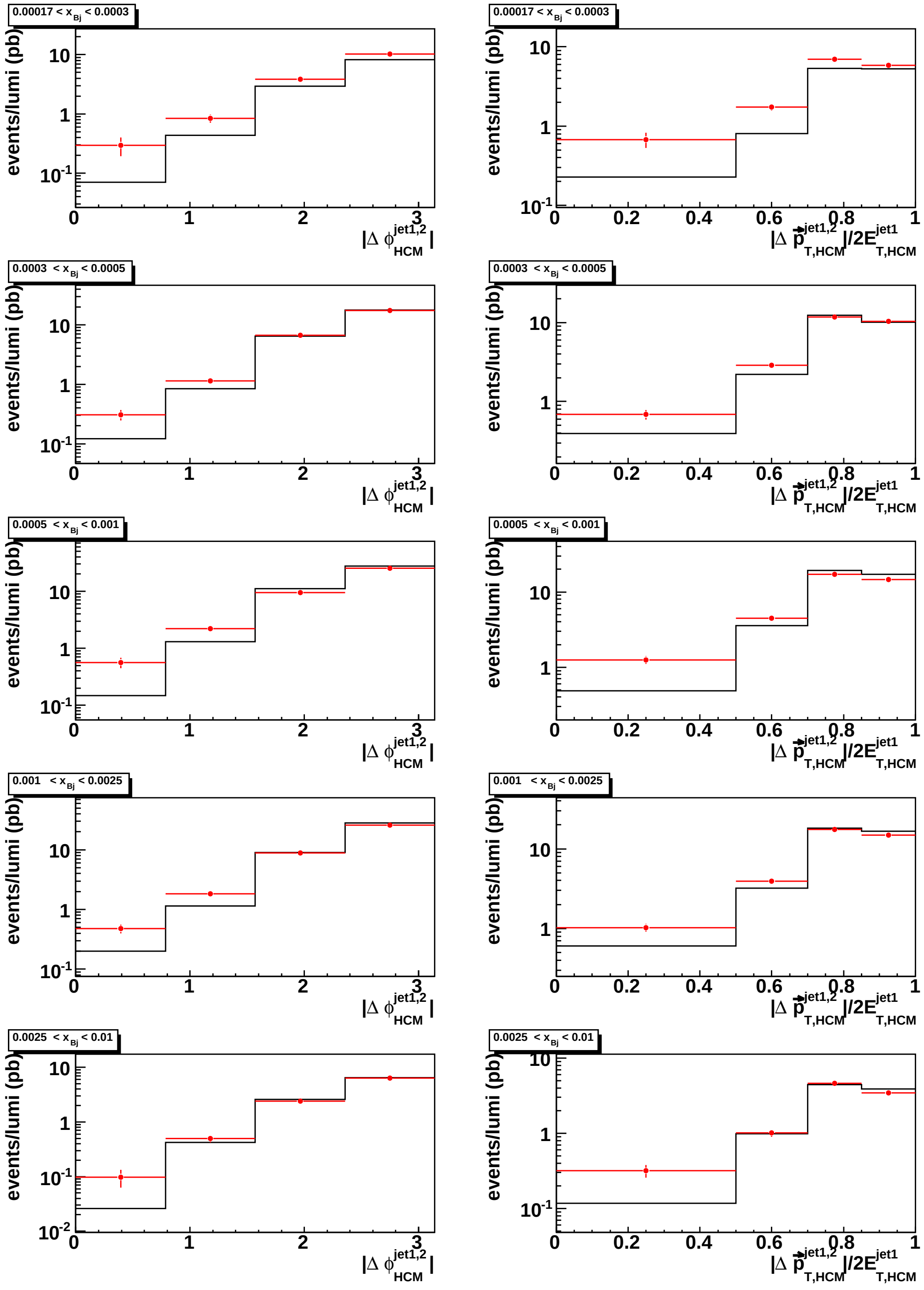

Figure A.23: Comparison of data and LEPTO, trijet events per integrated luminosity in bins of $|\Delta\phi_{\mathrm{HCM}}^{\mathrm{jet1,2}}|$ and $|\Delta\vec{p}_{T,\mathrm{HCM}}^{\mathrm{jet1,2}}|/(2E_{T,\mathrm{HCM}}^{\mathrm{jet1}})$, respectively, in different ranges of x_{Bj}. MC has been normalized to the data

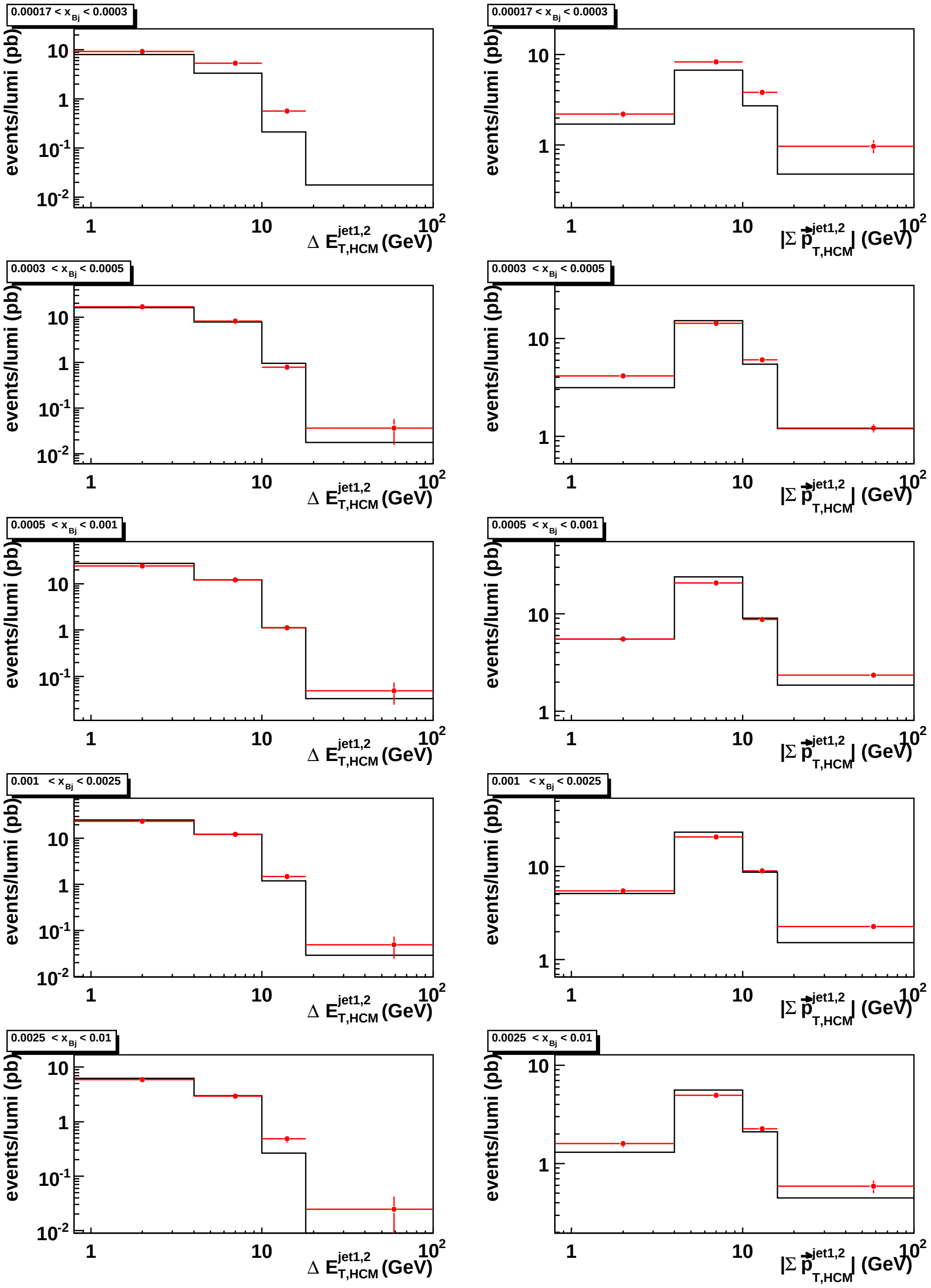

Figure A.24: Comparison of data and LEPTO, trijet events per integrated luminosity in bins of $\Delta E_{T,\mathrm{HCM}}^{\mathrm{jet1,2}}$ and $|\Sigma\vec{p}_{T,\mathrm{HCM}}^{\mathrm{jet1,2}}|$, respectively, in different ranges of x_{Bj}. MC has been normalized to the data

Appendix B

Cross-Section Tables

Q^2	$\frac{d\sigma}{dQ^2}$	δ_{stat}	δ_{syst}	δ_{ES}	C_{QED}	C_{had}
(GeV^2)	(pb/ GeV^2)	(pb/ GeV^2)	(pb/ GeV^2)	(pb/ GeV^2)		
10 - 15	66.0	0.8	$^{+3.7}_{-4.4}$	$^{+5.7}_{-5.9}$	0.984	0.866
15 - 20	41.4	0.6	$^{+2.0}_{-2.4}$	$^{+3.5}_{-3.6}$	0.968	0.870
20 - 30	26.2	0.3	$^{+1.0}_{-0.8}$	$^{+2.2}_{-2.0}$	0.965	0.876
30 - 50	14.0	0.1	$^{+0.4}_{-0.3}$	$^{+1.0}_{-1.1}$	0.955	0.884
50 - 100	5.82	0.06	$^{+0.17}_{-0.16}$	$^{+0.38}_{-0.38}$	0.952	0.887

Table B.1: The inclusive dijet cross sections as functions of Q^2. Included are the statistical, systematic, and jet energy scale uncertainties in columns 3, 4, and 5, respectively. Column 6 shows the correction factor from QED radiative effects applied to the measured cross sections, and column 7 shows the hadronization correction applied to the NLOJET calculations shown in the figures.

$x_{\rm Bj} \times 10^{-4}$	$\frac{d\sigma}{dx_{\rm Bj}}$	δ_{stat}	δ_{syst}	δ_{ES}	C_{QED}	C_{had}
	(pb, $\times 10^{-4}$)	(pb, $\times 10^{-4}$)	(pb, $\times 10^{-4}$)	(pb, $\times 10^{-4}$)		
1.7 - 3.0	85.3	1.7	$^{+5.6}_{-6.8}$	$^{+7.0}_{-6.3}$	0.987	0.910
3.0 - 5.0	113.8	1.5	$^{+5.9}_{-6.2}$	$^{+8.8}_{-8.9}$	0.975	0.887
5.0 - 10.0	83.1	0.8	$^{+3.3}_{-3.7}$	$^{+6.9}_{-7.1}$	0.969	0.876
10.0 - 25.0	29.5	0.3	$^{+0.8}_{-0.8}$	$^{+2.2}_{-2.2}$	0.958	0.876
25.0 - 100.0	2.31	0.03	$^{+0.08}_{-0.07}$	$^{+0.17}_{-0.17}$	0.948	0.862

Table B.2: The inclusive dijet cross sections as functions of $x_{\rm Bj}$. Other details as in the caption to Table 1.

$E_{T,HCM}^{jet,1}$ (GeV)	$\frac{d\sigma}{dE_{T,HCM}^{jet,1}}$ (pb/ GeV)	δ_{stat} (pb/ GeV)	δ_{syst} (pb/ GeV)	δ_{ES} (pb/ GeV)	C_{QED}	C_{had}
5 - 8	109	2	$^{+3}_{-109}$	$^{+5}_{-6}$	0.965	0.814
8 - 12	184	1	$^{+4}_{-3}$	$^{+12}_{-13}$	0.965	0.884
12 - 16	57.4	0.7	$^{+1.0}_{-4.2}$	$^{+6.1}_{-5.8}$	0.963	0.924
16 - 20	18.3	0.3	$^{+0.4}_{-0.8}$	$^{+2.1}_{-1.8}$	0.956	0.936
20 - 25	6.27	0.16	$^{+0.22}_{-0.86}$	$^{+0.74}_{-0.75}$	0.965	0.939
25 - 30	1.72	0.08	$^{+0.06}_{-0.07}$	$^{+0.29}_{-0.25}$	0.96	0.930
30 - 40	0.415	0.026	$^{+0.016}_{-0.035}$	$^{+0.082}_{-0.057}$	0.96	0.93
40 - 60	0.043	0.006	$^{+0.008}_{-0.011}$	$^{+0.007}_{-0.010}$	1.01	0.93

Table B.3: The inclusive dijet cross sections as functions of $E_{T,HCM}^{jet,1}$. Other details as in the caption to Table 1.

$E_{T,HCM}^{jet,2}$ (GeV)	$\frac{d\sigma}{dE_{T,HCM}^{jet,2}}$ (pb/ GeV)	δ_{stat} (pb/ GeV)	δ_{syst} (pb/ GeV)	δ_{ES} (pb/ GeV)	C_{QED}	C_{had}
5 - 8	278	2	$^{+6}_{-8}$	$^{+19}_{-19}$	0.964	0.864
8 - 12	104.5	0.9	$^{+0.8}_{-1.6}$	$^{+8.6}_{-9.0}$	0.965	0.879
12 - 16	23.3	0.4	$^{+0.4}_{-0.3}$	$^{+2.6}_{-2.5}$	0.965	0.926
16 - 20	6.59	0.19	$^{+0.71}_{-0.20}$	$^{+0.83}_{-0.64}$	0.958	0.953
20 - 25	2.12	0.09	$^{+0.21}_{-0.08}$	$^{+0.30}_{-0.30}$	0.97	0.937
25 - 30	0.64	0.05	$^{+0.12}_{-0.02}$	$^{+0.13}_{-0.05}$	0.93	0.97
30 - 40	0.171	0.017	$^{+0.014}_{-0.019}$	$^{+0.020}_{-0.027}$	0.97	0.95
40 - 60	0.0110	0.0037	$^{+0.0034}_{-0.0038}$	$^{+0.0033}_{-0.0022}$	1.07	0.93

Table B.4: The inclusive dijet cross sections as functions of $E_{T,HCM}^{jet,2}$. Other details as in the caption to Table 1.

$\eta_{LAB}^{jet,1}$	$\frac{d\sigma}{d\eta_{LAB}^{jet,1}}$ (pb)	δ_{stat} (pb)	δ_{syst} (pb)	δ_{ES} (pb)	C_{QED}	C_{had}
-1.0 - -0.5	6.0	0.9	$^{+2.5}_{-1.1}$	$^{+1.4}_{-1.0}$	0.94	0.424
-0.5 - 0.0	115	3	$^{+7}_{-2}$	$^{+17}_{-15}$	0.977	0.742
0.0 - 0.5	337	5	$^{+9}_{-11}$	$^{+31}_{-31}$	0.968	0.855
0.5 - 1.0	543	7	$^{+22}_{-20}$	$^{+45}_{-45}$	0.964	0.885
1.0 - 1.5	630	7	$^{+28}_{-25}$	$^{+43}_{-48}$	0.963	0.910
1.5 - 2.0	599	7	$^{+21}_{-29}$	$^{+40}_{-43}$	0.959	0.915
2.0 - 2.5	521	7	$^{+33}_{-36}$	$^{+38}_{-33}$	0.967	0.849

Table B.5: The inclusive dijet cross sections as functions of $\eta_{LAB}^{jet,1}$. Other details as in the caption to Table 1.

$\eta_{LAB}^{jet,2}$	$\frac{d\sigma}{d\eta_{LAB}^{jet,2}}$ (pb)	δ_{stat} (pb)	δ_{syst} (pb)	δ_{ES} (pb)	C_{QED}	C_{had}
-1.0 - -0.5	455	7	$^{+15}_{-26}$	$^{+51}_{-47}$	0.968	0.767
-0.5 - 0.0	703	7	$^{+26}_{-28}$	$^{+61}_{-64}$	0.968	0.873
0.0 - 0.5	709	7	$^{+31}_{-29}$	$^{+53}_{-54}$	0.963	0.899
0.5 - 1.0	542	6	$^{+20}_{-27}$	$^{+33}_{-36}$	0.960	0.933
1.0 - 1.5	234	4	$^{+14}_{-10}$	$^{+13}_{-11}$	0.960	0.992
1.5 - 2.0	74.0	2.3	$^{+5.3}_{-6.0}$	$^{+3.8}_{-4.4}$	0.954	0.910
2.0 - 2.5	15.9	1.3	$^{+1.4}_{-3.8}$	$^{+0.9}_{-0.6}$	0.94	0.87

Table B.6: The inclusive dijet cross sections as functions of $\eta_{LAB}^{jet,2}$. Other details as in the caption to Table 1.

$\Delta\eta_{HCM}^{\rm jet1,2}$	$\frac{d\sigma}{d\Delta\eta_{HCM}^{\rm jet1,2}}$ (pb)	δ_{stat} (pb)	δ_{syst} (pb)	δ_{ES} (pb)	C_{QED}	C_{had}
0.0 - 0.7	744	6	$^{+25}_{-25}$	$^{+55}_{-57}$	0.964	0.890
0.7 - 1.4	617	6	$^{+20}_{-21}$	$^{+47}_{-47}$	0.962	0.905
1.4 - 2.1	390	5	$^{+26}_{-20}$	$^{+31}_{-31}$	0.966	0.878
2.1 - 2.8	169	3	$^{+9}_{-13}$	$^{+16}_{-16}$	0.966	0.793
2.8 - 3.5	37.5	1.8	$^{+3.1}_{-5.3}$	$^{+4.8}_{-4.6}$	0.977	0.623

Table B.7: The inclusive dijet cross sections as functions of $\Delta\eta_{HCM}^{\rm jet1,2}$. Other details as in the caption to Table 1.

$x_{\rm Bj} \times 10^4$	$\Delta E^{\rm jet1,2}_{T,HCM}$ (GeV)	$\frac{d^2\sigma}{d\left(\Delta E^{\rm jet1,2}_{T,HCM}\right)dx_{\rm Bj}}$ (pb/ GeV)	δ_{stat} (pb/ GeV)	δ_{syst} (pb/ GeV)	δ_{ES} (pb/ GeV)	C_{QED}	C_{had}
1.7 - 3.0	0.0 - 4.0	1.75×10^5	4.3×10^3	${}^{+1.1\times10^4}_{-1.2\times10^4}$	${}^{+1.3\times10^4}_{-1.1\times10^4}$	0.984	0.908
	4.0 - 10.0	2.76×10^4	1.2×10^3	${}^{+4.0\times10^3}_{-8.7\times10^3}$	${}^{+2.9\times10^3}_{-2.8\times10^3}$	1.00	0.920
	10.0 - 18.0	1.51×10^3	2.1×10^2	${}^{+6.3\times10^2}_{-3.2\times10^2}$	${}^{+3.7\times10^2}_{-1.7\times10^2}$	1.04	0.89
3.0 - 5.0	0.0 - 4.0	2.37×10^5	3.9×10^3	${}^{+1.3\times10^4}_{-7.1\times10^3}$	${}^{+1.6\times10^4}_{-1.7\times10^4}$	0.975	0.883
	4.0 - 10.0	3.4×10^4	1.0×10^3	${}^{+3.9\times10^3}_{-1.0\times10^4}$	${}^{+3.8\times10^3}_{-3.4\times10^3}$	0.976	0.918
	10.0 - 18.0	1.55×10^3	1.5×10^2	${}^{+3.4\times10^2}_{-5.6\times10^2}$	${}^{+1.8\times10^2}_{-2.1\times10^2}$	0.97	0.88
	18.0 - 100.0	17.9	5.3	${}^{+4.9}_{-5.6}$	${}^{+1.2}_{-2.4}$	1.1	0.81
5.0 - 10	0.0 - 4.0	1.73×10^5	2.1×10^3	${}^{+3.9\times10^3}_{-4.8\times10^3}$	${}^{+1.3\times10^4}_{-1.4\times10^4}$	0.970	0.872
	4.0 - 10.0	2.46×10^4	5.8×10^2	${}^{+2.4\times10^3}_{-7.1\times10^3}$	${}^{+2.7\times10^3}_{-2.6\times10^3}$	0.964	0.905
	10.0 - 18.0	1.20×10^3	8.2×10^1	${}^{+2.7\times10^2}_{-2.8\times10^2}$	${}^{+2.1\times10^2}_{-1.3\times10^2}$	0.99	0.86
	18.0 - 100.0	10.6	3.4	${}^{+4.6}_{-3.6}$	${}^{+0.7}_{-1.1}$	0.96	0.80
10 - 25	0.0 - 4.0	6.24×10^4	6.8×10^2	${}^{+1.9\times10^3}_{-1.7\times10^3}$	${}^{+4.1\times10^3}_{-4.3\times10^3}$	0.959	0.874
	4.0 - 10.0	7.7×10^3	1.7×10^2	${}^{+3.4\times10^2}_{-1.9\times10^3}$	${}^{+7.5\times10^2}_{-7.2\times10^2}$	0.959	0.896
	10.0 - 18.0	428	27	${}^{+95}_{-152}$	${}^{+92}_{-44}$	0.94	0.82
	18.0 - 100.0	3.9	0.9	${}^{+1.3}_{-0.6}$	${}^{+1.1}_{-0.9}$	1.00	0.78
25 - 100	0.0 - 4.0	5.08×10^3	9.1×10^1	${}^{+1.5\times10^2}_{-1.4\times10^2}$	${}^{+3.2\times10^2}_{-3.2\times10^2}$	0.949	0.860
	4.0 - 10.0	457	18	${}^{+20}_{-96}$	${}^{+40}_{-46}$	0.941	0.885
	10.0 - 18.0	34	4	${}^{+9}_{-15}$	${}^{+5}_{-7}$	1.05	0.78
	18.0 - 100.0	0.24	0.09	${}^{+0.11}_{-0.11}$	${}^{+0.02}_{-0.02}$	0.7	1.0

Table B.8: The dijet double-differential cross sections as functions of $\Delta E^{jet1,2}_{T,HCM}$. Included are the statistical, systematic, and jet energy scale uncertainties in columns 4, 5, and 6, respectively. Column 7 shows the correction factor from QED radiative effects applied to the measured cross sections, and column 8 shows the hadronization correction applied to the NLOJET calculations shown in the figures.

Table B.9: The dijet double-differential cross sections as functions of $|\Sigma\vec{p}_{T,HCM}^{\,\rm jet1,2}|$. Other details as in the caption to Table 5.

$x_{\rm Bj} \times 10^4$	$\|\Sigma\vec{p}_{T,HCM}^{\,\rm jet1,2}\|$ (GeV)	$\frac{d^2\sigma}{d(\|\Sigma\vec{p}_{T,HCM}^{\,\rm jet1,2}\|)dx_{\rm Bj}}$ (pb/ GeV)	δ_{stat} (pb/ GeV)	δ_{syst} (pb/ GeV)	δ_{ES} (pb/ GeV)	C_{QED}	C_{had}
1.7 - 3.0	0.0 - 4.0	1.145×10^5	3.7×10^3	$^{+8.3\times10^3}_{-8.1\times10^3}$	$^{+6.0\times10^3}_{-5.6\times10^3}$	0.978	0.934
	4.0 - 10.0	5.47×10^4	1.8×10^3	$^{+3.5\times10^3}_{-6.0\times10^3}$	$^{+5.4\times10^3}_{-4.8\times10^3}$	0.995	0.878
	10.0 - 16.0	1.10×10^4	7.5×10^2	$^{+1.2\times10^3}_{-2.1\times10^3}$	$^{+1.1\times10^3}_{-1.2\times10^3}$	1.02	0.88
	16.0 - 100.0	164	25	$^{+36}_{-19}$	$^{+53}_{-23}$	1.02	0.85
3.0 - 5.0	0.0 - 4.0	1.597×10^5	3.4×10^3	$^{+6.9\times10^3}_{-4.9\times10^3}$	$^{+8.2\times10^3}_{-7.9\times10^3}$	0.973	0.898
	4.0 - 10.0	7.02×10^4	1.6×10^3	$^{+4.8\times10^3}_{-4.1\times10^3}$	$^{+6.6\times10^3}_{-6.5\times10^3}$	0.977	0.873
	10.0 - 16.0	1.20×10^4	5.9×10^2	$^{+1.2\times10^3}_{-3.3\times10^3}$	$^{+1.5\times10^3}_{-1.8\times10^3}$	0.98	0.86
	16.0 - 100.0	162	16	$^{+52}_{-31}$	$^{+32}_{-27}$	1.03	0.85
5.0 - 10	0.0 - 4.0	1.194×10^5	1.9×10^3	$^{+3.9\times10^3}_{-3.5\times10^3}$	$^{+7.1\times10^3}_{-8.1\times10^3}$	0.973	0.885
	4.0 - 10.0	4.88×10^4	8.4×10^2	$^{+2.1\times10^3}_{-3.9\times10^3}$	$^{+4.4\times10^3}_{-4.7\times10^3}$	0.967	0.859
	10.0 - 16.0	7.5×10^3	3.0×10^2	$^{+9.2\times10^2}_{-1.3\times10^3}$	$^{+1.3\times10^3}_{-9.1\times10^2}$	0.94	0.865
	16.0 - 100.0	130	10	$^{+10}_{-41}$	$^{+22}_{-23}$	0.94	0.84
10 - 25	0.0 - 4.0	4.44×10^4	6.0×10^2	$^{+1.8\times10^3}_{-1.7\times10^3}$	$^{+1.9\times10^3}_{-2.4\times10^3}$	0.959	0.883
	4.0 - 10.0	1.54×10^4	2.5×10^2	$^{+5.0\times10^2}_{-5.1\times10^2}$	$^{+1.5\times10^3}_{-1.4\times10^3}$	0.960	0.864
	10.0 - 16.0	2.52×10^3	9.7×10^1	$^{+1.6\times10^2}_{-4.9\times10^2}$	$^{+3.8\times10^2}_{-2.7\times10^2}$	0.939	0.855
	16.0 - 100.0	37	3	$^{+5}_{-12}$	$^{+5}_{-6}$	0.94	0.83
25 - 100	0.0 - 4.0	3.73×10^3	8.2×10^1	$^{+1.1\times10^2}_{-1.3\times10^2}$	$^{+1.2\times10^2}_{-1.6\times10^2}$	0.949	0.870
	4.0 - 10.0	921	26	$^{+86}_{-39}$	$^{+89}_{-84}$	0.947	0.847
	10.0 - 16.0	153	11	$^{+16}_{-27}$	$^{+19}_{-20}$	0.95	0.81
	16.0 - 100.0	2.68	0.35	$^{+0.32}_{-0.71}$	$^{+0.41}_{-0.61}$	0.93	0.82

$x_{\mathrm{Bj}} \times 10^4$	$\frac{\lvert\Delta\vec{p}^{\,\mathrm{jet1,2}}_{T,HCM}\rvert}{2E^{\mathrm{jet1}}_{T,HCM}}$	$\frac{d^2\sigma}{d\left(\frac{\lvert\Delta\vec{p}^{\,\mathrm{jet1,2}}_{T,HCM}\rvert}{2E^{\mathrm{jet1}}_{T,HCM}}\right)dx_{\mathrm{Bj}}}$ (pb)	δ_{stat} (pb)	δ_{syst} (pb)	δ_{ES} (pb)	C_{QED}	C_{had}
1.7 - 3.0	0.0 - 0.5	2.20×10^4	4.4×10^3	$^{+6.1\times10^3}_{-3.3\times10^3}$	$^{+4.3\times10^3}_{-1.9\times10^3}$	0.86	0.95
	0.5 - 0.7	1.95×10^5	2.1×10^4	$^{+4.6\times10^4}_{-2.3\times10^4}$	$^{+3.3\times10^4}_{-1.4\times10^4}$	0.98	0.89
	0.7 - 0.9	2.14×10^6	1.0×10^5	$^{+1.6\times10^5}_{-4.6\times10^5}$	$^{+1.8\times10^5}_{-1.9\times10^5}$	1.00	0.82
	0.9 - 1.0	3.28×10^6	9.0×10^4	$^{+2.7\times10^5}_{-1.8\times10^5}$	$^{+2.2\times10^5}_{-2.0\times10^5}$	0.987	0.912
3.0 - 5.0	0.0 - 0.5	3.5×10^4	5.0×10^3	$^{+9.3\times10^3}_{-1.4\times10^4}$	$^{+2.8\times10^3}_{-8.5\times10^3}$	1.01	0.88
	0.5 - 0.7	2.77×10^5	2.1×10^4	$^{+7.6\times10^4}_{-7.7\times10^4}$	$^{+3.1\times10^4}_{-3.3\times10^4}$	1.12	0.79
	0.7 - 0.9	2.62×10^6	8.2×10^4	$^{+2.1\times10^5}_{-4.6\times10^5}$	$^{+2.4\times10^5}_{-2.3\times10^5}$	0.96	0.86
	0.9 - 1.0	4.54×10^6	8.4×10^4	$^{+3.6\times10^5}_{-1.2\times10^5}$	$^{+2.9\times10^5}_{-2.8\times10^5}$	0.975	0.889
5.0 - 10	0.0 - 0.5	2.18×10^4	2.3×10^3	$^{+4.6\times10^3}_{-6.3\times10^3}$	$^{+4.1\times10^3}_{-4.4\times10^3}$	0.95	0.85
	0.5 - 0.7	1.61×10^5	9.2×10^3	$^{+3.1\times10^4}_{-2.5\times10^4}$	$^{+2.6\times10^4}_{-1.5\times10^4}$	0.97	0.83
	0.7 - 0.9	1.87×10^6	4.4×10^4	$^{+8.2\times10^4}_{-2.8\times10^5}$	$^{+1.7\times10^5}_{-1.9\times10^5}$	0.95	0.831
	0.9 - 1.0	3.37×10^6	4.7×10^4	$^{+9.1\times10^4}_{-6.2\times10^4}$	$^{+2.3\times10^5}_{-2.3\times10^5}$	0.970	0.877
10 - 25	0.0 - 0.5	5.5×10^3	5.3×10^2	$^{+1.1\times10^3}_{-1.4\times10^3}$	$^{+1.0\times10^3}_{-6.4\times10^2}$	0.98	0.78
	0.5 - 0.7	4.43×10^4	2.4×10^3	$^{+5.2\times10^3}_{-3.8\times10^3}$	$^{+7.1\times10^3}_{-5.5\times10^3}$	0.89	0.87
	0.7 - 0.9	6.05×10^5	1.3×10^4	$^{+1.3\times10^4}_{-5.3\times10^4}$	$^{+4.7\times10^4}_{-4.8\times10^4}$	0.96	0.825
	0.9 - 1.0	1.272×10^6	1.6×10^4	$^{+3.4\times10^4}_{-2.9\times10^4}$	$^{+7.8\times10^4}_{-8.4\times10^4}$	0.959	0.878
25 - 100	0.0 - 0.5	341	55	$^{+104}_{-83}$	$^{+42}_{-50}$	0.91	0.71
	0.5 - 0.7	3.34×10^3	3.2×10^2	$^{+2.8\times10^2}_{-3.5\times10^2}$	$^{+4.3\times10^2}_{-4.6\times10^2}$	0.99	0.77
	0.7 - 0.9	3.94×10^4	1.4×10^3	$^{+1.5\times10^3}_{-2.2\times10^3}$	$^{+3.0\times10^3}_{-3.2\times10^3}$	0.97	0.82
	0.9 - 1.0	1.065×10^5	2.2×10^3	$^{+3.2\times10^3}_{-3.1\times10^3}$	$^{+6.2\times10^3}_{-6.5\times10^3}$	0.948	0.864

Table B.10: The dijet double-differential cross sections as functions of $\lvert\Delta\vec{p}^{\,\mathrm{jet1,2}}_{T,HCM}\rvert/(2E^{\mathrm{jet1}}_{T,HCM})$. Other details as in the caption to Table 5.

$x_{\mathrm{Bj}} \times 10^4$	$\Delta\phi^{\mathrm{jet1,2}}_{HCM}$	$\frac{d^2\sigma}{d\left(\Delta\phi^{\mathrm{jet1,2}}_{HCM}\right)dx_{\mathrm{Bj}}}$ (pb)	δ_{stat} (pb)	δ_{syst} (pb)	δ_{ES} (pb)	C_{QED}	C_{had}
1.7 - 3.0	0.0 - $\pi/4$	6.6×10^3	1.8×10^3	$^{+5.3\times10^3}_{-3.3\times10^3}$	$^{+2.5\times10^3}_{-1.0\times10^3}$	0.78	1.1
	$\pi/4$ - $\pi/2$	2.21×10^4	3.5×10^3	$^{+5.0\times10^3}_{-3.8\times10^3}$	$^{+6.9\times10^2}_{-2.0\times10^3}$	1.00	0.83
	$\pi/2$ - $3\pi/4$	1.02×10^5	7.2×10^3	$^{+1.9\times10^4}_{-4.2\times10^3}$	$^{+1.2\times10^4}_{-8.7\times10^3}$	0.98	0.85
	$3\pi/4$ - π	9.46×10^5	2.0×10^4	$^{+5.9\times10^4}_{-7.9\times10^4}$	$^{+7.1\times10^4}_{-6.7\times10^4}$	0.988	0.916
3.0 - 5.0	0.0 - $\pi/4$	1.18×10^4	2.4×10^3	$^{+2.3\times10^3}_{-4.7\times10^3}$	$^{+1.3\times10^3}_{-2.3\times10^3}$	1.00	0.87
	$\pi/4$ - $\pi/2$	2.9×10^4	3.4×10^3	$^{+5.9\times10^3}_{-1.1\times10^4}$	$^{+1.8\times10^3}_{-6.7\times10^3}$	1.10	0.80
	$\pi/2$ - $3\pi/4$	1.39×10^5	6.9×10^3	$^{+1.4\times10^4}_{-1.3\times10^4}$	$^{+1.5\times10^4}_{-1.7\times10^4}$	0.98	0.839
	$3\pi/4$ - π	1.265×10^6	1.8×10^4	$^{+5.7\times10^4}_{-5.1\times10^4}$	$^{+9.4\times10^4}_{-8.6\times10^4}$	0.974	0.893
5.0 - 10	0.0 - $\pi/4$	6.9×10^3	1.0×10^3	$^{+1.2\times10^3}_{-2.9\times10^3}$	$^{+1.2\times10^3}_{-1.7\times10^3}$	0.91	0.81
	$\pi/4$ - $\pi/2$	1.84×10^4	1.7×10^3	$^{+2.1\times10^3}_{-4.3\times10^3}$	$^{+3.0\times10^3}_{-3.0\times10^3}$	0.95	0.84
	$\pi/2$ - $3\pi/4$	9.0×10^4	3.6×10^3	$^{+3.3\times10^3}_{-5.9\times10^3}$	$^{+1.0\times10^4}_{-8.6\times10^3}$	0.961	0.828
	$3\pi/4$ - π	9.35×10^5	1.0×10^4	$^{+2.9\times10^4}_{-3.0\times10^4}$	$^{+7.2\times10^4}_{-7.6\times10^4}$	0.970	0.881
10 - 25	0.0 - $\pi/4$	2.13×10^3	3.0×10^2	$^{+3.8\times10^2}_{-7.0\times10^2}$	$^{+4.1\times10^2}_{-2.1\times10^2}$	1.04	0.73
	$\pi/4$ - $\pi/2$	4.42×10^3	3.6×10^2	$^{+7.4\times10^2}_{-6.2\times10^2}$	$^{+7.1\times10^2}_{-5.8\times10^2}$	0.89	0.86
	$\pi/2$ - $3\pi/4$	2.72×10^4	1.1×10^3	$^{+1.7\times10^3}_{-5.2\times10^2}$	$^{+3.1\times10^3}_{-3.1\times10^3}$	0.945	0.822
	$3\pi/4$ - π	3.37×10^5	3.2×10^3	$^{+7.0\times10^3}_{-7.7\times10^3}$	$^{+2.3\times10^4}_{-2.4\times10^4}$	0.960	0.881
25 - 100	0.0 - $\pi/4$	98	22	$^{+27}_{-34}$	$^{+3}_{-13}$	0.85	0.70
	$\pi/4$ - $\pi/2$	354	53	$^{+55}_{-97}$	$^{+39}_{-62}$	0.97	0.79
	$\pi/2$ - $3\pi/4$	1.74×10^3	1.2×10^2	$^{+4.0\times10^2}_{-1.9\times10^2}$	$^{+2.1\times10^2}_{-2.0\times10^2}$	0.94	0.808
	$3\pi/4$ - π	2.63×10^4	4.1×10^2	$^{+9.8\times10^2}_{-5.9\times10^2}$	$^{+1.7\times10^3}_{-1.8\times10^3}$	0.949	0.867

Table B.11: The dijet double-differential cross sections as functions of $\Delta\phi^{\mathrm{jet1,2}}_{HCM}$. Other details as in the caption to Table 5.

Q^2 (GeV^2)	$\frac{d\sigma}{dQ^2}$ (pb/GeV^2)	δ_{stat} (pb/GeV^2)	δ_{syst} (pb/GeV^2)	δ_{ES} (pb/GeV^2)	C_{QED}	C_{had}
10 - 15	7.9	0.2	$^{+1.1}_{-1.3}$	$^{+1.0}_{-1.0}$	0.991	0.759
15 - 20	4.40	0.17	$^{+0.46}_{-0.66}$	$^{+0.45}_{-0.52}$	0.946	0.776
20 - 30	3.19	0.11	$^{+0.27}_{-0.37}$	$^{+0.38}_{-0.38}$	0.969	0.786
30 - 50	1.68	0.06	$^{+0.13}_{-0.11}$	$^{+0.20}_{-0.19}$	0.949	0.794
50 - 100	0.719	0.024	$^{+0.044}_{-0.027}$	$^{+0.077}_{-0.070}$	0.956	0.795

Table B.12: The inclusive trijet cross sections as functions of Q^2. Other details as in the caption to Table 1.

$x_{\mathrm{Bj}} \times 10^{-4}$	$\frac{d\sigma}{dx_{\mathrm{Bj}}}$ (pb, $\times 10^{-4}$)	δ_{stat} (pb, $\times 10^{-4}$)	δ_{syst} (pb, $\times 10^{-4}$)	δ_{ES} (pb, $\times 10^{-4}$)	C_{QED}	C_{had}
1.7 - 3.0	14.7	0.7	$^{+1.5}_{-3.3}$	$^{+1.5}_{-1.9}$	1.00	0.811
3.0 - 5.0	15.9	0.5	$^{+2.0}_{-2.3}$	$^{+1.9}_{-1.8}$	0.968	0.796
5.0 - 10.0	9.6	0.3	$^{+0.9}_{-0.9}$	$^{+1.1}_{-1.1}$	0.961	0.780
10.0 - 25.0	3.35	0.10	$^{+0.21}_{-0.19}$	$^{+0.40}_{-0.37}$	0.954	0.785
25.0 - 100.0	0.192	0.013	$^{+0.032}_{-0.020}$	$^{+0.023}_{-0.022}$	0.95	0.739

Table B.13: The inclusive trijet cross sections as functions of x_{Bj}. Other details as in the caption to Table 1.

$E_{T,HCM}^{jet,1}$ (GeV)	$\frac{d\sigma}{dE_{T,HCM}^{jet,1}}$ (pb/ GeV)	δ_{stat} (pb/ GeV)	δ_{syst} (pb/ GeV)	δ_{ES} (pb/ GeV)	C_{QED}	C_{had}
5 - 8	5.4	0.4	$^{+0.6}_{-5.4}$	$^{+0.6}_{-0.5}$	0.95	0.750
8 - 12	19.1	0.5	$^{+1.5}_{-0.8}$	$^{+1.7}_{-2.0}$	0.965	0.764
12 - 16	11.6	0.4	$^{+0.1}_{-0.7}$	$^{+1.5}_{-1.4}$	0.965	0.799
16 - 20	4.58	0.19	$^{+0.25}_{-0.26}$	$^{+0.68}_{-0.58}$	0.96	0.823
20 - 25	1.71	0.09	$^{+0.07}_{-0.22}$	$^{+0.24}_{-0.21}$	0.96	0.83
25 - 30	0.615	0.052	$^{+0.019}_{-0.037}$	$^{+0.091}_{-0.142}$	0.98	0.81
30 - 40	0.116	0.014	$^{+0.035}_{-0.018}$	$^{+0.025}_{-0.016}$	0.97	0.83
40 - 60	0.0119	0.0036	$^{+0.0032}_{-0.0059}$	$^{+0.0028}_{-0.0018}$	1.03	0.78

Table B.14: The inclusive trijet cross sections as functions of $E_{T,HCM}^{jet,1}$. Other details as in the caption to Table 1.

$E_{T,HCM}^{jet,2}$ (GeV)	$\frac{d\sigma}{dE_{T,HCM}^{jet,2}}$ (pb/ GeV)	δ_{stat} (pb/ GeV)	δ_{syst} (pb/ GeV)	δ_{ES} (pb/ GeV)	C_{QED}	C_{had}
5 - 8	23.9	0.7	$^{+1.4}_{-0.9}$	$^{+2.1}_{-2.4}$	0.951	0.774
8 - 12	17.2	0.4	$^{+0.3}_{-0.6}$	$^{+2.1}_{-2.1}$	0.975	0.773
12 - 16	4.85	0.19	$^{+0.14}_{-0.27}$	$^{+0.76}_{-0.60}$	0.96	0.816
16 - 20	1.31	0.09	$^{+0.09}_{-0.10}$	$^{+0.19}_{-0.16}$	0.96	0.84
20 - 25	0.470	0.045	$^{+0.064}_{-0.042}$	$^{+0.100}_{-0.100}$	0.98	0.82
25 - 30	0.115	0.020	$^{+0.018}_{-0.011}$	$^{+0.029}_{-0.014}$	0.90	0.84
30 - 40	0.029	0.007	$^{+0.014}_{-0.010}$	$^{+0.005}_{-0.004}$	1.06	0.77
40 - 60	0.0049	0.0033	$^{+0.0012}_{-0.0052}$	$^{+0.0000}_{-0.0016}$	1.3	0.78

Table B.15: The inclusive trijet cross sections as functions of $E_{T,HCM}^{jet,2}$. Other details as in the caption to Table 1.

$E_{T,HCM}^{jet,3}$ (GeV)	$\frac{d\sigma}{dE_{T,HCM}^{jet,3}}$ (pb/ GeV)	δ_{stat} (pb/ GeV)	δ_{syst} (pb/ GeV)	δ_{ES} (pb/ GeV)	C_{QED}	C_{had}
5 - 8	46.3	0.8	$^{+1.9}_{-2.0}$	$^{+5.1}_{-5.2}$	0.964	0.777
8 - 12	6.15	0.21	$^{+0.11}_{-0.22}$	$^{+0.87}_{-0.76}$	0.956	0.801
12 - 16	0.77	0.06	$^{+0.10}_{-0.03}$	$^{+0.11}_{-0.11}$	0.95	0.82
16 - 20	0.121	0.022	$^{+0.009}_{-0.036}$	$^{+0.020}_{-0.014}$	1.00	0.88
20 - 25	0.026	0.009	$^{+0.021}_{-0.012}$	$^{+0.004}_{0.000}$	0.96	0.90
25 - 30	0.0018	0.0019	$^{+0.0018}_{-0.0007}$	$^{+0.0036}_{0.0000}$	0.8	1.1

Table B.16: The inclusive trijet cross sections as functions of $E_{T,HCM}^{jet,3}$. Other details as in the caption to Table 1.

$\eta_{LAB}^{jet,1}$	$\frac{d\sigma}{d\eta_{LAB}^{jet,1}}$ (pb)	δ_{stat} (pb)	δ_{syst} (pb)	δ_{ES} (pb)	C_{QED}	C_{had}
-1.0 - -0.5	0.00	0.00	$^{+0.00}_{-0.00}$	$^{+0.00}_{0.00}$	0.00	0.00
-0.5 - 0.0	0.38	0.22	$^{+0.27}_{-0.42}$	$^{+0.14}_{-0.10}$	1.2	0.42
0.0 - 0.5	6.0	0.7	$^{+0.8}_{-2.0}$	$^{+1.3}_{-1.2}$	0.95	0.62
0.5 - 1.0	27.9	1.5	$^{+0.4}_{-1.9}$	$^{+3.6}_{-3.4}$	0.97	0.731
1.0 - 1.5	60.5	2.2	$^{+5.5}_{-4.5}$	$^{+7.5}_{-8.0}$	0.963	0.779
1.5 - 2.0	96	3	$^{+11}_{-11}$	$^{+11}_{-11}$	0.963	0.789
2.0 - 2.5	133	3	$^{+15}_{-14}$	$^{+14}_{-13}$	0.960	0.799

Table B.17: The inclusive trijet cross sections as functions of $\eta_{LAB}^{jet,1}$. Other details as in the caption to Table 1.

$\eta_{LAB}^{jet,2}$	$\frac{d\sigma}{d\eta_{LAB}^{jet,2}}$ (pb)	δ_{stat} (pb)	δ_{syst} (pb)	δ_{ES} (pb)	C_{QED}	C_{had}
-1.0 - -0.5	0.9	0.5	$^{+3.2}_{-1.0}$	$^{+0.3}_{-0.2}$	0.99	0.33
-0.5 - 0.0	18.1	1.4	$^{+2.2}_{-2.1}$	$^{+3.1}_{-3.3}$	0.97	0.606
0.0 - 0.5	61.7	2.3	$^{+2.8}_{-3.8}$	$^{+8.1}_{-7.9}$	0.963	0.746
0.5 - 1.0	95	3	$^{+12}_{-9}$	$^{+12}_{-11}$	0.970	0.799
1.0 - 1.5	84.1	2.4	$^{+6.1}_{-8.5}$	$^{+9.1}_{-9.5}$	0.963	0.826
1.5 - 2.0	48.9	1.8	$^{+5.6}_{-4.5}$	$^{+4.6}_{-4.5}$	0.943	0.835
2.0 - 2.5	15.0	1.3	$^{+1.0}_{-3.2}$	$^{+1.0}_{-1.1}$	0.96	0.86

Table B.18: The inclusive trijet cross sections as functions of $\eta_{LAB}^{jet,2}$. Other details as in the caption to Table 1.

$\eta^{jet,3}_{LAB}$	$\frac{d\sigma}{d\eta^{jet,3}_{LAB}}$ (pb)	δ_{stat} (pb)	δ_{syst} (pb)	δ_{ES} (pb)	C_{QED}	C_{had}
-1.0 - -0.5	53.6	2.3	$^{+4.3}_{-6.3}$	$^{+8.4}_{-7.9}$	0.960	0.681
-0.5 - 0.0	96	3	$^{+7}_{-10}$	$^{+12}_{-11}$	0.972	0.785
0.0 - 0.5	90	2	$^{+10}_{-9}$	$^{+10}_{-10}$	0.960	0.823
0.5 - 1.0	58.0	2.0	$^{+3.7}_{-5.5}$	$^{+5.7}_{-5.8}$	0.956	0.828
1.0 - 1.5	23.0	1.3	$^{+1.3}_{-2.1}$	$^{+2.1}_{-2.0}$	0.96	0.86
1.5 - 2.0	4.12	0.53	$^{+0.48}_{-0.74}$	$^{+0.32}_{-0.20}$	0.94	0.87
2.0 - 2.5	0.31	0.17	$^{+0.11}_{-0.22}$	$^{+0.00}_{0.00}$	1.1	0.8

Table B.19: The inclusive trijet cross sections as functions of $\eta^{jet,3}_{LAB}$. Other details as in the caption to Table 1.

$\Delta\eta^{\mathrm{jet1,2}}_{HCM}$	$\frac{d\sigma}{d\Delta\eta^{\mathrm{jet1,2}}_{HCM}}$ (pb)	δ_{stat} (pb)	δ_{syst} (pb)	δ_{ES} (pb)	C_{QED}	C_{had}
0.0 - 0.7	88.5	2.1	$^{+5.6}_{-9.0}$	$^{+9.3}_{-9.6}$	0.963	0.784
0.7 - 1.4	75.6	2.1	$^{+3.6}_{-8.4}$	$^{+8.6}_{-9.4}$	0.956	0.800
1.4 - 2.1	44.9	1.7	$^{+6.2}_{-4.3}$	$^{+5.9}_{-5.2}$	0.962	0.784
2.1 - 2.8	19.3	1.2	$^{+3.4}_{-2.1}$	$^{+2.7}_{-2.2}$	0.98	0.756
2.8 - 3.5	3.1	0.5	$^{+1.2}_{-0.7}$	$^{+0.7}_{-0.2}$	0.95	0.66

Table B.20: The inclusive trijet cross sections as functions of $\Delta\eta^{\mathrm{jet1,2}}_{HCM}$. Other details as in the caption to Table 1.

$x_{\rm Bj} \times 10^4$	$\Delta E^{\rm jet1,2}_{T,HCM}$ (GeV)	$\frac{d^2\sigma}{d\left(\Delta E^{\rm jet1,2}_{T,HCM}\right)dx_{\rm Bj}}$ (pb/ GeV)	δ_{stat} (pb/ GeV)	δ_{syst} (pb/ GeV)	δ_{ES} (pb/ GeV)	C_{QED}	C_{had}
1.7 - 3.0	0.0 - 4.0	2.40×10^4	1.5×10^3	$^{+2.5\times10^3}_{-6.1\times10^3}$	$^{+2.5\times10^3}_{-3.2\times10^3}$	0.99	0.801
	4.0 - 10.0	8.1×10^3	6.8×10^2	$^{+4.2\times10^2}_{-1.6\times10^3}$	$^{+7.5\times10^2}_{-9.3\times10^2}$	1.02	0.83
	10.0 - 18.0	638	123	$^{+782}_{-191}$	$^{+91}_{-130}$	1.04	0.87
3.0 - 5.0	0.0 - 4.0	2.67×10^4	1.2×10^3	$^{+3.6\times10^3}_{-2.9\times10^3}$	$^{+2.9\times10^3}_{-2.7\times10^3}$	0.97	0.788
	4.0 - 10.0	8.1×10^3	4.9×10^2	$^{+1.4\times10^3}_{-1.8\times10^3}$	$^{+1.2\times10^3}_{-1.1\times10^3}$	0.96	0.82
	10.0 - 18.0	599	96	$^{+118}_{-160}$	$^{+100}_{-64}$	1.08	0.77
5.0 - 10	0.0 - 4.0	1.67×10^4	6.3×10^2	$^{+1.1\times10^3}_{-1.4\times10^3}$	$^{+1.9\times10^3}_{-1.8\times10^3}$	0.966	0.766
	4.0 - 10.0	4.69×10^3	2.5×10^2	$^{+5.7\times10^2}_{-4.1\times10^2}$	$^{+5.9\times10^2}_{-6.0\times10^2}$	0.95	0.815
	10.0 - 18.0	321	43	$^{+85}_{-87}$	$^{+47}_{-56}$	0.97	0.85
10 - 25	0.0 - 4.0	5.65×10^3	2.2×10^2	$^{+4.8\times10^2}_{-2.3\times10^2}$	$^{+6.3\times10^2}_{-6.2\times10^2}$	0.952	0.775
	4.0 - 10.0	1.73×10^3	9.6×10^1	$^{+3.7\times10^1}_{-1.5\times10^2}$	$^{+2.2\times10^2}_{-1.9\times10^2}$	0.96	0.813
	10.0 - 18.0	123	17	$^{+18}_{-49}$	$^{+19}_{-15}$	0.97	0.77
25 - 100	0.0 - 4.0	344	29	$^{+51}_{-33}$	$^{+38}_{-35}$	0.95	0.731
	4.0 - 10.0	81	10	$^{+17}_{-10}$	$^{+11}_{-10}$	0.95	0.76

Table B.21: The trijet double-differential cross sections as functions of $\Delta E^{\rm jet1,2}_{T,HCM}$. Other details as in the caption to Table 5.

$x_{\rm Bj} \times 10^4$	$\lvert\Sigma\vec{p}_{T,HCM}^{\rm jet1,2}\rvert$ (GeV)	$\frac{d^2\sigma}{d\left(\lvert\Sigma\vec{p}_{T,HCM}^{\rm jet1,2}\rvert\right)dx_{\rm Bj}}$ (pb/ GeV)	δ_{stat} (pb/ GeV)	δ_{syst} (pb/ GeV)	δ_{ES} (pb/ GeV)	C_{QED}	C_{had}
1.7 - 3.0	0.0 - 4.0	6.7×10^3	8.2×10^2	$^{+1.3\times10^3}_{-2.3\times10^3}$	$^{+6.3\times10^2}_{-8.2\times10^2}$	0.98	0.85
	4.0 - 10.0	1.43×10^4	9.6×10^2	$^{+1.9\times10^3}_{-3.3\times10^3}$	$^{+1.4\times10^3}_{-1.7\times10^3}$	1.00	0.798
	10.0 - 16.0	5.3×10^3	4.9×10^2	$^{+3.6\times10^2}_{-1.4\times10^3}$	$^{+4.8\times10^2}_{-7.0\times10^2}$	1.04	0.85
	16.0 - 100.0	89	17	$^{+7}_{-23}$	$^{+16}_{-17}$	1.01	0.79
3.0 - 5.0	0.0 - 4.0	6.8×10^3	6.2×10^2	$^{+1.4\times10^3}_{-9.3\times10^2}$	$^{+9.8\times10^2}_{-6.3\times10^2}$	0.96	0.86
	4.0 - 10.0	1.55×10^4	7.4×10^2	$^{+2.9\times10^3}_{-2.7\times10^3}$	$^{+1.4\times10^3}_{-1.6\times10^3}$	0.97	0.778
	10.0 - 16.0	5.7×10^3	4.1×10^2	$^{+4.3\times10^2}_{-1.9\times10^3}$	$^{+9.5\times10^2}_{-7.2\times10^2}$	0.98	0.83
	16.0 - 100.0	74	10	$^{+18}_{-37}$	$^{+13}_{-13}$	0.93	0.81
5.0 - 10	0.0 - 4.0	4.17×10^3	3.1×10^2	$^{+4.9\times10^2}_{-4.4\times10^2}$	$^{+6.3\times10^2}_{-4.9\times10^2}$	0.96	0.84
	4.0 - 10.0	9.7×10^3	4.0×10^2	$^{+1.7\times10^3}_{-9.0\times10^2}$	$^{+9.5\times10^2}_{-1.1\times10^3}$	0.966	0.761
	10.0 - 16.0	3.04×10^3	2.0×10^2	$^{+1.9\times10^2}_{-5.6\times10^2}$	$^{+4.6\times10^2}_{-3.3\times10^2}$	0.93	0.83
	16.0 - 100.0	54	6	$^{+3}_{-23}$	$^{+6}_{-9}$	0.92	0.82
10 - 25	0.0 - 4.0	1.46×10^3	1.2×10^2	$^{+1.6\times10^2}_{-2.2\times10^2}$	$^{+2.3\times10^2}_{-1.7\times10^2}$	0.97	0.81
	4.0 - 10.0	3.61×10^3	1.5×10^2	$^{+1.8\times10^2}_{-1.7\times10^2}$	$^{+3.5\times10^2}_{-3.5\times10^2}$	0.955	0.772
	10.0 - 16.0	945	66	$^{+51}_{-159}$	$^{+126}_{-105}$	0.93	0.84
	16.0 - 100.0	15.0	1.8	$^{+2.1}_{-3.6}$	$^{+2.3}_{-3.3}$	0.94	0.77
25 - 100	0.0 - 4.0	123	21	$^{+17}_{-66}$	$^{+10}_{-13}$	0.93	0.74
	4.0 - 10.0	188	17	$^{+44}_{-17}$	$^{+23}_{-19}$	0.96	0.734
	10.0 - 16.0	48	7	$^{+11}_{-16}$	$^{+5}_{-5}$	0.93	0.77
	16.0 - 100.0	0.43	0.15	$^{+0.11}_{-0.21}$	$^{+0.10}_{-0.09}$	0.90	0.76

Table B.22: The trijet double-differential cross sections as functions of $\lvert\Sigma\vec{p}_{T,HCM}^{\rm jet1,2}\rvert$. Other details as in the caption to Table 5.

$x_{\rm Bj} \times 10^4$	$\frac{\lvert\Delta\vec{p}^{\rm jet1,2}_{T,HCM}\rvert}{2E^{\rm jet1}_{T,HCM}}$	$\frac{d^2\sigma}{d\left(\frac{\lvert\Delta\vec{p}^{\rm jet1,2}_{T,HCM}\rvert}{2E^{\rm jet1}_{T,HCM}}\right)dx_{\rm Bj}}$ (pb)	δ_{stat} (pb)	δ_{syst} (pb)	δ_{ES} (pb)	C_{QED}	C_{had}
1.7 - 3.0	0.5 - 0.7	6.5×10^4	1.2×10^4	${}^{+2.7\times10^{3}}_{-2.4\times10^{4}}$	${}^{+4.4\times10^{3}}_{-1.0\times10^{4}}$	1.0	0.70
	0.7 - 0.9	4.5×10^5	3.8×10^4	${}^{+1.3\times10^{5}}_{-1.1\times10^{5}}$	${}^{+4.3\times10^{4}}_{-4.6\times10^{4}}$	0.99	0.81
	0.9 - 1.0	4.1×10^5	3.1×10^4	${}^{+2.7\times10^{4}}_{-1.2\times10^{5}}$	${}^{+4.9\times10^{4}}_{-6.3\times10^{4}}$	1.00	0.812
3.0 - 5.0	0.0 - 0.5	8.5×10^3	2.0×10^3	${}^{+4.2\times10^{3}}_{-5.7\times10^{3}}$	${}^{+2.8\times10^{3}}_{-6.2\times10^{2}}$	1.0	0.81
	0.5 - 0.7	7.8×10^4	1.0×10^4	${}^{+1.4\times10^{4}}_{-5.1\times10^{4}}$	${}^{+1.1\times10^{4}}_{-9.4\times10^{3}}$	1.04	0.76
	0.7 - 0.9	5.31×10^5	3.3×10^4	${}^{+5.9\times10^{4}}_{-9.0\times10^{4}}$	${}^{+6.2\times10^{4}}_{-6.4\times10^{4}}$	0.98	0.85
	0.9 - 1.0	4.10×10^5	2.2×10^4	${}^{+8.0\times10^{4}}_{-4.8\times10^{4}}$	${}^{+4.5\times10^{4}}_{-4.1\times10^{4}}$	0.967	0.794
5.0 - 10	0.0 - 0.5	4.7×10^3	9.1×10^2	${}^{+1.2\times10^{3}}_{-2.8\times10^{3}}$	${}^{+5.9\times10^{2}}_{-5.9\times10^{2}}$	0.9	0.96
	0.5 - 0.7	5.2×10^4	5.9×10^3	${}^{+3.2\times10^{3}}_{-1.5\times10^{4}}$	${}^{+7.5\times10^{3}}_{-4.3\times10^{3}}$	1.05	0.70
	0.7 - 0.9	3.02×10^5	1.6×10^4	${}^{+4.9\times10^{4}}_{-2.7\times10^{4}}$	${}^{+3.7\times10^{4}}_{-3.7\times10^{4}}$	0.95	0.80
	0.9 - 1.0	2.57×10^5	1.2×10^4	${}^{+1.9\times10^{4}}_{-2.2\times10^{4}}$	${}^{+2.8\times10^{4}}_{-3.0\times10^{4}}$	0.961	0.780
10 - 25	0.0 - 0.5	1.18×10^3	2.4×10^2	${}^{+3.3\times10^{2}}_{-3.2\times10^{2}}$	${}^{+2.2\times10^{2}}_{-2.1\times10^{2}}$	1.0	0.78
	0.5 - 0.7	1.08×10^4	1.3×10^3	${}^{+1.5\times10^{3}}_{-3.5\times10^{3}}$	${}^{+1.4\times10^{3}}_{-1.3\times10^{3}}$	0.84	0.85
	0.7 - 0.9	1.15×10^5	6.1×10^3	${}^{+4.9\times10^{3}}_{-9.9\times10^{3}}$	${}^{+1.2\times10^{4}}_{-1.3\times10^{4}}$	0.97	0.81
	0.9 - 1.0	9.3×10^4	4.4×10^3	${}^{+7.9\times10^{3}}_{-4.8\times10^{3}}$	${}^{+1.2\times10^{4}}_{-9.8\times10^{3}}$	0.955	0.783
25 - 100	0.5 - 0.7	640	158	${}^{+264}_{-260}$	${}^{+68}_{-75}$	1.0	0.71
	0.7 - 0.9	6.4×10^3	7.1×10^2	${}^{+1.7\times10^{3}}_{-6.5\times10^{2}}$	${}^{+7.9\times10^{2}}_{-6.9\times10^{2}}$	0.94	0.76
	0.9 - 1.0	5.7×10^3	6.4×10^2	${}^{+7.3\times10^{2}}_{-1.3\times10^{3}}$	${}^{+6.5\times10^{2}}_{-6.7\times10^{2}}$	0.95	0.739

Table B.23: The trijet double-differential cross sections as functions of $\lvert\Delta\vec{p}^{\rm jet1,2}_{T,HCM}\rvert/(2E^{\rm jet1}_{T,HCM})$. Other details as in the caption to Table 5.

$x_{\mathrm{Bj}} \times 10^4$	$\Delta\phi_{HCM}^{\mathrm{jet1,2}}$	$\frac{d^2\sigma}{d\left(\Delta\phi_{HCM}^{\mathrm{jet1,2}}\right)dx_{\mathrm{Bj}}}$ (pb)	δ_{stat} (pb)	δ_{syst} (pb)	δ_{ES} (pb)	C_{QED}	C_{had}
1.7 - 3.0	0.0 - $\pi/2$	4.9×10^3	1.0×10^3	$^{+6.5\times10^2}_{-3.5\times10^3}$	$^{+4.2\times10^2}_{-6.4\times10^2}$	0.92	0.75
	$\pi/2$ - $3\pi/4$	3.76×10^4	4.0×10^3	$^{+9.7\times10^3}_{-8.6\times10^3}$	$^{+3.4\times10^3}_{-4.6\times10^3}$	0.97	0.82
	$3\pi/4$ - π	1.37×10^5	7.2×10^3	$^{+1.5\times10^4}_{-3.3\times10^4}$	$^{+1.5\times10^4}_{-1.8\times10^4}$	1.01	0.811
3.0 - 5.0	0.0 - $\pi/2$	5.9×10^3	8.6×10^2	$^{+1.5\times10^3}_{-3.9\times10^3}$	$^{+1.3\times10^3}_{-7.1\times10^2}$	1.04	0.77
	$\pi/2$ - $3\pi/4$	4.76×10^4	3.7×10^3	$^{+5.1\times10^3}_{-5.2\times10^3}$	$^{+5.7\times10^3}_{-4.2\times10^3}$	0.97	0.79
	$3\pi/4$ - π	1.42×10^5	5.5×10^3	$^{+2.1\times10^4}_{-2.2\times10^4}$	$^{+1.7\times10^4}_{-1.7\times10^4}$	0.966	0.798
5.0 - 10	0.0 - $\pi/2$	3.5×10^3	4.4×10^2	$^{+5.2\times10^2}_{-1.4\times10^3}$	$^{+4.8\times10^2}_{-2.8\times10^2}$	0.95	0.79
	$\pi/2$ - $3\pi/4$	3.08×10^4	2.0×10^3	$^{+1.4\times10^3}_{-5.3\times10^3}$	$^{+3.7\times10^3}_{-3.1\times10^3}$	0.95	0.780
	$3\pi/4$ - π	8.5×10^4	2.9×10^3	$^{+1.4\times10^4}_{-6.9\times10^3}$	$^{+9.9\times10^3}_{-1.1\times10^4}$	0.964	0.780
10 - 25	0.0 - $\pi/2$	772	103	$^{+138}_{-65}$	$^{+131}_{-110}$	0.87	0.82
	$\pi/2$ - $3\pi/4$	8.6×10^3	6.0×10^2	$^{+1.0\times10^3}_{-4.3\times10^2}$	$^{+8.7\times10^2}_{-9.4\times10^2}$	0.94	0.778
	$3\pi/4$ - π	3.25×10^4	1.1×10^3	$^{+1.3\times10^3}_{-2.5\times10^3}$	$^{+3.9\times10^3}_{-3.6\times10^3}$	0.960	0.786
25 - 100	0.0 - $\pi/2$	41	11	$^{+7}_{-9}$	$^{+5}_{-6}$	0.99	0.73
	$\pi/2$ - $3\pi/4$	548	81	$^{+221}_{-78}$	$^{+65}_{-60}$	0.95	0.73
	$3\pi/4$ - π	1.83×10^3	1.5×10^2	$^{+2.8\times10^2}_{-2.0\times10^2}$	$^{+2.2\times10^2}_{-2.0\times10^2}$	0.95	0.740

Table B.24: The trijet double-differential cross sections as functions of $\Delta\phi_{HCM}^{\mathrm{jet1,2}}$. Other details as in the caption to Table 5.

Variable	Bin	Boundaries
$\Delta E_{T,\mathrm{HCM}}^{\mathrm{jet1,2}}$	1	$0-4$ GeV
	2	$4-10$ GeV
	3	$10-18$ GeV
	4	$18-100$ GeV
$\lvert\Sigma\vec{p}_{T,\mathrm{HCM}}^{\,\mathrm{jet1,2}}\rvert$	1	$0-4$ GeV
	2	$4-10$ GeV
	3	$10-16$ GeV
	4	$16-100$ GeV
$\lvert\Delta\vec{p}_{T,\mathrm{HCM}}^{\,\mathrm{jet1,2}}\rvert/2E_{T,\mathrm{HCM}}^{\mathrm{jet1}}$	1	$0-0.5$
	2	$0.5-0.7$
	3	$0.7-0.85$
	4	$0.85-1$
$\lvert\Delta\phi_{\mathrm{HCM}}^{\mathrm{jet1,2}}\rvert$	1	$0-\pi/4$
	2	$\pi/4-\pi/2$
	3	$\pi/2-3\pi/4$
	4	$3\pi/4-\pi$

Table B.25: The bin edges used for the measurements of the jet correlations presented. For the trijet sample, the first two bins in $\lvert\Delta\phi_{\mathrm{HCM}}^{\mathrm{jet1,2}}\rvert$ are combined.

Bibliography

[1] ZEUS Coll., S. Chekanov et al., Preprint DESY-07-062, DESY, 2007. Accepted by Nucl. Phys. B.

[2] ZEUS Coll., S. Chekanov et al., Eur. Phys. J. **C 44**, 183 (2005).

[3] H1 Coll., C. Adloff et al., Phys. Lett. **B 515**, 17 (2001).

[4] H1 Coll., C. Adloff et al., Eur. Phys. J. **C 6**, 575 (1999).

[5] ZEUS Coll., M. Derrick et al., Phys. Lett. **B 363**, 201 (1995).

[6] ZEUS Coll., J. Breitweg et al., Phys. Lett. **B 507**, 70 (2001).

[7] ZEUS Coll., S. Chekanov et al., Phys. Lett. **B 547**, 164 (2002).

[8] ZEUS Coll., S. Chekanov et al., Phys. Lett. **B 558**, 41 (2003).

[9] H1 Coll., C. Adloff et al., Eur. Phys. J. **C 19**, 289 (2001).

[10] H1 Coll., C. Adloff et al., Eur. Phys. J. **C 21**, 33 (2001).

[11] ZEUS Coll., S. Chekanov et al., Nucl. Phys. **B 700**, 3 (2004).

[12] ZEUS Coll., S. Chekanov et al., Phys. Lett. **B 560**, 7 (2003).

[13] J.D. Bjorken, Phys. Rev. **179**, 1547 (1969).

[14] V.N. Gribov and L.N. Lipatov, Sov. J. Nucl. Phys. **15**, 438 (1972).

[15] G. Altarelli and G. Parisi, Nucl. Phys. **B 126**, 298 (1977);
L.N. Lipatov, Sov. J. Nucl. Phys. **20**, 94 (1975);
Yu.L. Dokshitzer, Sov. Phys. JETP **46**, 641 (1977).

[16] ZEUS Coll., S. Chekanov et al., Phys. Rev. **D 67**, 012007 (2003).

[17] H1 Coll., Adloff, C. et al., Phys. Lett. **B515**, 17 (2001).

[18] ZEUS Coll., S. Chekanov et al., Eur. Phys. J. **C 23**, 13 (2002).

[19] ZEUS Coll., S. Chekanov et al., Eur. Phys. J. **C 21**, 443 (2001);
H1 Coll., S. Aid et al., Nucl. Phys. **B 470**, 3 (1996).

[20] H1 Coll., A. Aktas et al., Eur. Phys. J. **C 33**, 477 (2004).

[21] Gross, D. J. and Wilczek, Frank, Phys. Rev. Lett. **30**, 1343 (1973).

[22] Politzer, H. David, Phys. Rev. Lett. **30**, 1346 (1973).

[23] Gross, D. J. and Wilczek, Frank, Phys. Rev. **D8**, 3633 (1973).

[24] Politzer, H. David, Phys. Rept. **14**, 129 (1974).

[25] *Nobel Prize in Physics 2004*, available on `http://nobelprize.org/nobel_prizes/physics/laureates/2004/`.

[26] CTEQ Coll., G. Sterman et al., Rev. Mod. Phys. **67**, 157 (1995).

[27] E.A. Kuraev, L.N. Lipatov and V.S. Fadin, Sov. Phys. JETP **45**, 199 (1977);
Ya.Ya. Balitskiĭ and L.N. Lipatov, Sov. J. Nucl. Phys. **28**, 822 (1978).

[28] Z. Nagy and Z. Trócsányi, Phys. Rev. Lett. **87**, 082001 (2001).

[29] N. Krumnack, *Three Jet Events in Deep Inelastic Scattering*. Ph.D. Thesis, University of Hamburg, Report DESY-THESIS-2004-011, 2004.

[30] L. Li, *Three Jet Production in Neutral Current Deep Inelastic Scattering with ZEUSat HERA*. Ph.D. Thesis, University of Wisconsin – Madison, 2005.

[31] S. Catani and M. H. Seymour, Nucl. Phys. **B 485**, 291 (1997). Erratum in Nucl. Phys **B 510**, 503 (1997).

[32] W.A. Bardeen et al., Phys. Rev. **D 18**, 3998 (1978).

[33] J. Pumplin et al., JHEP **07**, 012 (2002).

[34] R.K. Ellis, D.A. Ross and A.E. Terrano, Nucl. Phys. **B178**, 421 (1981).

[35] S.Catani et al., Nucl. Phys. **B 406**, 187 (1993).

[36] S.D. Ellis and D.E. Soper, Phys. Rev. **D 48**, 3160 (1993).

[37] A. Kwiatkowski, H. Spiesberger and H.-J. Möhring, Comp. Phys. Comm. **69**, 155 (1992). Also in *Proc. Workshop Physics at HERA*, eds. W. Buchmüller and G.Ingelman, (DESY, Hamburg, 1991).

[38] K. Charchula, G.A. Schuler and H. Spiesberger, Comp. Phys. Comm. **81**, 381 (1994).

[39] G. Ingelman, A. Edin and J. Rathsman, Comp. Phys. Comm. **101**, 108 (1997).

[40] L. Lönnblad, Comp. Phys. Comm. **71**, 15 (1992).

[41] T. Sjöstrand, Comp. Phys. Comm. **82**, 74 (1994).

[42] R. Brun et al., GEANT3, Technical Report CERN-DD/EE/84-1, CERN, 1987.

[43] *DESY webpage*, available on `http://www.desy.de`.

[44] ZEUS Coll., U. Holm (ed.), *The ZEUS Detector*. Status Report (unpublished), DESY (1993), available on `http://www-zeus.desy.de/bluebook/bluebook.html`.

[45] ZEUS Coll., UK group, C.B. Brooks et al., Nucl. Inst. Meth. **A 283**, 477 (1989).

[46] J. Krüger, *The Uranium Scintillator Calorimeter for the ZEUS Detector at the Electron - Proton collider HERA: The Heart of ZEUS*. Habilitation Thesis, Universität Hamburg, Report DESY-F35-92-02, 1992.

[47] A. Bamberger et al., Nucl. Inst. Meth. **A 401**, 63 (1997).

[48] A. Bamberger et al., Nucl. Inst. Meth. **A 382**, 419 (1996).

[49] K. J. Gaemers and M. van der Horst, Nucl. Phys. **B 316**, 269 (1989).

[50] W.H. Smith et al., Nucl. Inst. Meth. **A 355**, 278 (1995).

[51] N. Krumnack, *Testbeam experiments and Monte Carlo simulation of the ZEUS 6m Tagger*. Diploma Thesis, Universität Hamburg, Report DESY-THESIS-2001-033, 2001.

[52] R. Graciani, *Studies for a new electron tagger at 6m* (unpublished). ZEUS-99-038, internal ZEUS Note, 1999.

[53] R. Graciani, *A new electron tagger for ZEUS* (unpublished). ZEUS-99-067, internal ZEUS Note, 1999.

[54] G. Hochweller, P. Gasiorek, *ZEUS Luminosity Monitor Memory Module*, available on `http://fe.desy.de/sites/site_fe/content/e5/e8/e257/infoboxContent258/FEAmemory.pdf`.

[55] N. Latuske, *Untersuchung von szintillierenden Fasern für ein Spaghetti-Kalorimeter auf ihre Strahlungshärte*. Diploma Thesis, Universität Hamburg, 2001, available on `http://maren/diplomarbeiten/Nicolas_Latuske.ps.gz`.

[56] A. Ziegler, *Beeintrčhtigung der optischen Eigenschaften und Veränderung der Fluoreszenz von Kunststoffszintillatoren durch Röntgenstrahlung*. Ph.D. Thesis, Universität Hamburg, 2002, available on `http://maren/dissertationen/Thomas_Zoufal_0502.ps.gz`.

[57] A. Ziegler, *Investigation of the Scintillating Fiber SCSF-38M for the 6m-Tagger and Measurement of Inclusive K^0_S Meson and Λ Baryon Production in Neutral Current Deep Inelastic Scattering at HERA*. Ph.D. Thesis, Universität Hamburg, Report DESY-THESIS-2003-012, 2003.

[58] T. Gosau, *Online-Messungen von Strahlenschäden an szintillierenden Fasern*. Diploma Thesis, Universität Hamburg, 2003.

[59] U. Behrens et al., Nucl. Inst. Meth. **A 323**, 611 (1992).

[60] S. Wesch, *Untersuching der Strahlenschädigung am 6m Tagger*. Studienarbeit, Universität Hamburg, 2006.

[61] S. Lammers, D. Chapin, *Jet Energy Scale Uncertainty* (unpublished). ZEUS-01-006, internal ZEUS Note, 2001.

[62] N. Tuning, *ZUFOs: Hadronic Final State Reconstruction with Calorimeter, Tracking and Backsplash Correction* (unpublished). ZEUS-01-021, internal ZEUS Note, 2001.

[63] R. Sinkus and T. Voss, Nucl. Inst. Meth. **A 391**, 360 (1997).

[64] A. López-Durán Viani and S. Schlenstedt, *Electron Finder Efficiencies and Impurities. A Comparison Between SINISTRA95, EM and EMNET* (unpublished). ZEUS-99-077, internal ZEUS Note, 1999.

[65] J. Ng and W. Verkerke, *An Overview of SRTD Analysis* (unpublished). ZEUS-95-37.

[66] A. Kreisel, *Improving SRTD Position Reconstruction* (unpublished). ZEUS-03-007, internal ZEUS Note, 2003.

[67] J.E. Huth et al., *Research Directions for the Decade. Proceedings of Summer Study on High Energy Physics, 1990*, E.L. Berger (ed.), p. 134. World Scientific (1992). Also in preprint FERMILAB-CONF-90-249-E.

[68] O. González López, *Precise Determinations of the Strong Coupling Constant at HERA*. Ph.D. Thesis, Universidad Autónoma de Madrid, Report DESY-THESIS-2002-020, 2002.

Acknowledgments

I would like to thank my advisors Klaus Wick and Robert Klanner for their supervision. I would also like to thank everyone whom I worked with at Hamburg University and at ZEUS. Special thanks go to the members of the Wisconsin group at ZEUS.

Finally and most importantly I want to thank my parents, my grandma and my sister for their love and support.